Chem Soc Rev

Probing the Structures and Bonding of Size-Selected Boron and Doped-Boron Clusters

SCHOLARONE™
Manuscripts

Probing the Structures and Bonding of Size-Selected Boron and Doped-Boron Clusters

Tian Jian,[a,1] Xuenian Chen,[*b,c] Si-Dian Li,[*d] Alexander I. Boldyrev,[*e] Jun Li[*f] and Lai-Sheng Wang[*a]

[a] Department of Chemistry, Brown University, Providence, RI 02912, USA. E-mail: lai-sheng_wang@brown.edu
[b] School of Chemistry and Chemical Engineering, Henan Key Laboratory of Boron Chemistry and Advanced Energy Materials, Henan Normal University, Xinxiang, Henan 453007, China. E-mail:xnchen@htu.edu.cn
[c] College of Chemistry and Molecular Engineering, Zhengzhou University, Zhengzhou, Henan 450001, China
[d] Nanocluster Laboratory, Institute of Molecular Science, Shanxi University, Taiyuan 030006, China. E-mail: lisidian@sxu.edu.cn
[e] Department of Chemistry and Biochemistry, Utah State University, Logan, UT 84322, USA. E-mail: a.i.boldyrev@usu.edu
[f] Department of Chemistry and Key Laboratory of Organic Optoelectronics & Molecular Engineering of Ministry of Education, Tsinghua University, Beijing 100084, China. E-mail: junli@tsinghua.edu.cn

Abstract: Because of their interesting structures and bonding and potentials as motifs for new nanomaterials, size-selected boron clusters have received tremendous interests in recent years. In particular, boron cluster anions (B_n^-) have allowed systematic joint photoelectron spectroscopy and theoretical studies, revealing predominantly two-dimensional structures. The discovery of the planar B_{36} cluster with a central hexagonal vacancy provided the first experimental evidence of the viability of 2D borons, giving rise to the concept of borophene. The finding of the B_{40} cage cluster unveiled the existence of fullerene-like boron clusters (borospherenes). Metal-doping can significantly extend the structural and bonding repertoire of boron clusters. Main-group metals interact with boron through s/p orbitals, resulting in either half-sandwich-type structures or substitutional structures. Transition metals are more versatile in bonding with boron, forming a variety of structures including half-sandwich structures, metal-centered boron rings, and metal-centered boron drums. Transition metal atoms have also been found to be able to be doped into the plane of 2D boron clusters, suggesting the possibility of metalloborophenes. Early studies of di-metal-doped boron clusters focused on gold, revealing ladder-like boron structures with terminal gold atoms. Recent observations of highly symmetric $Ta_2B_6^-$ and $Ln_2B_n^-$ (n = 7−9) clusters have established a family of inverse sandwich structures with monocyclic boron rings stabilized by two metal atoms. The study of size-selected boron and doped-boron clusters is a burgeoning field of research. Further investigations will continue to reveal more interesting structures and novel chemical bonding, paving the foundation for new boron-based chemical compounds and nanomaterials.

---

[1] *Current address: Division of Chemical Science, Lawrence Berkeley National Laboratory, Berkeley, CA 94720, USA*

1. Introduction

Boron with three valence electrons $(2s^22p^1)$ is an electron-deficient element and possesses chemistry very different from that of its carbon neighbor.[1,2] To accommodate its electron deficiency, boron aggregates into versatile structures to share electrons, underlying the many allotropes of bulk boron.[3-5] While bulk boron is known to have different polyhedral structures as building units, early computational studies suggested that the very common icosahedral B_{12} cage was not stable as an isolated cluster and instead planar or quasi-planar structures were more favored for small boron clusters.[6-11] Early experimental studies mainly involved mass spectrometry observations and chemical reactivity of small cationic boron clusters.[12-20] However, no experimental structural or spectroscopic information was available. Since 2002, combined photoelectron spectroscopy (PES) and theoretical studies have been systematically undertaken to elucidate the structures and bonding of size-selected boron clusters and have shown that anionic boron clusters can be planar up to B_{38}^-.[21-49] A combined ion mobility mass spectrometry and theoretical study found that cationic boron clusters can be two-dimensional (2D) up to B_{15}^+.[50] Experimental studies of neutral boron clusters are challenging. Although small 3D cage structures were suggested,[51] the 2D-3D transition has not been observed experimentally.[52] All the planar structures feature two-center two-electron (2c-2e) σ bonds in the edge and delocalized multi-center two-electron (nc-2e) bonds between the inner and peripheral boron atoms via detailed bonding analyses.[53-55] The delocalized σ and π bonds give rise to the concept of multi-aromaticity and lead to the planarity in boron clusters.[24,25] Due to the similar π bonding, these planar boron clusters can be viewed as all boron-analogues of the polycyclic aromatic hydrocarbons (PAHs).[24,25,28-41,44-48] The discoveries of planar B_{36}/B_{36}^- and cage-like B_{40}/B_{40}^- represent two major breakthroughs in the study of boron clusters.[34,56] Cage-like B_{40} can be viewed as a boron analogue of C_{60}, aka borospherene. A family of borospherenes have been uncovered with B_{28}^- being the smallest one.[39,57] On the other hand, the planar B_{36} proves the viability of monolayer boron sheets with hexagonal vacancies, giving rise to the concept of borophene.[34] More flexible cluster motifs for borophene were also revealed, such as B_{35}^-, B_{37}^-, and B_{38}^-.[37,41] Recent studies show that the hexagonal vacancy is common for mid-sized boron clusters, while B_{26}^- is the smallest boron cluster with such a vacancy.[38,43] Borophenes have since been synthesized on silver substrates and becoming a new class of synthetic 2D materials.[58]

The fact that small boron clusters have a centered boron atom surrounded by a boron ring[25,26] has inspired considerations that other atoms may be used to replace the central boron atom.[59–63] Main group metal atoms interact with boron clusters through their s and p orbitals and avoid the central position. The lithium atom was found to have ionic interactions with boron clusters, mainly forming half-sandwich structures.[64–66] Aluminum also avoids the center position by either substituting the peripheral boron or forming half-sandwich structures.[67–70] Recently, it has been found that bismuth is capable of forming single, double, and triple bonds.[71–73] With a filled 5d electron shell and an unpaired 6s electron, gold prefers to form a covalent bond with a peripheral boron in gold-doped planar boron clusters.[74–78] Transition metal atoms with unfilled d orbitals turn out to be better guests for the center of 8, 9, 10-membered boron rings.[79–83] Both geometrical and electronic requirements must be fulfilled to form these doubly aromatic molecular boron wheels.[84–87] As the number of boron atoms increases, transition metal doped boron clusters evolve from metal-centered boron rings to metal-coordinated half-sandwich boron structures,[83,88] and eventually to metal-centered boron drums.[89–94] A family of transition-metal-centered boron drums with unprecedented coordination number were discovered, featuring a transition metal atom sandwiched by two boron rings.[91–94] Interestingly, planar CoB_{18}^- and RhB_{18}^- clusters were shown to have a metal atom doped into the boron triangular network, indicating the viability of metalloborophene.[93,95] Although lanthanides possess 5d and 6s electrons, the structures of mono-lanthanide doped boron clusters turned out to be similar to aluminum-doped clusters.[96–100]

Despite the recent advances on mono-metal doped boron clusters, the chemistry of di-metal doped boron clusters is relatively unexplored. Di-gold doped boron clusters were found to possess ladder-like structures with terminal gold atoms.[74,76,77] A series of di-tantalum doped boron clusters $Ta_2B_x^-$ ($x = 2-6$) were determined to have boron atoms building around a Ta−Ta dimer equatorially.[101,102] Very recently, a family of di-lanthanide-doped boron clusters are characterized to have η^n-B_n ($n = 7-9$) rings sandwiched by two lanthanide atoms.[103,104] The unique (d-p)δ bonds are vital to stabilize these inverse-sandwich complexes.

Previous experimental studies on non-metal doped boron clusters have involved hydrogen, carbon, oxygen, and silicon. Boron-rich oxide clusters have been found to feature a boron cluster core with terminal triply-bonded BO (boronyl) units,[105] which have been reviewed in a prior account.[106] Silicon-boron mixed clusters that have been experimentally characterized

are mostly made of a few boron atoms doped into silicon clusters.[107–111] Carbon was first predicted to be hypercoordinated in carbon-doped boron clusters,[112–114] but was shown to avoid the central position and favor 2c-2e bonds on the periphery.[115–120] Dihydrogenated boron clusters were found to be ladder-like structures with terminal hydrogens in cis- or trans- positions, which are analogous to polyenes.[121]

A number of reviews and perspectives have appeared previously about size-selected boron clusters. Early studies on small boron clusters and their potentials as inorganic ligands were extensively reviewed in 2006.[45] The chemical bonding, structural characteristics and fluxionality of boron clusters were discussed in a Perspective article in 2014.[46] The experimental efforts on size-selected boron clusters have been comprehensively reviewed recently, highlighting the advances that led to the discoveries of borophenes and borospherenes.[47,48] Very recently, a perspective has appeared, focusing on the findings of planar CoB_{18}^- and RhB_{18}^- clusters and their implications for metalloborophenes.[49] Significant progress has been made over the past several years both in understanding the structural evolution of size-selected boron clusters and metal-doped boron clusters. Now all boron clusters (B_n^-) for $n = 3-40$ have been completely elucidated. The current review will cover these recent progresses, focusing on the few boron clusters that have been difficult to solve, such as B_n^- ($n = 26, 28, 29, 31, 32, 33, 34, 37, 38$) and in particular the recent advances in doped-boron clusters including Bi-B binary clusters with multiple bismuth-boron bonds, metal-centered boron drums, planar doped-boron clusters as motifs for metallo-borophenes, and di-metal-coordinated inverse boron sandwiches. A better understanding of boron-boron and metal-boron bonding will eventually enable us to synthesize new boron compounds and design novel boron-based materials with tailored properties.

2. Experimental and theoretical methods

Most of the experimental studies covered in this review were performed in a magnetic-bottle time-of-flight PES apparatus, details of which were described before.[47,122] An ultraviolet laser was used to detach valence electrons from size-selected anionic clusters. Electron binding energies were obtained by subtracting the measured electron kinetic energies from the detachment laser photon energy. PES directly probes the energy levels of the valence electrons, which are responsible for chemical bonds in the size-selected clusters. The electron binding

energy is essentially the energy difference between the ground state of a size-selected anion cluster and the ground or an excited state of the corresponding neutral. The peak maximum of one detachment band represents the vertical detachment energy (VDE), which corresponds to a vertical transition from the ground state of an anion to the final state of the corresponding neutral. The onset of the first detachment band represents the adiabatic detachment energy (ADE), which also stands for the electron affinity (EA) of the corresponding neutral species. The ADE and VDEs, as well as vibrational features sometimes, measured from a photoelectron spectrum provide a fingerprint of the underlying size-selected cluster and they are compared with theoretical calculations to determine the structure of the cluster.

Determination of global minimum structures is key to elucidate the energetics, geometric and electronic structures, and chemical bonding of size-selected boron clusters. Global minimum searches for large boron clusters or metal-doped boron clusters can be extremely challenging and computationally expensive. With the development of search algorithms, such as Basin Hopping (BH),[123] Gradient Embedded Genetic Algorithm (GEGA),[124] Coalescence Kick (CK),[30] Cartesian Walking (CW),[31] and the recently developed Tsinghua Global Minimum (TGMin) method,[125,126] it is possible to perform global minimum searches for clusters consisting of tens of atoms. By comparing the theoretical VDEs and ADEs of low-lying isomers with experimental data, the global minimum or low-lying isomers observed in the experiments can be determined. The calculated vibrational frequencies can also be used to compare with the experimental data (when available) to confirm the obtained structures. To understand the stability and chemical bonding of the observed clusters, chemical bonding analyses can be done using canonical molecular orbitals (CMOs) or the adaptive natural density partitioning (AdNDP) method.[55]

3. Size-selected boron clusters

The investigations of carbon clusters have led to the discoveries of fullerenes,[127] carbon nanotubes,[128] and graphenes.[129] One of the major motivations to study size-selected boron clusters is to assess the possibility if boron can form similar nanostructures.[21-49] Because of its electron deficiency, a fullerene-like B_{60} with sp^2 hybridization is not stable. Filling each hexagon on the fullerene-like B_{60} by a boron atom led to a fullerene-like B_{80}, which was suggested to be the first all-boron fullerene.[130] However, subsequent calculations showed many core-shell-type structures were much more stable.[131–135] Boron nanotubes that consist of triangular monolayer

boron sheets were also suggested,[136] but were found to be less stable than those made of triangular monolayer boron sheets with hexagonal vacancies.[137,138] Due to its electron deficiency, boron cannot form hexagonal monolayers like graphene with pure sp^2 hybridization. While filling all the hexagons in a graphene-like boron sheet makes the resulting triangular sheet too electron-rich, boron sheets with hexagonal vacancies were predicted to be more stable.[137–140] Apparently, a systematic elucidation on the structural and electronic properties of size-selected boron clusters is necessary for the rational design and development of boron-based nanomaterials.

This endeavor was initiated in 2001 by combining PES and computational chemistry.[21-48] Fig. 1 summarizes the global minima of all the B_n^- ($n = 3−40$) clusters that have been elucidated heretofore. Most clusters display distinct and highly stable global minima, but low-lying isomers have been observed for some clusters; only the borospherene isomers of B_{39}^- and B_{40}^- are given here.[56,57] As revealed by AdNDP analyses, planar or quasi-planar boron clusters feature 2c-2e σ bonds in the peripheral ring and delocalized σ and π bonds between the inner and outside boron atoms.[53,55] Consequently, the peripheral B−B bonds are stronger and shorter than the inner ones. As a result, most of the interior boron atoms in the 2D boron clusters either have slight out-of-plane displacement or form polygonal vacancies in the cluster plane. Small boron clusters from B_3^- to B_{18}^- all consist of boron triangular lattices with up to one tetragonal vacancy.[21-28,30] Going from B_{19}^- to B_{25}^-, we start to observe multiple tetragonal or pentagonal vacancies.[29,31-33,36] The B_{26}^- cluster is the smallest boron cluster to contain a hexagonal vacancy,[43] which becomes characteristic for larger boron clusters from B_{30}^- to B_{38}^-.[34,35,37,41,44,141] The discovery of hexagonal B_{36}^- is a major advance in boron chemistry,[34] providing the first experimental evidence for the viability of monolayer boron sheets with hexagonal vacancies. This finding led to the name "borophene" because of its experimental viability.[34] Borophenes were synthesized shortly after[58] and they are becoming a new class of synthetic 2D materials.[142] While the cage-like isomer of B_{40}^- is observed to be the first all-boron fullerene (borospherene),[56] the B_{39}^- cluster is characterized to have two chiral borospherene structures (Fig. 1).[57] A family of borospherenes were observed, including the low-lying 3D isomers for B_{28}^- and B_{29}^-.[39,40]

The experimental studies on boron clusters focus on boron anions and cations, mainly due to the challenge of mass separation for neutral clusters. In 2012, the structures of neutral B_{11}, B_{16}, and B_{17} clusters were probed by infrared/ultraviolet two photon ionization and density

functional theory calculations, which found that the neutrals have similar structures as their anion counterparts.[52] In 2007, ion mobility and theoretical calculations were used to elucidate the structures of boron cations from B_{12}^+ to B_{25}^+.[50] Collision cross sections measured from ion-mobility were compared with the calculated values to determine the cationic structures. It was concluded that there is a structural transition from planar to double-ring structures at B_{16}^+, in which a double-ring structure is found to compete with a planar structure.

In this section, the recent advances on mid-sized boron clusters are reviewed, including B_n^- ($n = 26, 28, 29, 31, 32, 33, 34, 37, 38$).

3.1. B_{26}^-: Smallest boron cluster with a hexagonal vacancy

Among the mid-sized boron clusters, B_{26}^- was challenging because its complicated PE spectrum despite a prior computational investigation.[143] The PE spectrum of B_{26}^- at 193 nm is shown in Fig. 2a, displaying four main spectral bands (X, A-C) and a weak band (X').[43] Global minimum searches were done using the Minima Hopping (MH)[144] and BH methods at the PBE0 level of theory. The top five isomers of B_{26}^- within 0.5 eV at PBE0 are shown in Fig. 3a. While the close-packed triangular isomer II has the lowest energy at the PBE0 and CCSD(T) levels, its simulated spectrum did not agree well with the experimental spectrum (Fig. 2c). To take into account the entropic effects at finite temperatures, the Gibbs free energy corrections beyond the single point CCSD(T) energetics were calculated for the top five isomers, as shown in Fig. 4. It was found that isomers I and III became more stable as temperature increased with isomer I being more stable than isomer II above 440 K. The overall spectral pattern of the simulated spectrum of isomer I agrees well with the experimental spectrum (Fig. 2b), lending considerable credence to isomer I as the main contributor of the observed spectrum. Both isomers II and III had lower VDEs and could be responsible for the weak low binding energy feature X' (Fig. 2). Thus, it was concluded that all three isomers I-III were present in the cluster beam with isomer I being the major species under the experimental conditions.

While a low-lying isomer with a hexagonal vacancy was observed for B_{27}^-,[38] the B_{26}^- cluster was the smallest boron cluster with a hexagonal vacancy being the global minimum and major contributor for the observed spectrum. CMO analyses of the closed-shell B_{26}^{2-} species corresponding to isomer I showed that it possesses eight delocalized π MOs, analogous to those

of the PAH $C_{17}H_{11}^+$, as shown in Fig. 5. The AdNDP analyses given in Fig. 6a revealed eight multi-center π bonds, which are very similar to those of $C_{17}H_{11}^+$ (Fig. 6b).

In summary, isomer I of B_{26}^- represents the smallest boron cluster with a hexagonal vacancy and can be viewed as an all-boron analog of the PAH $C_{17}H_{11}^+$.

3.2. B_{28}^- and B_{29}^-: Competition between quasi-planar and cage-like structures

3.2.1. B_{28}^-: The smallest borospherene. Previous computational studies suggested that both 2D close-packed triangular lattice and 3D cage-like structures were might be the global minimum for B_{28}.[143,145] The mid-sized boron clusters appeared to possess fairly complicated potential energy surfaces and required the most careful global searches in combination with the experiment to yield the global minimum with confidence. The PE spectrum of B_{28}^- at 193 nm is shown in Fig. 7a with a relatively congested and broad pattern, indicating multiple isomers could contribute to the observed spectrum.[39] A very weak feature X' was observed at the lower binding energy side, and its intensity could increase from 10% to 20% relative to that of feature X under hotter source conditions, confirming that feature X' was from a low-lying isomer of B_{28}^-.

The top five isomers of B_{28}^- at the PBE0 and CCSD(T) levels of theory are shown in Fig. 8a. The global minimum is a closed-packed triangular 2D structure with 16 peripheral atoms and 12 interior atoms. The second low-lying isomer is a 3D seashell-like structure, only 0.05 eV higher than the global minimum at the CCSD(T) level. The structural details of isomers I and II are given in Fig. 9. The seashell-like isomer II consists of two quasi-planar B_{15} triangular sheets fused together by sharing two corner atoms at the bottom and via a B_2 twist at the top corner. There are two heptagons on the waist and a hexagon at the bottom. The third isomer III with a hexagonal vacancy is only 0.08 eV higher in energy than the global minimum at the CCSD(T) level. While isomers III to V could be safely excluded due to their energies, isomers I and II are very close in energy and could co-exist in the experiment. The simulated spectra were compared with the experimental spectrum in Fig. 7. The simulated spectrum of isomer I agrees well with the major features, while that of isomer II is in good agreement with the peak X' and the features in the 4.7-5.1 eV range. The overall good agreement of the experimental spectrum with the combined simulated spectra of isomers I and II provided considerable credence for the 2D global minimum of B_{28}^- and the cage isomer II.

As shown in Fig. 10, the chemical bonding analyses of the planar closed-shell B_{28}^{2-} corresponding to isomer I showed it possesses similar π bonding to the PAH dicyclopenta[cd,jk]pyrene ($C_{20}H_{10}$). Thus, the global minimum of B_{28}^- can be viewed as the analogue of PAH $C_{20}H_{10}$. For the seashell isomer II, chemical bonding analyses were performed on the close-shell B_{28} cage using both electron localization function (ELF) (Fig. 11a)[146] and the AdNDP method. While there are thirty-eight B_3 triangles on the B_{28} cage, there are thirty-two 3c-3e σ bonds and one 12c-2e σ bond, as shown in Fig. 11b. In addition, there are three 3c-3e π bonds in each B_{15} sheet, one 6c-2e and two 5c-2e π bonds among the corner sites (Fig. 11c). Overall, the 18 π electrons in the B_{28} seashell constitutes $2(n+1)^2$ spherical aromaticity.[147]

In summary, the close-packed quasi-planar structure and the seashell-like cage structure are competing for the global minimum for B_{28}^-. Even though it was a minor component in the cluster beam, the seashell structure represented the smallest borospherene observed experimentally.

3.2.2. B_{29}^-: Competition between quasi-planar and cage-like structures continued. The PE spectrum of B_{29}^- at 193 nm and the comparison with the simulated spectra of the top three low-lying isomers are shown in Fig. 12.[40] The experimental spectrum was complicated with multiple weak features in the lower binding energy side of the peak X. Two bands X' and X'' were tentatively labeled. The global minimum searches revealed a structural landscape with mostly 2D and a couple of 3D low-lying structures. The top five low-lying isomers are shown in Fig. 13. Isomer 1 is a quasi-planar structure with a pentagonal vacancy, which has a stingray-like shape. Similar to the B_{28}^- borospherene, the seashell-like isomer 2 contains two quasi-planar B_{15} triangular lattices sharing one apex atom at the top and forming two B_2 interlaces at the bottom. There are two heptagons on the waist and one octagon at the bottom. Isomer 3 is also quasi-planar with a hexagonal vacancy.

The Gibbs free energy corrections beyond the single point CCSD(T) energetics were calculated for the top five isomers to account for entropic effects at finite temperatures, as shown in Fig. 14. Isomers 1 and 3 became more stable as temperature increased with isomer 1 being more stable than isomer 2 above ~300 K. The simulated spectrum of isomer 1 was in good agreement with the experimental spectrum (Fig. 12b), lending considerable credence to isomer 1 as the main species in the cluster beam. Isomers 2 and 3 can account for the weak features X' and X'', suggesting they were weakly populated in the cluster beam.

Chemical bonding analyses of isomer 1 were performed using CMO (Fig. 15) and AdNDP (Fig. 16), showing that the π bonding was analogous to that of the PAH benzo[ghi]fluoranthene ($C_{18}H_{10}$). The AdNDP analyses of the 3D isomer 2 are shown in Fig. 17. While there are thirty-eight B_3 triangles with sixteen on each B_{15} sheet and six at the joints, the AdNDP analyses give rise to thirty-four 3c-2e σ bonds and one 6c-2e σ bond at the top joint. Additionally, there are three 5c-3e π bonds in each B_{15} sheet, one 5c-2e and two 6c-2e π bonds among the corner sites, satisfying the $2(n+1)^2$ spherical aromaticity. In summary, the competition between the quasi-planar and cage-like structures continued at B_{29}^-.[40]

3.3. B_{31}^- and B_{32}^-: Chiral quasi-planar boron clusters

The B_{31}^- and B_{32}^- clusters have been the most elusive among the B_n^- ($n<40$) clusters and they have not been solved until very recently.[141] The PE spectra of B_{31}^- and B_{32}^- at 193 nm are shown in Figs. 18a and 19a, respectively, compared with the simulated spectra of the global minima or the top low-lying isomers. The top five low-lying isomers of B_{31}^- and B_{32}^- are shown in Fig. 20. The global minima of B_{31}^- are found to be a pair of chiral hexagonal quasi-planar structures (I and II). The third low-lying isomer III is a seashell-like structure, which is 0.08 eV higher at the CCSD(T) level. The global minimum structures of B_{32}^- are also found to be a pair of chiral hexagonal quasi-planar structures (VI and VII). The third low-lying isomer VIII also contains a hexagonal vacancy, lying 0.13 eV higher at the CCSD(T) level.

For B_{31}^-, the chiral isomers I and II give rise to identical VDEs and simulated spectra. Both isomers I and II can reproduce all the features in the experimental spectrum (Fig. 18b). While the calculated VDEs of other low-lying isomers are inconsistent with the observed features, the degenerate chiral enantiomers I and II can reproduce all the observed features and are assigned as the global minimum for B_{31}^-. Similarly, the calculated VDEs of the isomers VI and VII of B_{32}^- are in good agreement with the experimental spectrum (Fig. 19b), while isomer VIII is the only low-lying isomer that could account for peak X'. It was concluded that the degenerate chiral enantiomers VI/VII are the main contributor in the cluster beam of B_{32}^-, the closest low-lying isomer VIII is present as a minor species.

Chemical bonding analyses for the global minima of B_{31}^- and B_{32}^- using AdNDP are shown in Figs. 21 and 22, respectively. It was observed that the π bonding in B_{31}^- exhibited a similar pattern with that of the PAH $C_{19}H_{11}^-$ (Fig. 21), whereas the π bonding pattern in B_{32}^- was

found to be analogous to that in the PAH perylene ($C_{20}H_{12}$) (Fig. 22). Hence, the global minimum structures of B_{31}^- and B_{32}^- are both chiral and can be viewed as all-boron analogues of PAHs.

3.4. B_{33}^- and B_{34}^-: Aromatic planar boron clusters with a hexagonal vacancy

The PE spectra of B_{33}^- and B_{34}^- are shown in Figs 23a and 24a, compared with the simulated spectra from the respective global minimum structure.[44] The spectrum of B_{33}^- was fairly congested, while that of B_{34}^- was separated into two spectral regions. The top four low-lying isomers of the two clusters are given in Fig. 25. The global minimum of B_{33}^- has a hexagonal vacancy with eighteen peripheral and fifteen interior atoms (Fig. 25a). The global minimum structures of B_{34}^- were a pair of chiral hexagonal quasi-planar structures (V and VI in Fig. 25b), similar to those of B_{31}^- and B_{32}^- discussed above. As shown in Fig. 23b, the simulated spectrum of isomer I agreed well with the observed spectrum, strongly confirming the identified global minimum for B_{33}^-. For the B_{34}^- cluster, the chiral isomers V and VI gave rise to identical spectra that were in good agreement with observed spectrum, lending considerable credence for the identified chiral global minimum.

Chemical bonding analyses were performed using AdNDP for the global minima of B_{33}^- and B_{34}^-, as shown in Figs 26 and 27, respectively. The global minimum of B_{33}^- was found to have 10 delocalized π bonds, which were similar to those in the PAH $C_{19}H_{11}^-$ (Fig. 26b). AdNDP analyses on the closed-shell B_{34}^{2-} corresponding to the chiral global minimum of B_{34}^- revealed two delocalized π systems (Fig. 27): nine 5c-2e π bonds around the periphery and three 5c-2e π bonds around the inner hexagon. The π bonding pattern in B_{34}^{2-} suggested double π aromaticity.

Overall, the global minima of B_{33}^- and B_{34}^- were observed to be quasi-planar with a hexagonal vacancy. These results suggested that B_{35}^- was the smallest boron cluster to possess a double-hexagonal vacancy (DHV).[37]

3.5. B_{37}^- and B_{38}^-: Borophene motifs with a double-hexagonal vacancy

The B_{37}^- and B_{38}^- cluster are in between the structural transition from borophene-type 2D structures (B_{35}^- and B_{36}^-) to the 3D borospherenes (B_{39}^- and 3D B_{40}^-).[41] Prior calculations on B_{38} suggested that a borospherene cage and a 2D isomer with a DHV competed for the global minimum,[51b,148] but that was not confirmed experimentally. The PE spectra of B_{37}^- and B_{38}^- at 193 nm are shown in Fig. 28, in comparison with the simulated spectra of the global minima.

The spectrum of B_{38}^- exhibited six well-spaced bands as well as continuous signal beyond 6.0 eV (Fig. 28a), while the spectrum of B_{37}^- displayed nine well-resolved bands (Fig. 28c). The global minima and low-lying isomers of B_{38}^- and B_{37}^- are shown in Figs. 29 and 30. The 2D global minimum of B_{38}^- with a DHV (**1** in Fig. 29) was found to be at least 0.74 eV more stable than the nearest low-lying isomer (Fig. 30a), suggesting the overwhelming stability of the 2D structure. Interestingly, the cage-like B_{38}^- lied 1.33 eV higher than the global minimum 2D structure **1**. The global minimum of B_{37}^- (**2** in Fig. 29) can be viewed as removing a boron atom from the shorter edge of B_{38}^- (**1**) with significant local distortions. There is also no nearby low-lying isomer for B_{37}^- (Fig. 30b).

Hence, no contributions from low-lying isomers were expected to the observed PE spectra for B_{38}^- and B_{37}^-. The simulated spectra for the global minima of B_{38}^- and B_{37}^- were indeed in excellent agreement with the experimental spectra, as shown in Fig. 28, establishing the global minima of these two clusters both contained a DHV (Fig. 29). Chemical bonding analyses for the closed-shell B_{38}^{2-} and B_{37}^- are shown in Fig. 31. The π bonding patterns of both B_{38}^{2-} and B_{37}^- were found to be very similar, and both were analogous to that in the PAH coronene ($C_{24}H_{12}$), continuing the hydrocarbon analogues of all boron clusters.[24,25]

4. Main group doped boron clusters

4.1.   Lithium and aluminum doped boron clusters. The electronic and structural properties of pure boron clusters have been systematically characterized up to B_{40}^- (Fig. 1), dominated by delocalized σ and π bonds formed from the 2s and 2p orbitals. Doping boron clusters by a single main group atom can lead to a variety of structures, as shown in Fig. 32. These structures were obtained from joint PES and theoretical investigations. Lithium prefers to donate its valence electron to the boron motif, forming half-sandwich structures via mainly ionic bonding.[64,65] LiB_6^- and LiB_8^- are two interesting charge-transfer complexes, where Li donates its electron to the C_{2v} B_6^{2-} and C_{7v} B_8^{2-}. Chemical bonding analyses showed B_6^{2-} is doubly antiaromatic,[65] while B_8^{2-} is doubly aromatic.[64] Aluminum can also form similar charge-transfer complexes in AlB_7^- and AlB_8^-, where the Al atom donates two and one electrons to form the doubly aromatic C_{6v} B_7^{3-} and C_{7v} B_8^{2-}, respectively.[68] Moreover, Al can form covalent interactions with peripheral boron atoms or the whole boron cluster.[67,69] Neither lithium or aluminum could be stabilized in the center of a boron ring.

4.2   Mono-bismuth doped boron clusters. Boron clusters and compounds are dominated by delocalized bonds. Although boron has only three valence electrons, it is capable of forming B≡B triple bonds not only in the gas phase but also in condensed phase.[105c,149,150] In fact, boron can readily form a triple bond with O in gaseous BO⁻ species, which act as a unit (boronyl) in all boron-rich oxide clusters.[105] In fact, a boronyl compound has been even isolated.[151] While the metal boron triple bond has been experimentally elusive,[152] boron has been found to be able to form double and triple bonds with a bismuth atom in linear bismuth boron species.[73]

The PE spectra of BiB_2O^- are shown at three photon energies in Fig. 33. There were only three sharp features in the 193 nm spectrum, while the first two bands were vibrationally resolved in the 355 nm and 266 nm spectra. The short vibrational progressions and sharp bands suggested there was minimal geometry change upon electron detachment from BiB_2O^-. The PE spectra of Bi_2B^- are shown at three photon energies in Fig. 34. The overall spectral pattern was slightly more complicated with four intense bands and several weak features. The global minimum structures for BiB_2O^- and Bi_2B^- were both found to be linear, as shown in Fig. 35. The VDEs were calculated and were found to be in excellent agreement with the experimental data.[73]

Chemical bonding analyses using AdNDP (Fig. 36) revealed that the linear structures of BiB_2O^- and Bi_2B^- can be viewed indeed as [Bi≡B-B≡O]⁻ and [Bi=B=B]⁻. For BiB_2O^-, there is a Bi≡B triple bond, a B−B single bond, and a B≡O triple bond, constituting an electron-precise species with high stability. For Bi_2B^-, there are two Bi=B double bonds. Together with the previously observed [Bi−B≡O]⁻ species,[71] there is now available a complete series of bonds between bismuth and boron. This is the first experimental observation of Bi−B double and triple bonds, opening the door to design metal−boron complexes with multiple bonding.

4.3.   Di-bismuth doped boron clusters $Bi_2B_n^-$ (n = 2–4).[153] Bismuth boride is a heavy member of the III-V semiconductors.[154] Though there have been some theoretical interests in this material,[155-158] it has not been synthesized experimentally. Very recently, a series of boron-bismuth binary clusters, $Bi_2B_n^-$ (n = 2–4), were produced by laser vaporization of a B/Bi mixed target and investigated by high-resolution PE imaging in combination with theoretical calculations. Vibrationally-resolved PE spectra were obtained for all three clusters and the measured vibrational and electronic information was used to compare with theoretical calculations to understand their structures and bonding. As shown in Fig. 37, the $Bi_2B_2^-$ cluster

was found to be linear ($D_{\infty h}$, $^2\Pi_g$) with a B_2 unit and two terminal Bi atoms, while $Bi_2B_3^-$ was found to be planar (C_{2v}, $^1A_1$), consisting of a B_3 triangle with two bridging Bi atoms. Interestingly, the spectra of $Bi_2B_4^-$ revealed two co-existing isomers; both were found to be planar and contained a rhombus B_4 unit with two bridging Bi atoms in a *trans* (C_{2h}, ^2A_u) and *cis* (C_{2v}, $^2B_1$) fashion separated only by 0.03 eV in energy (Fig. 37c). In the neutrals, the rhombus structure for Bi_2B_2 became the global minimum (Fig. 37a), where the structure of Bi_2B_3 was similar to that of the anion. For neutral Bi_2B_4, the *trans* isomer became much more stable than the *cis* isomer by 0.33 eV in energy, as shown in Fig. 37c.

The interactions between the two Bi atoms and the B_n motifs were understood using AdNDP chemical bonding analyses, as shown in Fig. 38. The 6s electrons clearly remain as a lone pair on each Bi atom and only the 6p orbitals participate in chemical bonding with the boron atoms, due to the relativistic stabilization of the 6s orbital.[159] The bonding in the linear Bi_2B_2 cluster can be viewed approximately as Bi=B=B=Bi. In the larger clusters, the Bi atoms each form two single Bi−B σ bonds with the B_3 or B_4 motifs. In the $Bi_2B_3^-$ cluster, the delocalized σ and π bonds were found to be similar to those in the bare B_3 cluster. The bonding in the two $Bi_2B_4^-$ isomers were similar, both containing a delocalized σ and π bond in the B_4 unit. This study showed that the   Bi–B bonding is weak enough so that the B_n units maintain their structural integrity with the Bi atoms bonded to the cluster periphery only.

4.4. Non-metal doped boron clusters. While there may have been many computational studies of mixed boron clusters with non-metal elements, here we will limit our review only on joint experimental and theoretical studies on carbon and hydrogen doped boron clusters. Fig. 39 summarizes all the global minima of carbon-doped boron clusters confirmed from joint PES and theoretical studies. Carbon was initially proposed to be hypercoordinated in CB_6^{2-}, CB_7^-, and CB_8 clusters, i.e., C©B_n.[112–114] However, carbon was found to avoid the central position and prefer peripheral position in these clusters.[115–118] Being more electronegative than boron, carbon favors 2c-2e σ bonds in the peripheral position. Subsequent studies on $C_xB_{5-x}^-$ ($x = 1-5$), CB_9^-, and $C_2B_8^-$ clusters revealed carbon always avoided the central position (Fig. 39).[119,120]

The structures and chemical bonding of planar boron clusters were in stark contrast to those of the 3D borane compounds. Hydrogenation of pure boron clusters was expected to break the peripheral B−B σ bonds, and cause the structural transition from planar to 3D structures. Theoretical calculations showed the $H_2B_7^-$ cluster to have an elongated two-row (ladder-like)

structure with two terminal hydrogen atoms in *cis* positions.[160] A joint PES and theoretical study showed that $Au_2B_7^-$ had a similar structure, revealing the H/Au analogy in bonding with boron.[74] Fig. 40 summarizes all the global minima of $B_nH_2^-$ (n = 7−12) clusters confirmed from joint PES and theoretical calculations.[121a] All these dihydrogenated boron clusters were found to have ladder-like structures with two terminal hydrogens in *cis* or *trans* positions. The AdNDP analyses of these dihydrogenated boron clusters are shown in Fig. 41, featuring 2c-2e σ bonds between peripheral boron atoms, 2c-2e σ bonds between the terminal boron and hydrogen, and delocalized σ and π bonds between the two boron rows. Remarkably, the π orbitals of these dihydrogenated boron clusters were found to be similar to those of conjugated alkenes, as shown in Fig. 42. The similarity in π bonding suggested that these dihydrogenated boron clusters could be considered as polyene analogues or polyboroenes.[121]

5. Transition metal doped boron clusters

Due to the strong bonding capacity of the *d* orbitals, transition metal doped boron clusters are versatile in structures and chemical bonding.[49,83,88] Fig. 43 summarizes the representative transition metal doped boron clusters with a variety of dopants, such as the coinage metal gold, 3d metal cobalt, 4d metal rhodium, and 5d metal tantalum. With a $5d^{10}6s^1$ electron configuration, gold can act as a σ electron donor and forms strong covalent bonds with boron.[161] Hence, gold behaves like hydrogen in gold-doped boron clusters, avoiding the central positions and interacting with the boron clusters via a peripheral boron atom.[74–78] The first row of Fig. 43 displays four mono-gold doped boron clusters, each containing a σ bond between the Au atom and a peripheral boron atom.

Transition metal atoms with open *d* shells are more flexible in bonding with boron clusters, forming a variety of structures. The B_9^- cluster was known to have D_{8h} symmetry with double aromaticity, where the central boron was bonded with the B_8 ring via completely delocalized bonds.[25] Inspired by this perfect molecular wheel, a design principle was proposed to substitute the central boron atom with various transition metal atoms to form metal-centered boron rings ($M©B_n$).[79,85] With the right electron counts to satisfy double aromaticity (σ and π) and appropriate dopant size, a family of 8, 9, 10-membered transition metal-centered boron rings have been produced and investigated. The chemical bonding using AdNDP for three representative borometallic molecular wheels, D_{8h} $Co©B_8^-$, D_{9h} $Ru©B_9^-$, and D_{10h} $Ta©B_{10}^-$ is

shown in Fig. 44, all possessing double aromaticity. The second role in Fig. 40 shows the structures of TaB_n^- (n = 3–8),[87] revealing how the D_{10h} $Ta©B_{10}^-$ molecular wheel is formed. Interestingly, boron atoms were found not to simply nucleate around the Ta atom on the way to $Ta©B_{10}^-$, but undergo a structural transition at TaB_6^-, which can be viewed as substituting a peripheral B atom in the C_{6v} B_7^- cluster by a Ta atom.

The $M©B_n^-$ borometallic molecular wheels have been discussed in detail in a previous perspective article.[83] Here we review in detail only the larger mono-transition metal doped boron clusters beyond 10 boron atoms. In the larger sizes, half-sandwich structures, metal-centered boron drums, and 2D cluster motifs for metallo-borophenes start to appear,[83,88,91–95] as presented in Fig. 43.

5.1. Metal-coordinated half boron sandwiches.

The B_{12} cluster is aromatic with six electrons and has a bowl-shape,[24] making it ideal to form half-sandwich structures. The PE spectra of CoB_{12}^- and RhB_{12}^- at two different photon energies are shown in Fig. 45.[88] The 193 nm spectrum of CoB_{12}^- displayed five bands, while no fine features could be resolved in the 266 nm spectrum. The overall spectral pattern of RhB_{12}^- was very similar to that of CoB_{12}^- except the first band was resolved into two bands in the 266 nm spectrum (Fig. 45d). The global minima for CoB_{12}^- and RhB_{12}^- were also found to be similar, as shown in Fig. 46. As expected, they both formed half sandwich structures with C_{3v} symmetry. To better accommodate the metal atoms, the B_{12} moiety were slightly more buckled compared with the bare B_{12} cluster. The calculated VDEs for the C_{3v} global minima were in good agreement with the experimental data, confirming the half sandwich structures for CoB_{12}^- and RhB_{12}^-.[88]

The chemical bonding in the half sandwich complexes was analyzed using AdNDP, as shown in Fig. 47 for RhB_{12}^-. The localized peripheral σ bonds in the B_{12} motif are similar to those in the bare B_{12} cluster. The interactions between Rh and B_{12} are described in three types of bonds. First, Rh interacts with the three peripheral boron atoms of B_{12} via three 2c-2e σ bonds. Second, Rh forms a 4c-2e π bonds with the bottom B_3 triangle through its $4d_{z^2}$ orbital. Most importantly, Rh is involved in four totally delocalized bonds via both σ and π interactions. Overall, the metal-boron interactions are strongly covalent, quite different from the primarily

ionic interactions in the LiB_6^-, LiB_8^-, AlB_7^-, or AlB_8^- half-sandwich complexes. Recently, numerous computational studies of B_{12} sandwich-type complexes have been reported.[162-168]

5.2. Metal-centered boron drums

As potential embryos for boron nanotubes, tubular boron clusters have been of interest for many years.[27] While pure or doped tubular boron clusters were computed to be stable, they have never been experimentally confirmed until these recent experimental advances except the B_n^+ cations from the ion mobility experiment.[50]

5.2.1. CoB_{16}^-: Cobalt-centered boron drum. The PE spectra of CoB_{16}^- at two different photon energies are shown in Fig. 48.[91] The overall spectral pattern was relatively simple, suggesting the structure of the CoB_{16}^- cluster was likely to be symmetric and rigid. Global minimum searches revealed a D_{8d} isomer I and a C_{4v} isomer II were competing for the global minimum (Fig. 49), which could be considered to be degenerate. The C_{4v} isomer could be viewed as slightly distorted from the D_{8d} isomer. Their structural details are also shown in Fig. 48, both featuring a cobalt atom centered in a B_{16} tube. The VDEs for the first two detachment channels for isomers I and II were calculated and they compared well with the observed values. Recently, the full detachment channels for the two isomers are calculated and the simulated spectra are found to be in good agreement with the observed PE spectra,[169] providing further confirmation for the two drum-like structures to be the global minima of CoB_{16}^-.

The C_{4v} structure was similar to the D_{8d} isomer and was due to a slight Jahn-Teller distortion. The AdNDP bonding analyses of the D_{8d} isomer are shown in Fig. 50, where the first row revealed sixteen 2c-2e B-B bond in the B_8 rings and the $3d_{z^2}$ lone pair on Co. The remaining delocalized bonds were responsible for the interactions between the two B_8 rings, as well as the interactions between Co and the two B_8 rings. The second row includes five delocalized $\sigma+\sigma$ bonds, which are formed by the overlap of the delocalized σ bonds between the B_8 rings. The two 17-2c $\sigma+\sigma$ bonds primarily result from the $3d_{xy}$ and $3d_{x^2-y^2}$ orbitals of Co interacting with the boron rings. The third row displays three delocalized $\sigma-\sigma$ bonds, which represent bonding interactions within each ring, but anti-bonding interactions between the two boron rings. The two 17-2c $\sigma-\sigma$ bonds involve bonding interactions between the $3d_{xz}$ and $3d_{yz}$ orbitals of Co with the boron rings. The last row represents the $\pi-\pi$ interactions between the two boron rings. Overall, the AdNDP analysis indicated strong bonding interactions between the 3d orbitals of Co and the

B_8 rings. While the pure B_{16} cluster is planar,[28] the strong bonding between Co and the boron tube helps stabilize the CoB_{16}^- drum.

5.2.2. MnB_{16}^-: A second member of the metal-centered boron drums. The discovery of the CoB_{16}^- drum was significant in two respects. First, it represented the highest coordination number for a metal atom at the time. Second, it was the first tubular boron cluster characterized spectroscopically. Even though the tubular B_{20}^- was predicted to be the global minimum,[27,170] the experimentally observed specie was in fact the planar structure (Fig. 1). Hence, the question was if the CoB_{16}^- tubular structure was unique to Co or if other transition metals can from similar structures. The second system that was investigated was MnB_{16}^-.[92] The PE spectrum of MnB_{16}^- at 193 nm is shown in Fig. 51a. Global minimum searches were performed using the TGMin code and the CK program. As shown in Fig. 52, the C_{4v} drum isomer was found to be the global minimum for MnB_{16}^-, whereas neutral MnB_{16} had a lower symmetry C_{2v} drum structure. The simulated spectrum of the C_{4v} isomer was in good agreement with the observed spectrum (Fig. 51b), confirming the C_{4v} global minimum for MnB_{16}^-.

The size of the MnB_{16}^- drum is very similar to that of CoB_{16}^-. The correlation of the CMOs of MnB_{16}^- with the atomic orbitals of Mn and B is shown in Fig. 53 to illustrate the bonding between Mn and the B_{16} tube. There are two unpaired electrons in the closely-lying HOMO and HOMO-1. The HOMO is a delocalized orbital on the B_{16} moiety, while the HOMO-1 is mainly from the Mn $3d_{z^2}$ orbital. The C_{4v} symmetry of MnB_{16}^- is distorted from the perfect D_{8d} symmetry due to the Jahn-Teller effect. The chemical bonding in MnB_{16}^- was analyzed using AdNDP, as displayed in Fig. 54. The bonding picture in MnB_{16}^- is very similar to that in CoB_{16}^- (Fig. 50). There is one unpaired $3d_{z^2}$ electron on Mn and one 16c-1e $\pi-\pi$ bond, making MnB_{16}^- an interesting diradical species.[92]

5.2.3. TaB_{20}^-: The largest metal-centered boron drum. Following the discoveries of the CoB_{16}^- and MnB_{16}^- drums, the question was if drums with larger diameters would be possible. The CoB_{18}^- cluster was found to be a planar structure with Co being an integral part of the boron triangular lattice.[95] However, RhB_{18}^- was shown to have a D_{9d} drum competing for the global minimum with a planar isomer in which the Rh atom was part of the boron planar network.[93] Clearly the size of the central metal atom matters. Considering that the Ta atom gave rise to the largest metal-centered boron wheel,[81] it would be interesting to explore if even larger drum could exist for TaB_{20}^-.[94] The findings of planar CoB_{18}^- and RhB_{18}^- clusters, in which the

18

metal dopants became part of boron network was exciting, suggesting that extended 2D boron nanostructures decorated with metal atoms, i.e, metallo-borophenes, would be possible. This concept has been expounded in a recent Perspective article.[49] Here the largest boron drum, TaB_{20}^-, is reviewed.

The PE spectra of TaB_{20}^- at two photon energies are shown in Fig. 55,[94] compared with the simulated spectra of the two lowest-lying isomers. The spectrum at 193 nm displayed five broad features, while a weak feature X' was resolved at 266 nm between X and A (Fig. 55a). Overall, the observed spectra were well-resolved and suggested the co-existence of a minor isomer. Global minimum searches revealed two isomers **1** and **2** to compete for the global minimum, as shown in Fig. 56. Isomer **1** was a Ta-centered eighteen-membered drum with a B_2 unit on the top. Isomer **2** was a D_{10d} twenty-membered boron drum, which was only 0.81 kcal/mol higher than isomer **1** at the CCSD(T) level of theory. The simulated spectrum of isomer **1** was in good agreement with the observed main features (X, A−D) (Fig. 55c), while that of isomer **2** agreed well with the peak X', providing considerable credence for the coexistence of the two species in the cluster beam. The slightly higher stability of isomer **1** implied that the D_{10d} isomer **2** had likely reached the size limit for metal-centered boron drums. The D_{10d} TaB_{20}^- set the record for coordination number. Its chemical bonding was analyzed using AdNDP, as shown in Fig. 57. The overall bonding picture was reminiscent of that in CoB_{16}^- (Fig. 50) and MnB_{16}^- (Fig. 54).

5.3. $Ta_2B_6^-$: A hexa-boron bipyramidal cluster

There have been relatively few experimental studies on di-metal doped boron clusters. Previous PES and theoretical studies found that, in diauride boron clusters ($Au_2B_n^-$), the two Au atoms are covalently bonded to the periphery of the boron clusters in $Au_2B_3^-$, $Au_2B_6^-$, $Au_2B_7^-$, similar to dihydrides (Fig. 40).[74,76,77] Transition metals with open *d* shells have strong covalent interactions with boron and can form a variety of interesting structures, as seen above for the mono-transition metal doped boron clusters. A joint PES and theoretical study showed that di-tantalum doped boron clusters featured boron atoms building around the Ta−Ta dimer, as shown in Fig. 58.[101] The Ta−Ta distance increased as the number of boron atoms increased, suggesting that an extra boron atom might achieve a closed equatorial ring to yield a highly symmetric bipyramidal cluster.

The PE spectra of $Ta_2B_6^-$ at two photon energies are shown in Fig. 59 with well-resolved spectral bands labeled as X, A−G.[102] There was a large energy gap between bands X and A, indicating a high electronic stability for the neutral Ta_2B_6 with a large HOMO-LUMO gap. The global minimum of $Ta_2B_6^-$ was found indeed to be a perfect bipyramidal D_{6h} hexa-boron cluster, as shown in Fig. 60. The Ta…Ta distance was relatively long, indicating there was no bonding interaction between the two Ta atoms. The calculated VDEs were in excellent agreement with the experimental data, lending considerable evidence to the D_{6h} global minimum for $Ta_2B_6^-$. The $Ta_2B_n^-$ series of clusters were very different from the di-niobium doped gold clusters ($Nb_2Au_n^-$, $n = 2−6$), where the Au atoms nucleate around a multiply-bonded Nb−Nb dimer even in the D_{6h} $Nb_2Au_6^-$ cluster.[171]

Because of its high symmetry and relatively small size, the CMOs of $Ta_2B_6^-$ were sufficient to understand its chemical bonding, as shown in Fig. 61. The HOMO orbital with a single occupation is a non-bonding orbital, mainly of Ta 6s/6p characters. The removal of this non-bonding electron gives rise to a highly stable neutral Ta_2B_6 cluster with little structural change (Fig. 60). The degenerate HOMO-1 and HOMO-1' are π orbitals describing bonding interactions between the Ta atoms and the B_6 ring. The HOMO-2, HOMO-2', and HOMO-5 are three totally delocalized σ orbitals, while the HOMO-3, HOMO-3', and HOMO-6 are three totally delocalized π orbitals. The remaining six CMOs describe B−B σ bonds in the B_6 ring. Overall, the bipyramidal Ta_2B_6 cluster possesses 10 delocalized π electrons and 6 delocalized σ electrons, giving rise to double aromaticity and its high electronic stability.

Interestingly, B_6 rings have been observed in two solid-state boride compounds $Ti_7Rh_4Ir_2B_8$ and $Nb_6Fe_{1-x}Ir_{6+x}B_8$.[172,173] The bipyramidal D_{6h} Ta_2B_6 cluster is reminiscent of the MB_6M motif in the solid-state materials, revealing an intrinsic link between gas phase clusters and condensed matters. Several di-transition metal doped boron clusters have been investigated computationally recently.[174-177] However, these binary clusters represent extremely complex electronic systems and pose huge challenges both theoretically and experimentally. The D_{6h} $Ta_2B_6^-$ cluster was the first gas-phase species containing a planar B_6 ring coordinated by two Ta atoms in an inverse sandwich fashion. As have been shown recently (vide infra), dilanthanide doped boron clusters can form a family of novel inverse sandwich complexes.[103,104]

6. Lanthanide doped boron clusters

The chemistry of lanthanides (Ln) is dominated by trivalency and ionic interactions. Lanthanide borides constitute an important class of materials with wide industrial applications,[178-181] but clusters of lanthanide borides have been rarely investigated until recently.[70,96–100,103,104,182] A joint PE imaging and theoretical study was used to elucidate the electronic structures and chemical bonding of small lanthanum doped boron clusters LaB_n^- (n = 1−3).[97,96] The SmB_6^- cluster was assigned to a C_{2v} structure based on a joint PES and computational study.[98] A similar planar structure for CeB_6^- was reported very recently.[182] A series of Pr-doped boron clusters have been investigated PrB_n^- (n = 3, 4, and 7), revealing unusually low oxidation states for Pr.[99,100] Very recently, a family of dilanthanide boron inverse sandwich complexes $Ln_2B_n^-$ (n = 7−9) have been discovered.[103,104] Here we will focus on the half-sandwich PrB_7^- cluster and the very exciting inverse-sandwiches complexes. Fig. 62 summarizes all the mono-lanthanide doped boron clusters reported recently.

6.1. PrB_7^-: A Pr^{II} coordinated by a doubly aromatic η^7-B_7^{3-} cluster

The PE spectrum of PrB_7^- at 193 nm is shown in Fig. 63,[99] displaying a relatively simple pattern in the low binding energy region. There was a large energy gap between band X and A. Beyond band A, the spectrum became more congested. The global minimum of PrB_7^- was found to have C_{6v} symmetry with a quartet electronic state ($^4B_1$), as shown in Fig. 64. The calculated VDEs of the C_{6v} PrB_7^- was in excellent agreement with the experimental data (Fig. 63), confirming identified global minimum. The Kohn-Sham MO levels of PrB_7^- are shown in Fig. 65, showing a large energy gap between the HOMO ($7a_1$) and the remaining occupied orbitals consistent with the large gap between bands X and A observed experimentally (Fig. 63). The quartet C_{6v} structure has three unpaired electrons $4f^26s^1$ on Pr, resulting in an uncommon Pr^{II} oxidation state in PrB_7^-. Upon electron detachment of the 6s orbital, Pr become the common Pr^{III} oxidation state in PrB_7, which can be $Pr^{III}(\eta^7$-$B_7^{3-})$ with extremely high electronic stability.

Hence, the half-sandwich PrB_7 cluster is a charge transfer complex with two unpaired 4f electrons in Pr^{III}. The bonding in the B_7^{3-} moiety can be better appreciated from the AdNDP analyses, as shown in Fig. 66.[99] Six 2c-2e σ bonds can be seen readily around the peripheral B atoms of the B_7^{3-} ligand. Of particular importance are the two sets of multi-center bonds: three in-plane 7c-2e bonds and three out-of-plane 8c-2e bonds, which represent the π bonding within B_7^{3-} and bonding interactions between the Pr 5dπ orbitals and the B_7^{3-} ligand. The delocalized σ and π bonds in B_7^{3-} are reminiscent of the σ and π bonds in both B_8^{2-} and B_9^-,[25a] giving rise to

double aromaticity because both the σ and π bonds fulfill the Hückel $4N+2$ rule with $N = 1$. The stability of B_7^{3-} can also be understood that the C_{6v} B_7^- cluster was found previously to be a triplet state with two unpaired electrons. The out-of-plane distortion of the C_{6v} B_7^{3-} and also in B_7^- was due to the fact that the B_6 ring was too small to fit the central B atom perfectly.[67] In fact, the slight bowl-shape of B_7^{3-} makes it a more suitable ligand to form half-sandwich complexes than the perfect planar B_8^{2-} and B_9^- species. Since most 4f elements prefer the +3 oxidation state, it was expected that a whole series of lanthanide $Ln^{III}[\eta^7\text{-}B_7^{3-}]$ complexes should exist with tunable magnetic and optical properties.

6.2. $Ln_2B_8^-$ (Ln = La, Pr, Tb): Octa-boron inverse boron sandwiches

Inverse sandwich structures represent a well-known class of transition-metal and actinide compounds consisting of two metal atoms sandwiching an aromatic hydrocarbon molecule.[183-191] The central aromatic molecule can form interesting chemical bonds to the metals on both faces of its planar π-electron system. The D_{6h} $Ta_2B_6^-$ cluster discussed above should be considered the first inverse-sandwich boron complex.[102] It turned out that di-lanthanide doped boron clusters can form a whole family of inverse sandwich complexes with different boron ring sizes, $Ln_2B_n^-$ ($n = 7-9$).[103,104]

The first di-lanthanide boron inverse sandwich cluster was discovered serendipitously during an investigation of Pr-doped boron clusters.[103] Among a whole series of $Pr_2B_n^-$ clusters, the PE spectrum of $Pr_2B_8^-$ (Fig. 67b) was found to be quite simple. Subsequently, the spectrum of $La_2B_8^-$ (Fig. 67a) was also taken and found to be similar to that of $Pr_2B_8^-$. These observations suggested that these clusters must have similar and high symmetry structures. Global minimum searches revealed that the neutral La_2B_8 and Pr_2B_8 both had bipyramidal D_{8h} structures, as shown in Fig. 68, while the anions both had D_{4h} symmetry due to the Jahn-Teller effect.[103] The simulated spectra of the D_{4h} global minima were in excellent agreement with the experimental data (Fig. 67), confirming unequivocally the inverse-sandwich structures for $La_2B_8^-$ and $Pr_2B_8^-$.

The bonding between the two lanthanide atoms and the B_8 ring can be understood from the orbital correlation diagram shown in Fig. 69 for the case of La_2B_8. It was found that the antibonding π_2 orbital of B_8 interacted strongly with the d-δ_u orbital of La…La by symmetry, forming a special δ bond, which was reminiscent of a similar δ bond first found in uranium

inverse-sandwich compounds.[190,191] This unique $(d\text{-}p)\delta$ bonding significantly stabilizes the $1e_{2u}$ orbitals, underlying the high stability of the inverse-sandwich complexes. The AdNDP analyses on La_2B_8 revealed a relatively simple and intuitive bonding picture, as shown in Fig. 70. There are eight 2c-2e σ bonds on the peripheral B_8 ring. The three 10c-2e σ bonds in the first row mainly involves the delocalized σ bonding within B_8 ring, constituting to σ aromaticity. The second row consists of three 10c-2e π bonds and two 10c-1e π bonds, constituting to π aromaticity for triplet states.[192] Thus, the Ln_2B_8 inverse sandwiches can be considered to be doubly aromatic.

Neutral D_{8h} La_2B_8 has a triplet ground state with two unpaired electrons, while the ground state of D_{8h} Pr_2B_8 is characterized to be septuplet with six unpaired electrons.[103] All Ln_2B_8 complexes are expected to display similar structures and bonding, providing opportunities to design highly magnetic Ln_2B_8 sandwich complexes, as well as 1D magnetic nanowires.

6.3. $La_2B_n^-$ ($n = 7$ and 9): Inverse boron sandwiches with different ring sizes

Following the discovery of the $Ln_2B_8^-$ inverse sandwiches, two questions arose: 1) Could similar inverse sandwiches be formed with other monocyclic boron ring sizes? 2) What was the trend and nature of the bonding in such complexes? To answer these questions, the $La_2B_7^-$ and $La_2B_9^-$ clusters were recently investigated.[104]

The PE spectra of $La_2B_7^-$ and $La_2B_9^-$ at 193 nm are shown in Figs. 71a and 72a, respectively. The spectrum of $La_2B_7^-$ was relatively complex in comparison with that of $La_2B_8^-$ (Fig. 67a). However, global minimum searches found that it also possessed an inverse sandwich structure (Fig. 73) with a triplet ground state (D_{7h}, $^3A_2'$). The simulated spectrum of the D_{7h} $La_2B_7^-$ was found to agree well with the experimental data (Fig. 73b), confirming the inverse sandwich structure. The PE spectrum of $La_2B_9^-$ (Fig. 72a) turned out to be very sharp and even simpler than that of $La_2B_8^-$, immediately suggesting that it must have the high symmetry inverse sandwich structure. This conjecture was borne out from global minimum searches that found that the most stable structure of $La_2B_9^-$ was indeed the D_{9h} inverse sandwich with a closed shell electronic structure ($^1A_1'$). The simulated spectrum of the D_{9h} $La_2B_9^-$ global minimum was almost in quantitative agreement with the experiment (Fig. 72b), unequivocally confirming the inverse sandwich structure.

6.3.1. Chemical bonding in La$_2$B$_n^-$ (n = 7−9). It was clear that there existed a whole class of lanthanide inverse sandwiches with n = 7–9. Their bonding can be understood systematically on the basis of the interactions between the La…La atom pair and the local orbitals on the B$_n$ ring moiety, similar to that shown in Fig. 69 for La$_2$B$_8$. Fig. 74 presents the schematic MO diagrams of all three La$_2$B$_n^-$ (n = 7−9). The differences among La$_2$B$_7^-$, La$_2$B$_8^-$, and La$_2$B$_9^-$ lie only in the occupation of the d$_\delta$ HOMO orbitals. The d$_\delta$ HOMO in La$_2$B$_7^-$ is half-filled with two unpaired electrons, resulting in its triplet ground state, similar to the neutral La$_2$B$_8$ inverse sandwich.[103] The additional electron in La$_2$B$_8^-$ makes it a doublet ground state, leading to the Jahn-Teller distortion from D$_{8h}$ symmetry in La$_2$B$_8$ to D$_{4h}$ in La$_2$B$_8^-$. In La$_2$B$_9^-$, the d$_\delta$ HOMO is fully occupied, resulting in a closed-shell system and the exceptional stability for this large inverse sandwich. The stabilities of these inverse sandwich structures can be glimpsed from the large HOMO-LUMO gap revealed in the MO diagram of Fig. 74. The LUMO mainly originates from the La 6s orbitals, which only have weak interactions with the B$_n$ rings. The 4f orbitals of the La atoms are also radially too contracted to contribute to chemical bonding with the B$_n$ rings, so they form a nonbonding f-band just above the LUMO region. The 5d orbitals of the La atoms then play the most important role in bonding with the B$_n$ ring in the inverse sandwich systems due to its large radial distribution and unique angular orientation. As can be seen in Fig. 74, the 5dδ orbitals of the La atoms are stabilized via bonding with the π$_2$ orbital of the B$_n$ ring, forming the (d-p)δ bonding-type for the HOMO in all three inverse sandwiches. A similar δ bonding MO was found previously in inverse sandwiches of uranium with arenes.[190,191] The 5dπ orbitals overlap with the σ$_{r1}$ orbital of the B$_n$ ring − this (d-p)π bonding accounts for most of the interactions between La…La and the B$_n$ ring. The 5dσ orbitals of the La atoms overlap with the σ$_{r0}$ orbital of the B$_n$ ring, and this (d-p)σ bonding-type also plays a tangible role in stabilizing the system.

6.3.2. AdNDP bonding analyses. The bonding in La$_2$B$_7^-$ and La$_2$B$_9^-$ was further analyzed using the AdNDP method, as shown in Fig. 75. Similar that in La$_2$B$_8$ (Fig. 70), Four types of bonds were found for the inverse sandwiches: 1) n 2c-2e σ bonds on the periphery of the B$_n$ ring; 2) three delocalized nc-2e σ bonds from the interactions between the La 5d$_\pi$ and 5d$_\sigma$ orbitals and the in-plane delocalized σ bonds within the B$_n$ ring; 3) three delocalized nc-2e π bonds from the interactions between the La 5d$_\pi$ and 5d$_\sigma$ orbitals and the out-of-plane delocalized π bonds of the B$_n$ ring; 4) two (d-p)δ bonds due to the interactions of the La dδ orbitals and the π

orbitals of the B_n ring. The three delocalized nc-2e σ and π bonds give rise to double aromaticity for the inverse sandwiches, each satisfying the $4n + 2$ Hückel rule. The only difference between the bonding in $La_2B_7^-$ and $La_2B_9^-$ lies at the (d-p)δ bonds. In $La_2B_7^-$, the (d-p)δ orbitals (Fig. 76) are half-filled, resulting in two 9c-1e (d-p)δ bonds. This situation is exactly the same as in the neutral La_2B_8 inverse sandwich, which features two 10c-1e (d-p)δ bonds (Fig. 70), whereas the $La_2B_8^-$ anion contains one 10c-2e (d-p)δ bond and one 10c-1e (d-p)δ bond. In $La_2B_9^-$, the (d-p)δ orbitals (Fig. 74) are completely filled, resulting in two 11c-2e (d-p)δ bonds. Thus, the stability of the inverse sandwiches is derived from the double aromaticity and the unique (d-p)δ bonds between the La atoms and the boron rings. The extraordinary stability of the $La_2B_9^-$ inverse sandwich can be understood from the two full (d-p)δ bonds, whereas the $La_2B_7^-$ and $La_2B_8^-$ inverse sandwiches only have partial (d-p)δ bonds.

6.3.3. Stability and size limit of di-lanthanide boron inverse sandwiches. To further quantify the stabilities of the $La_2B_n^-$ ($n = 7-9$) inverse sandwiches, the metal-metal interactions and the binding energies of the complexes were exmined.[104] The binding energies were calculated as: $La_2B_n^- \rightarrow 2La + B_n^-$. All three complexes showed strong binding energies between the La atoms and the boron ring, increasing from 340.4 kcal/mol for $n = 7$ to 372.4 kcal/mol for $n = 9$. This trend is also consistent with the increasing (d-p)δ bond order, as discussed above. As the size of the B_n ring increases, the metal-boron distances become larger, while the distances between the two La atoms become smaller, indicating gradually weaker metal-boron interactions and stronger metal-metal interactions. As shown in Fig. 73, even though the La…La distance ranging from 3.83 to 3.47 Å is within the La−La single-bond length (3.60 Å based on the self-consistent covalent radius of Pyykkö),[193] there is no clear La−La bond, which is reminiscent of the lack of metal-metal bonding in the Be_2O_2 rhombic structure.[194,195] Instead, the bonding between the two La atoms and between the La atoms and the boron rings is completely by delocalized multi-center bonds. The stabilities of the inverse sandwiches depend mainly on the optimal overlaps between the La 5d orbitals and the 2p orbitals on the B_n ring. If the B_n ring is too large, no effective overlap is possible between the La 5d and the 2p orbitals on the B_n ring. Hence, $La_2B_9^-$ is likely the largest inverse sandwich between lanthanide and boron. The B_{10} ring is probably too large to allow effective La−B interactions to form a stable $La_2B_{10}^-$ inverse sandwich. Preliminary photoelectron data of $La_2B_{10}^-$ showed a more complicated spectral pattern,[196] incommensurate with a high symmetry structure. On the smaller side, it is more

difficult to consider whether the B_6 ring can form lanthanide inverse sandwich structures solely on the basis of the geometrical argument. Preliminary experimental and theoretical data both suggest that it does not have the inverse sandwich global minimum structure.[196]

6.3.4. Electronic design principles for di-lanthanide boron inverse sandwiches. Further insights obtained from the electronic structure and bonding of the $La_2B_n^-$ ($n = 7-9$) inverse sandwiches also indicate that it would not be favorable for $La_2B_6^-$ and $La_2B_{10}^-$ to form inverse sandwiches. Fig. 75 shows that the stabilities of the inverse sandwiches derive from both the double aromaticity and the unique (d-p)δ bonds. Thus, in the $[La(\eta^n\text{-}B_n)La]$ inverse sandwiches, we need $2(n + 6 + y)$ electrons, where $2n$ electrons are for the bonding in the periphery of the B_n ring, 12 electrons for the double aromaticity and $2y$ electrons for the (d-p)δ bonds ($y = 1$, half-filled; $y = 2$, fully filled). According to the $2(n + 6 + y)$ rule, we would need 28 electrons for a closed-shell La_2B_6 inverse sandwich complex ($n = 6$; $y = 2$), but La_2B_6 only has 24 valence electrons, which means that there would be no more electrons for the (d-p)δ bonds. For the $La_2B_6^-$ anion, there would be only one electron for the (d-p)δ bonds, which explains the instability of a $La_2B_6^-$ inverse sandwich structure. It is interesting to note that the Ta_2B_6 cluster with 28 valence electrons was found previously to form a highly stable D_{6h} $Ta(\eta^6\text{-}B_6)Ta$ inverse sandwich (Fig. 60).[102] A similar electronic consideration suggests that a $La_2B_{10}^-$ inverse sandwich would have one extra electron, which would occupy the high energy 6s-based LUMO (Fig. 74), making it energetically unfavorable. Hence, It was concluded that $La_2B_n^-$ ($n = 7-9$) would be the only likely inverse sandwich complexes in term of the size of the B_n ring.[104] On the other hand, the $Ln_2B_8^-$ species can form inverse sandwiches for a range of lanthanide elements for Ln = La, Pr, and Tb.[103] Therefore, it was expected that most lanthanides should also be able to form the inverse sandwiches in the same size range, $[Ln(\eta^n\text{-}B_n)Ln]^-$ ($n = 7-9$).

Given the diverse magnetic properties of the lanthanides, the $Ln_2B_n^-$ ($n = 7-9$) clusters constitute a novel class of inverse sandwich complexes with tunable chemical and physical properties. They not only provide new motifs for bulk borides, but it is also conceivable that some of these inverse sandwiches may be able to be synthesized in solution with appropriate ligand coordination, similar to the actinide arene inverse sandwiches.[190,191,197]

7. Conclusion and perspectives

Combined photoelectron spectroscopy and theoretical studies have systematically elucidated the structures and chemical bonding of anionic boron clusters up to B_{40}^-, revealing a structural landscape with prevalent 2D structures in contrast to bulk boron where 3D polyhedral building blocks dominate. The electron deficiency of boron and the complexity of boron clusters have posed great challenges to establish their global minima and required deliberate and careful joint experimental and theoretical efforts. The 2D boron clusters feature strong peripheral two-center two-electron B−B bonds and delocalized bonds within the cluster plane. Chemical bonding analyses show that all planar boron clusters can be viewed as analogues of polycyclic aromatic hydrocarbons in terms of their π bonding within the molecular planes. Planar boron clusters mainly consist of B_3 triangles. However, the strong peripheral B−B bonds cause out-of-plane distortions concomitant with the appearance of tetragonal, pentagonal or hexagonal vacancies, as cluster size increases. The observation of the hexagonal vacancy in the B_{36} cluster provided the first experimental evidence of borophenes consisting of a triangular lattice with periodic hexagonal vacancies.[34] The B_{26}^- cluster is the smallest boron cluster to feature a hexagonal vacancy,[43] while B_{35}^- is the smallest cluster to contain a double hexagonal vacancy.[37] The B_{40} cluster was found to be an exceptionally stable fullerene-like cage with a large HOMO-LUMO gap and was named borospherene.[56] Minor borospherene isomers were observed for smaller boron clusters, B_{28}^- and B_{29}^-, whereas the global minimum of B_{39}^- was found to be a chiral borospherene.[57] It is interesting to note that hydrogen-terminated boron clusters form stable and well-known borane cages, $B_nH_n^{2-}$ ($n = 5-12$),[1] as shown in Fig. 76, whereas bare boron clusters all prefer 2D structures (Fig. 1). The transition from 2D to 3D structures in B_nH_x type clusters as a function of x is expected, as has been studied for B_6H_x and $B_{12}H_x$.[198-200] With increased understanding of the mechanisms of the formation of boranes and the increased synthetic yields,[201-203] it is conceivable that novel planar boranes may be synthesized, as has been demonstrated for sandwich-type metal-borane compounds.[204-207]

Metal doping greatly extends the chemistry of boron clusters and results in unprecedented structures and novel chemical bonding. Metal-centered borometallic molecular wheels (M©B_n, n = 8−10) have been observed, giving rise to the largest coordination number in a molecular plane.[81,208] The first observation of the metal-stabilized boron drum (CoB$_{16}^-$) set a record of coordination and was named one of the "Molecules of the Year" by *Chem. & Eng. News*,[209] but this record was quickly broken by the observation of the RhB$_{18}^-$ and TaB$_{20}^-$ drums.[93,94] The

finding of transition metal atoms that become part of the boron planar network has led to the possibility of metallo-borophenes.[49] The recent observation of new families of inverse sandwiches in di-lanthanide boron clusters open up another new avenue of investigations.

It is clear that the field of size-selected boron clusters is a rich area of scientific research still full of surprises and unexpected results. For bare boron clusters, the structures and bonding beyond $B_{40}^{-/0}$ are still wide open. An interesting question is: are the clusters continuing to be planar or cage-like? Theoretical calculations have been done on several larger boron clusters, suggesting both 2D and 3D structures.[210-222] However, whether these structures are the global minima or not will need to be corroborated by further calculations or ultimately experiments. Because of the complex potential energy surfaces, any given calculation can only explore a small portion of the vast configuration space and it would be extremely challenging to locate the true global minima, as shown in the case of B_{80}.[130-135] Metal-boron binary clusters provide unlimited opportunities to discover new structures and bonding. Only a selected few mono- and di-meal doped boron clusters have been studied thus far experimentally, as reviewed here. Theoretical calculations have explored a number of large doped-boron clusters and suggested interesting tubular and endohedral structures.[223-226] Note that Metal-boron binary clusters are even more challenging for global minimum searches.

Experimentally, the primary technique to study size-elected boron clusters has been anion photoelectron spectroscopy, as discussed in this review. However, larger bare boron clusters or complex binary clusters also pose major challenges experimentally for the anion photoelectron spectroscopic technique. Large clusters tend to yield broad spectral bands and featureless photoelectron spectra, which become less valuable to compare with theoretical calculations. Clearly major innovation in the photoelectron spectroscopic techniques will be required to study large boron clusters by preparing cold cluster anions and improving spectral resolution. Ion mobility was shown to be valuable to provide structural information for size-selected boron clusters.[50] Application of ion mobility to larger boron clusters would be interesting. An emerging technique for boron clusters is infrared spectroscopy, which has been applied recently to B_{13}^{+}.[227] Extension of this technique to large size-selected boron clusters would be extremely valuable to help elucidate the structures of complex boron clusters.

The chemical properties of bulk transition metal borides remain fairly unexplored. For example, the recent observations of tungsten borides as electrocatalysts for the hydrogen

evolution reaction and the dependence of the catalytic effects on the boride stoichiometry and surface structures are extremely interesting.[228,229] Size-selected W-B binary clusters would be excellent model systems to understand the observed catalytic effects of the bulk borides. Boron is known to be the "rule breaker" in chemistry due to its electron deficiency that underlies the great variety of structures and bonding observed in size-selected boron clusters and in bulk boron and borides. It is anticipated that the "unruly" boron will continue to produce surprises and unexpected breakthroughs. Further research on size-selected boron clusters will unveil more interesting structures and novel chemical bonding, paving the foundations for new boron compounds and boron-based nanomaterials.

Conflicts of Interest

There are no conflicts to declare.

Acknowledgements

Notes and references

1   W. N. Lipscomb, *Science*, 1977, **196**, 1047–1055.
2   K. Wade, in *Advances in Inorganic Chemistry and Radiochemistry*, eds. H. J. Emeléus and A. G. Sharpe, Academic Press, 1976, vol. 18, pp. 1–66.
3   B. Douglas and S.-M. Ho, *Structure and Chemistry of Crystalline Solids*, Springer-Verlag, New York, 2006.
4   B. Albert and H. Hillebrecht, *Angew. Chem. Int. Ed.*, 2009, **48**, 8640–8668.
5   A. R. Oganov, J. Chen, C. Gatti, Y. Ma, Y. Ma, C. W. Glass, Z. Liu, T. Yu, O. O. Kurakevych and V. L. Solozhenko, *Nature*, 2009, **457**, 863–867.
6   (a) R. Kawai and J. H. Weare, *J. Chem. Phys.*, 1991, **95**, 1151-1159; (b) R. Kawai and J. H. Weare, *Chem. Phys. Lett.*, 1992, **191**, 311-314.
7   V. Bonacic-Koutecky, P. Fantucci and J. Koutecky, *Chem. Rev.*, 1991, **91**, 1035–1108.
8   H. Kato, K. Yamashita and K. Morokuma, *Chem. Phys. Lett.*, 1992, **190**, 361–366.

9   I. Boustani, *Chem. Phys. Lett.*, 1995, **240**, 135–140.

10   (a) A. Ricca and C. W. Bauschlicher Jr, *Chem. Phys. Lett.*, 1996, **208**, 233-242; (b) A. Ricca and C. W. Bauschlicher Jr, *J. Chem. Phys.*, 1997, **106**, 2317-2322.

11   I. Boustani, *Phys. Rev. B*, 1997, **55**, 16426–16438.

12   L. Hanley and S. L. Anderson, *J. Phys. Chem.*, 1987, **91**, 5161–5163.

13   L. Hanley and S. L. Anderson, *J. Chem. Phys.*, 1988, **89**, 2848–2860.

14   L. Hanley, J. L. Whitten and S. L. Anderson, *J. Phys. Chem.*, 1988, **92**, 5803–5812.

15   P. A. Hintz, M. B. Sowa, S. A. Ruatta and S. L. Anderson, *J. Chem. Phys.*, 1991, **94**, 6446–6458.

16   M. B. Sowa-Resat, J. Smolanoff, A. Lapicki and S. L. Anderson, *J. Chem. Phys.*, 1997, **106**, 9511–9522.

17   P. A. Hintz, S. A. Ruatta and S. L. Anderson, *J. Chem. Phys.*, 1998, **92**, 292.

18   S. A. Ruatta, L. Hanley and S. L. Anderson, *J. Chem. Phys.*, 1990, **91**, 226.

19   S. J. La Placa, P. A. Roland and J. J. Wynne, *Chem. Phys. Lett.*, 1992, **190**, 163–168.

20   S.-J. Xu, J. M. Nilles, D. Radisic, W.-J. Zheng, S. Stokes, K. H. Bowen, R. C. Becker and I. Boustani, *Chem. Phys. Lett.*, 2003, **379**, 282–286.

21   H. J. Zhai, L. S. Wang, A. N. Alexandrova and A. I. Boldyrev, *J. Chem. Phys.*, 2002, **117**, 7917–7924.

22   A. N. Alexandrova, A. I. Boldyrev, H. J. Zhai, L. S. Wang, E. Steiner and P. W. Fowler, *J. Phys. Chem. A*, 2003, **107**, 1359–1369.

23   H. J. Zhai, L. S. Wang, A. N. Alexandrova, A. I. Boldyrev and V. G. Zakrzewski, *J. Phys. Chem. A*, 2003, **107**, 9319–9328.

24   H. J. Zhai, B. Kiran, J. Li and L. S. Wang, *Nat. Mater.*, 2003, **2**, 827-833.

25   (a) H. J. Zhai, A. N. Alexandrova, K. A. Birch, A. I. Boldyrev and L. S. Wang, *Angew. Chem. Int. Ed.*, 2003, **42**, 6004–6008; (b) L. L. Pan, J. Li and L. S. Wang, *J. Chem. Phys.*, 2008, **129**, 024302.

26   A. N. Alexandrova, A. I. Boldyrev, H. J. Zhai and L. S. Wang, *J. Phys. Chem. A*, 2004, **108**, 3509–3517.

27   B. Kiran, S. Bulusu, H. J. Zhai, S. Yoo, X. C. Zeng and L. S. Wang, *Proc. Natl. Acad. Sci.*, 2005, **102**, 961–964.

28   A. P. Sergeeva, D. Yu. Zubarev, H. J. Zhai, A. I. Boldyrev and L. S. Wang, *J. Am. Chem. Soc.*, 2008, **130**, 7244-7246.

29   W. Huang, A. P. Sergeeva, H. J. Zhai, B. B. Averkiev, L. S. Wang and A. I. Boldyrev, *Nat. Chem.*, 2010, **2**, 202-206.

30   A. P. Sergeeva, B. B. Averkiev, H. J. Zhai, A. I. Boldyrev and L. S. Wang, *J. Chem. Phys.*, 2011, **134**, 224304.

31   Z. A. Piazza, W. L. Li, C. Romanescu, A. P. Sergeeva, L. S. Wang and A. I. Boldyrev, *J. Chem. Phys.*, 2012, **136**, 104310.

32   A. P. Sergeeva, Z. A. Piazza, C. Romanescu, W.-L. Li, A. I. Boldyrev and L. S. Wang, *J. Am. Chem. Soc.*, 2012, **134**, 18065–18073.

33   I. A. Popov, Z. A. Piazza, W. L. Li, L. S. Wang and A. I. Boldyrev, *J. Chem. Phys.*, 2013, **139**, 144307.

34   Z. A. Piazza, H. S. Hu, W. L. Li, Y. F. Zhao, J. Li and L. S. Wang, *Nat. Commun.*, 2014, **5**, 3113.

35   W. L. Li, Y. F. Zhao, H. S. Hu, J. Li and L. S. Wang, *Angew. Chem. Int. Ed.*, 2014, **53**, 5540–5545.

36   Z. A. Piazza, I. A. Popov, W. L. Li, R. Pal, X. C. Zeng, A. I. Boldyrev and L. S. Wang, *J. Chem. Phys.*, 2014, **141**, 034303.

37   W. L. Li, Q. Chen, W. J. Tian, H. Bai, Y. F. Zhao, H. S. Hu, J. Li, H. J. Zhai, S. D. Li and L. S. Wang, *J. Am. Chem. Soc.*, 2014, **136**, 12257–12260.

38   W. L. Li, R. Pal, Z. A. Piazza, X. C. Zeng and L. S. Wang, *J. Chem. Phys.*, 2015, **142**, 204305.

39   Y. J. Wang, Y. F. Zhao, W. L. Li, T. Jian, Q. Chen, X. R. You, T. Ou, X. Y. Zhao, H. J. Zhai, S. D. Li, J. Li and L. S. Wang, *J. Chem. Phys.*, 2016, **144**, 064307.

40   H. R. Li, T. Jian, W. L. Li, C. Q. Miao, Y. J. Wang, Q. Chen, X. M. Luo, K. Wang, H. J. Zhai, S. D. Li and L. S. Wang, *Phys. Chem. Chem. Phys.*, 2016, **18**, 29147–29155.

41   Q. Chen, W. J. Tian, L. Y. Feng, H. G. Lu, Y. W. Mu, H. J. Zhai, S. D. Li and L. S. Wang, *Nanoscale*, 2017, **9**, 4550–4557.

42   J. Czekner, L. F. Cheung and L. S. Wang, *J. Phys. Chem. C*, 2017, **121**, 10752–10759.

43   X.-M. Luo, T. Jian, L.-J. Cheng, W. L. Li, Q. Chen, R. Li, H. J. Zhai, S. D. Li, A. I. Boldyrev, J. Li and L. S. Wang, *Chem. Phys. Lett.*, 2017, **683**, 336–341.

44   Q. Chen, W. L. Li, X. Y. Zhao, H. R. Li, L. Y. Feng, H. J. Zhai, S. D. Li and L. S. Wang, *Eur. J. Inorg. Chem.*, 2017, **2017**, 4546–4551.

45   A. N. Alexandrova, A. I. Boldyrev, H. J. Zhai and L. S. Wang, *Coord. Chem. Rev.*, 2006, **250**, 2811–2866.

46   A. P. Sergeeva, I. A. Popov, Z. A. Piazza, W. L. Li, C. Romanescu, L. S. Wang and A. I. Boldyrev, *Acc. Chem. Res.*, 2014, **47**, 1349–1358.

47   L. S. Wang, *Int. Rev. Phys. Chem.*, 2016, **35**, 69–142.

48   L. S. Wang, in *International Symposium on Clusters and Nanomaterials*, International Society for Optics and Photonics, 2016, vol. 10174, p. 1017402.

49   (a) W. L. Li, X. Chen, T. Jian, T. T. Chen, J. Li and L. S. Wang, *Nat. Rev. Chem.*, 2017, **1**, 0071; (b) W. L. Li, H. S. Hu, Y. F. Zhao, X. Chen, T. T. Chen, T. Jian, L. S. Wang and J. Li, *Sci. Sin. Chim.*, 2018, **48**, 98-107.

50   E. Oger, N. R. M. Crawford, R. Kelting, P. Weis, M. M. Kappes and R. Ahlrichs, *Angew. Chem. Int. Ed.*, 2007, **46**, 8503–8506.

51   (a) L. Cheng, *J. Chem. Phys.*, 2012, **136**, 104301; (b) J. Lv, Y. Wang, L. Zhu and Y. Ma, *Nanoscale*, 2014, **6**, 11692–11696.

52   C. Romanescu, D. J. Harding, A. Fielicke and L. S. Wang, *J. Chem. Phys.*, 2012, **137**, 014317.

53   A. I. Boldyrev and L. S. Wang, *Phys. Chem. Chem. Phys.*, 2016, **18**, 11589-11605.

54   D. Y. Zubarev and A. I. Boldyrev, *J. Comput. Chem.*, 2007, **28**, 251–268.

55   D. Y. Zubarev and A. I. Boldyrev, *Phys. Chem. Chem. Phys.*, 2008, **10**, 5207–5217.

56   H. J. Zhai, Y. F. Zhao, W. L. Li, Q. Chen, H. Bai, H. S. Hu, Z. A. Piazza, W. J. Tian, H. G. Lu, Y. B. Wu, Y. W. Mu, G. F. Wei, Z. P. Liu, J. Li, S. D. Li and L. S. Wang, *Nat. Chem.*, 2014, **6**, 727-731.

57   Q. Chen, W. L. Li, Y. F. Zhao, S. Y. Zhang, H. S. Hu, H. Bai, H. R. Li, W. J. Tian, H. G. Lu, H. J. Zhai, S. D. Li, J. Li and L. S. Wang, *ACS Nano*, 2015, **9**, 754–760.

58   (a) A. J. Mannix, *et al. Science*, 2015, **350**, 1513-1516; (b) B. Feng, *et al. Nat. Chem.*, 2016, **8**, 563-568.

59   B. B. Averkiev and A. I. Boldyrev, *Russ. J. Gen. Chem.*, 2008, **78**, 769–773.

60   K. Ito, Z. Pu, Q.-S. Li and P. von R. Schleyer, *Inorg. Chem.*, 2008, **47**, 10906–10910.

61   Z. Pu, K. Ito, P. v. R. Schleyer and Q.-S. Li, *Inorg. Chem.*, 2009, **48**, 10679–10686.

62   (a) J. Guo, W. Yao, Z. Li and S. Li, *Sci. China Ser. B Chem.*, 2009, **52**, 566–570; (b) C. Miao, J. Guo and S. Li, *Sci. China Ser. B Chem.*, 2009, **52**, 900–904.

63   Z. Pu, M. Ge and Q. Li, *Sci. China Chem.*, 2010, **53**, 1737–1745.

64   A. N. Alexandrova, H. J. Zhai, L. S. Wang and A. I. Boldyrev, *Inorg. Chem.*, 2004, **43**, 3552–3554.

65   A. N. Alexandrova, A. I. Boldyrev, H. J. Zhai and L. S. Wang, *J. Chem. Phys.*, 2005, **122**, 054313.

66   T. B. Tai and M. T. Nguyen, *Chem. Phys.*, 2010, **375**, 35–45.

67   C. Romanescu, A. P. Sergeeva, W. L. Li, A. I. Boldyrev and L. S. Wang, *J. Am. Chem. Soc.*, 2011, **133**, 8646–8653.

68   T. R. Galeev, C. Romanescu, W. L. Li, L. S. Wang and A. I. Boldyrev, *J. Chem. Phys.*, 2011, **135**, 104301.

69　W. L. Li, C. Romanescu, T. R. Galeev, L. S. Wang and A. I. Boldyrev, *J. Phys. Chem. A*, 2011, **115**, 10391–10397.

70　J. Gu, C. Wang, Y. Cheng, L. Zhang and X. Yang, *Comput. Theor. Chem.*, 2014, **1049**, 67–74.

71　T. Jian, G. V. Lopez and L. S. Wang, *J. Phys. Chem. B*, 2016, **120**, 1635–1640.

72　J. Moon, J. S. Lim and J. Kim, *Int. J. Quantum Chem.*, 2017, **117**, e25324.

73　T. Jian, L. F. Cheung, T. T. Chen and L. S. Wang, *Angew. Chem. Int. Ed.*, 2017, **56**, 9551–9555.

74　H. J. Zhai, L. S. Wang, D. Y. Zubarev and A. I. Boldyrev, *J. Phys. Chem. A*, 2006, **110**, 1689–1693.

75　H. J. Zhai, C.-Q. Miao, S. D. Li and L. S. Wang, *J. Phys. Chem. A*, 2010, **114**, 12155–12161.

76　Q. Chen, H.-J. Zhai, S.-D. Li and L. S. Wang, *J. Chem. Phys.*, 2013, **138**, 084306.

77　Q. Chen, H. Bai, H.-J. Zhai, S.-D. Li and L. S. Wang, *J. Chem. Phys.*, 2013, **139**, 044308.

78　H. Bai, H. J. Zhai, S.-D. Li and L. S. Wang, *Phys. Chem. Chem. Phys.*, 2013, **15**, 9646–9653.

79　C. Romanescu, T. R. Galeev, W.-L. Li, A. I. Boldyrev and L. S. Wang, *Angew. Chem. Int. Ed.*, 2011, **50**, 9334–9337.

80　W. L. Li, C. Romanescu, T. R. Galeev, Z. A. Piazza, A. I. Boldyrev and L. S. Wang, *J. Am. Chem. Soc.*, 2012, **134**, 165–168.

81　T. R. Galeev, C. Romanescu, W. L. Li, L. S. Wang and A. I. Boldyrev, *Angew. Chem. Int. Ed.*, 2012, **51**, 2101–2105.

82　C. Romanescu, T. R. Galeev, A. P. Sergeeva, W. L. Li, L. S. Wang and A. I. Boldyrev, *J. Organomet. Chem.*, 2012, **721–722**, 148–154.

83　C. Romanescu, T. R. Galeev, W. L. Li, A. I. Boldyrev and L. S. Wang, *Acc. Chem. Res.*, 2013, **46**, 350–358.

84　Y. Liao, C. Leticia Cruz, P. von R. Schleyer and Z. Chen, *Phys. Chem. Chem. Phys.*, 2012, **14**, 14898–14904.

85　W. L. Li, C. Romanescu, Z. A. Piazza and L. S. Wang, *Phys. Chem. Chem. Phys.*, 2012, **14**, 13663–13669.

86　C. Romanescu, T. R. Galeev, W. L. Li, A. I. Boldyrev and L. S. Wang, *J. Chem. Phys.*, 2013, **138**, 134315.

87　W. L. Li, A. S. Ivanov, J. Federič, C. Romanescu, I. Černušák, A. I. Boldyrev and L. S. Wang, *J. Chem. Phys.*, 2013, **139**, 104312.

88　I. A. Popov, W. L. Li, Z. A. Piazza, A. I. Boldyrev and L. S. Wang, *J. Phys. Chem. A*, 2014, **118**, 8098–8105.

89　C. Xu, L. Cheng, and J. Yang, *J. Chem. Phys.*, 2014, **141**, 124301.

90　N. M. Tam, H. T. Pham, L. V. Duong, M. P. Pham-Ho and M. T. Nguyen, *Phys. Chem. Chem. Phys.*, 2015, **17**, 3000–3003.

91　I. A. Popov, T. Jian, G. V. Lopez, A. I. Boldyrev and L. S. Wang, *Nat. Commun.*, 2015, **6**, 8654.

92　T. Jian, W. L. Li, I. A. Popov, G. V. Lopez, X. Chen, A. I. Boldyrev, J. Li and L. S. Wang, *J. Chem. Phys.*, 2016, **144**, 154310.

93　T. Jian, W. L. Li, X. Chen, T. T. Chen, G. V. Lopez, J. Li and L. S. Wang, *Chem. Sci.*, 2016, **7**, 7020–7027.

94　W. L. Li, T. Jian, X. Chen, H. R. Li, T. T. Chen, X. M. Luo, S. D. Li, J. Li and L. S. Wang, *Chem. Commun.*, 2017, **53**, 1587–1590.

95　W. L. Li, T. Jian, X. Chen, T. T. Chen, G. V. Lopez, J. Li and L. S. Wang, *Angew. Chem. Int. Ed.*, 2016, **55**, 7358–7363.

96　S.-B. Cheng, C. Berkdemir and A. W. Castleman, *Proc. Natl. Acad. Sci.*, 2015, 201504714.

97　S.-B. Cheng, C. Berkdemir and A. W. Castleman, *Phys. Chem. Chem. Phys.*, 2014, **16**, 533–539.

98   P. J. Robinson, X. Zhang, T. McQueen, K. H. Bowen and A. N. Alexandrova, *J. Phys. Chem. A*, 2017, **121**, 1849–1854.

99   T. T. Chen, W. L. Li, T. Jian, X. Chen, J. Li and L. S. Wang, *Angew. Chem. Int. Ed.*, 2017, **56**, 6916–6920.

100 X. Chen, T. T. Chen, W. L. Li, J. B. Lu, L. J. Zhao, T. Jian, H. S. Hu, L. S. Wang and J. Li, *Inorg. Chem.*, 2019, **58**, 411-418.

101 L. Xie, W. L. Li, C. Romanescu, X. Huang and L. S. Wang, *J. Chem. Phys.*, 2013, **138**, 034308.

102 W. L. Li, L. Xie, T. Jian, C. Romanescu, X. Huang and L. S. Wang, *Angew. Chem. Int. Ed.*, 2014, **53**, 1288–1292.

103 W. L. Li, T. T. Chen, D. H. Xing, X. Chen, J. Li and L. S. Wang, *Proc. Natl. Acad. Sci. (USA)*, 2018, **115**, E6972-E6977.

104 T. T. Chen, W. L. Li, J. Li and L. S. Wang, *Chem. Sci.*, 2019, **10**, 2534-2542.

105 (a) H. J. Zhai, L. M. Wang, S. D. Li and L. S. Wang, *J. Phys. Chem. A*, 2007, **111**, 1030–1035; (b) H. J. Zhai, S. D. Li and L. S. Wang, *J. Am. Chem. Soc*., 2007, **129**, 9254-9255; (c) S. D. Li, H. J. Zhai and L. S. Wang, *J. Am. Chem. Soc*., 2008, **130**, 2573-2579; (d) H. J. Zhai, C. Q. Miao, S. D. Li and L. S. Wang, *J. Phys. Chem. A*, 2010, **114**, 12155-12161; (e) H. J. Zhai, J. C. Guo, S. D. Li and L. S. Wang, *ChemPhysChem*, 2011, **12**, 2549-2553; (f) Q. Chen, H. J. Zhai, S. D. Li and L. S. Wang, *J. Chem. Phys*., 2012, **137**, 044307; (g) H. Bai, H. J. Zhai, S. D. Li and L. S. Wang, *Phys. Chem. Chem. Phys*., 2013, **15**, 9646-9653; (h) Q. Chen, H. Bai, H. J. Zhai, S. D. Li and L. S. Wang, *J. Chem. Phys*., 2013, **139**, 044308; (i) H. J. Zhai, Q. Chen, H. Bai, H. G. Lu, W. L. Li, S. D. Li and L. S. Wang, *J. Chem. Phys*., 2013, **139**, 174301.

106 H. J. Zhai, Q. Chen, H. Bai, S. D. Li and L. S. Wang, *Acc. Chem. Res.*, 2014, **47**, 2435–2445.

107 N. X. Truong, M. Haertelt, B. K. A. Jaeger, S. Gewinner, W. Schöllkopf, A. Fielicke and O. Dopfer, *Int. J. Mass Spectrom.*, 2016, **395**, 1–6.

108 N. X. Truong, B. K. A. Jaeger, S. Gewinner, W. Schöllkopf, A. Fielicke and O. Dopfer, *J. Phys. Chem. C*, 2017, **121**, 9560–9571.

109 X. Wu, S.-J. Lu, X. Liang, X. Huang, Y. Qin, M. Chen, J. Zhao, H.-G. Xu, R. B. King and W. Zheng, *J. Chem. Phys.*, 2017, **146**, 044306.

110 S.-J. Lu, X.-L. Xu, G.-J. Cao, H.-G. Xu and W.-J. Zheng, *J. Phys. Chem. C*, 2018, **122**, 2391–2401.

111 S.-J. Lu, X.-L. Xu, G.-J. Cao, H.-G. Xu and W.-J. Zheng, *J. Chem. Phys.*, 2018, **149**, 174314.

112 K. Exner and P. von R. Schleyer, *Science*, 2000, **290**, 1937–1940.

113 Z.-X. Wang and P. von R. Schleyer, *Science*, 2001, **292**, 2465–2469.

114 R. M. Minyaev, T. N. Gribanova, A. G. Starikov and V. I. Minkin, *Mendeleev Commun.*, 2001, **11**, 213–214.

115 L. M. Wang, W. Huang, B. B. Averkiev, A. I. Boldyrev and L. S. Wang, *Angew. Chem. Int. Ed.*, 2007, **46**, 4550–4553.

116 B. B. Averkiev, D. Y. Zubarev, L. M. Wang, W. Huang, L. S. Wang and A. I. Boldyrev, *J. Am. Chem. Soc.*, 2008, **130**, 9248–9250.

117 Y. Pei and X. C. Zeng, *J. Am. Chem. Soc.*, 2008, **130**, 2580–2592.

118 B. B. Averkiev, L. M. Wang, W. Huang, L. S. Wang and A. I. Boldyrev, *Phys. Chem. Chem. Phys.*, 2009, **11**, 9840–9849.

119 L. M. Wang, B. B. Averkiev, J. A. Ramilowski, W. Huang, L. S. Wang and A. I. Boldyrev, *J. Am. Chem. Soc.*, 2010, **132**, 14104–14112.

120 T. R. Galeev, W. L. Li, C. Romanescu, I. Černušák, L. S. Wang and A. I. Boldyrev, *J. Chem. Phys.*, 2012, **137**, 234306.

121 (a) W. L. Li, C. Romanescu, T. Jian and L. S. Wang, *J. Am. Chem. Soc.*, 2012, **134**, 13228–13231; (b) D. Z. Li, Q. Chen, Y. B. Wu, H. G. Lu and S. D. Li, *Phys. Chem. Chem. Phys.*, 2012, **14**, 14769-14774.

122 L. S. Wang, H. Cheng and J. Fan, *J. Chem. Phys.*, 1995, **102**, 9480–9493.

123 D. J. Wales and J. P. K. Doye, *J. Phys. Chem. A*, 1997, **101**, 5111–5116.

124 A. N. Alexandrova and A. I. Boldyrev, *J. Chem. Theory Comput.*, 2005, **1**, 566–580.

125 (a) Y. F. Zhao, X. Chen and J. Li, *Nano Res* 2017, **10**, 3407-3420; (b) X. Chen, Y. F. Zhao, L. S. Wang and J. Li, *Comput. Theor. Chem.*, 2017, **1107**, 57–65.

126 X. Chen, Y. F. Zhao, Y. Y. Zhang and J. Li, *J. Comput. Chem.*, 2019, **40**, 1105-1112.

127 H. W. Kroto, J. R. Heath, S. C. O'Brien, R. F. Curl and R. E. Smalley, *Nature*, 1985, **318**, 162.

128 S. Iijima, *Nature*, 1991, **354**, 56.

129 K. S. Novoselov, A. K. Geim, S. V. Morozov, D. Jiang, Y. Zhang, S. V. Dubonos, I. V. Grigorieva and A. A. Firsov, *Science*, 2004, **306**, 666–669.

130 N. Gonzalez Szwacki, A. Sadrzadeh and B. I. Yakobson, *Phys. Rev. Lett.*, 2007, **98**, 166804.

131 D. L. V. K. Prasad and E. D. Jemmis, *Phys. Rev. Lett.*, 2008, **100**, 165504.

132 H. Li, N. Shao, B. Shang, L.-F. Yuan, J. Yang and X. C. Zeng, *Chem. Commun.*, 2010, **46**, 3878–3880.

133 J. Zhao, L. Wang, F. Li and Z. Chen, *J. Phys. Chem. A*, 2010, **114**, 9969–9972.

134 S. De, A. Willand, M. Amsler, P. Pochet, L. Genovese and S. Goedecker, *Phys. Rev. Lett.*, 2011, **106**, 225502.

135 F. Li, P. Jin, D. Jiang, L. Wang, S. B. Zhang, J. Zhao and Z. Chen, *J. Chem. Phys.*, 2012, **136**, 074302.

136 (a) I. Boustani and A. Quandt, *Euro. Phys. Lett.*, 1997, **39**, 527-532; (b) A. Gindulyte, W. N. Lipscomb and N. L. Massa, *Inorg. Chem.*, 1998, **37**, 6544-6545.

137 X. Yang, Y. Ding and J. Ni, *Phys. Rev. B*, 2008, **77**, 041402.

138 H. Tang and S. Ismail-Beigi, *Phys. Rev. Lett.*, 2007, **99**, 115501.

139 E. S. Penev, S. Bhowmick, A. Sadrzadeh and B. I. Yakobson, *Nano Lett.*, 2012, **12**, 2441–2445.

140 X. Wu, J. Dai, Y. Zhao, Z. Zhuo, J. Yang and X. C. Zeng, *ACS Nano*, 2012, **6**, 7443–7453.

141 Q. Chen, T. T. Chen, H. R. Li, Xi. Y. Zhao, W. J. Chen, J. J. Zhai, S. D. Li and L. S. Wang, *Nanoscale,* 2019, DOI: 10.1039/C9NR01524H.

142 (a) A. J. Mannix, Z. Zhang, N. P. Guisinger, B. I. Yakobson and M. C. Hersam, *Nat. Nanotech.,* 2018*,* **13**, 444-450; (b) Z. Zhang, E. S. Penev and B. I. Yakobson, *Chem. Soc. Rev.,* 2017*,* **46**, 6746-6763.

143 T. B. Tai and M. T. Nguyen, *Phys. Chem. Chem. Phys.*, 2015, **17**, 13672–13679.

144 S. Goedecker, *J. Chem. Phys.*, 2004, **120**, 9911–9917.

145 J. Zhao, X. Huang, R. Shi, H. Liu, Y. Su and R. B. King, *Nanoscale*, 2015, **7**, 15086–15090.

146 A. Savin, R. Nesper, S. Wengert and T. F. Fässler, *Angew. Chem. Int. Ed. Engl.*, 1997, **36**, 1808–1832.

147 A. Hirsch, Z. Chen and H. Jiao, *Angew. Chem. Int. Ed.*, 2000, **39**, 3915–3917.

148 T. B. Tai and M. T. Nguyen, *Nanoscale*, 2015, **7**, 3316–3317.

149 M. Zhou, N. Tsumori, L. Andrews and Q. Xu, *J. Phys. Chem. A*, 2003, **107**, 2458–2463.

150 H. Braunschweig, R. D. Dewhurst, K. Hammond, J. Mies, K. Radacki and A. Vargas, *Science*, 2012, **336**, 1420.

151 H. Braunschweig, K. Radacki and A. Schneider, *Science*, 2010, **328**, 345–347.

152 J. S. Lu, S. H. Su, M. C. Yang, X. T. Wen, J. Z. Xie and M. D. Su, *Organometallics,* 2016, **35**, 3924-3931.

153 L. F. Cheung, J. Czekner, G. S. Kocheril and L. S. Wang, *J. Chem. Phys.*, 2019, **150**, 064304.

154 I. Vurgaftman, J. R. Meyer and L. R. Ram-Mohan, *J. Appl. Phys.*, 2001, **89**, 5815.

155 D. Madouri and M. Ferhat, *Phys. Stat. Sol. B*, 2005, **242**, 2856.

156 S. Cui, W. Feng, H. Hua, Z. Feng and Y. Wang, *Comput. Mater. Sci.*, 2010, **47**, 968.

157 S. Bagci and B. G. Yalcin, *J. Phys. D: Appl. Phys.*, 2015, **48**, 475304.

158 R. . P. Shahri and A. Akhtar, *Chin. Phys. B*, 2017, **26**, 093107.

159 P. Pyykko, *Chem. Rev.*, 1988, **88**, 563.

160 A. N. Alexandrova, E. Koyle and A. I. Boldyrev, *J. Mol. Model.*, 2006, **12**, 569–576.

161 L. S. Wang, *Phys. Chem. Chem. Phys.*, 2010, **12**, 8694-8705.

162 Y. Yuan and L. Cheng, *J. Chem. Phys.*, 2013, **138**, 024301.

163 L. Liu, D. Moreno, E. Osoria, A. C. Castro, S. Pan, P. K. Chattaraj, T. Heine and G. Merino, *RCC Adv.*, 2016, **6**, 27177-27182.

164 W. Sun, X. Xia, C. Lu, X. Kuang and A. Hermann, *Phys. Chem. Chem. Phys.*, 2018, **20**, 23740-23746.

165 P. F. Li, X. D. Du, J. J. Wang, C. Lu and H. H. Chen, *J. Phys. Chem. C*, 2018, **122**, 20000-20005.

166 (a) B. L. Chen, W. G. Sun, X. Y. Kuang, C. Lu, X. X. Xia, H. X. Shi and G. L. Gutsev, *Phys. Chem. Chem. Phys.*, 2018, **20**, 30376-30383; (b) B. L. Chen, W. G. Sun, X. Y. Kuang, C. Lu, X. X. Xia, H. X. Shi and G. Maroulis, *Inorg. Chem.*, 2018, **57**, 343-350.

167 X. Y. Zhao, X. M. Lou, X. X. Tian, H. G. Lu and S. D. Li, *J. Cluster Sci.*, 2019, **30**, 115-121.

168 X. C. Shao, X. Qu, S. Y. Liu, L. H. Yang, J. H. Yang, X. H. Liu, X. Zhong, S. Sun, G. Vaitheeswaran and J. Lv, *RSC Adv.*, 2019, **9**, 2870-2876.

169 W. L. Li, T. T. Chen, Z. Y. Jiang, W. J. Chen, H. S. Hu, L. S. Wang and J. Li. *Chin. J. Chem. Phys.*, 2019, **31**, 241-247.

170 W. An, S. Bulusu, Y. Gao, and X. C. Zeng, *J. Chem. Phys.*, 2016, **124**, 154310.

171 (a) T. Jian, L. F. Cheung, J. Czekner, T. T. Chen, G. V. Lopez, W. L. Li and L. S. Wang, *Chem. Sci.*, 2017, **8**, 7528-7536; (b) T. Jian, L. F. Cheung, T. T. Chen, G. V. Lopez, W. L. Li and L. S. Wang, *Int. J. Mass Spectrom.*, 2018, **434**, 7-16.

172 B. P. T. Fokwa and M. Hermus, *Angew. Chem. Int. Ed.*, 2012, **51**, 1702–1705.

173 M. Mbarki, R. St. Touzani and B. P. T. Fokwa, *Angew. Chem. Int. Ed.*, 2014, **53**, 13174–13177.

174 B. Wang, L. Xie, X. J. Liu, W. J. Chen, Y. F. Zhang and X. Huang, *Eur. J. Inorg. Chem.*, 2018, **7**, 950-950.

175 A. Q. Hao, B. Z. Xue and J. F. Jia, *J. Mol. Modeling*, 2019, **25**, article no. 27.

176 H. T. Pham and M. T. Nguyen, *Phys. Chem. Chem. Phys.*, 2018, **20**, 26072-26082.

177 A. Q. Hao, B. Z. Xue and J. F. Jia, *Mat. Chem. Phys.*, 2018, **205**, 1-8.

178 J. P. Scheifers, Y. Zhang and B. P. T. Fokwa, *Acc. Chem. Res.*, 2017, **50**, 2317-2325.

179 A. Sussardi, T. Tanaka, A. U. Khan, L. Schlapbach, T. Mori, *J. Materiomics* 2015, **1**, 196-204.

180 G. Akopov, M. T. Yeung and R. B. Kaner, *Adv. Mater.* 2017, **29**,1604506.

181 S. Careco, D. Portrhault, C. Boissiere, N. Mezailles and C. Sanchez, *Chem. Rev.*, 2013, **113**, 7981-8065.

182 J. L. Mason, H. Harb, C. D. Huizenga, J. C. Ewigleben, J. E. Topolski, H. P. Hratchian and C. C. Jarrold, *J. Phys. Chem. A*, 2019, **123**, 2040-2048.

183 A. Schier, J. M. Wallis, G. Müller and H. Schmidbaur, *Angew. Chem. Int. Ed.,* 1986, **25**, 757-759.

184 A. Streitwieser and K. A. Smith, *J. Mol. Struc-THEOCHEM*, 1988, **163**, 259-265.

185 T. Arliguie, M. Lance, M. Nierlich, J. Vigner and M. Ephritikhine, *J. Chem. Soc., Chem. Commun.*, 1994, 847-848.

186 W. J. Evans, G. W. Nyce and J. W. Ziller, *Angew. Chem. Int. Ed.*, 2000, **39**, 240-242.

187 W. H. Monillas, G. P. Yap and K. H. Theopold, *Angew. Chem. Int. Ed.*, 2007, **46**, 6692-6694.

188 S. Krieck, H. Görls, L. Yu, M. Reiher and M. Westerhausen, *J. Am. Chem. Soc.*, 2009, **131**, 2977-2985.

189 O. T. Summerscales, X. Wang and P. P. Power, *Angew. Chem. Int. Ed.*, 2010, **49**, 4788-4790.

190 P. L. Diaconescu, P. L. Arnold, T. A. Baker, D. J. Mindiola and C. C. Cummins, *J. Am. Chem. Soc.*, 2000, **122**, 6108-6109.

191 P. L. Diaconescu and C. C. Cummins, *J. Am. Chem. Soc.*, 2002, **124**, 7660-7661.

192 N. C. Baird, *J. Am. Chem. Soc.*, 1972, **94**, 4941-4948.

193 P. Pyykkö, *J. Phys. Chem. A*, 2014, **119**, 2326-2337.

194 W. L. Li, J. B. Lu, L. Zhao, R. Ponec, D. L. Cooper, J. Li and G. Frenking, *J. Phys. Chem. A*, 2018, **122**, 2816-2822.

195 Q. Zhang, W. L. Li, L. Zhao, M. Chen, M. Zhou, J. Li and G. Frenking, *Chem. Eur. J.*, 2017, **23**, 2035-2039.

196 T. T. Chen, W. L. Li, W. J. Chen, J. Li and L. S. Wang, unpublished results.

197 S. T. Liddle, *Coord. Chem. Rev.*, 2015, **293**, 211-227.

198 J. K. Olson and A. I. Boldyrev, *J. Phys. Chem. A*, 2013, **117**, 1614-1620.

199 H. Bai and S. D. Li, *J. Clust. Sci.*, 2011, **22**, 525-535.

200 M. R. Fagiani, L. L. Zeonjuk, T. K. Esser, D. Gabel, T. Heine, K. R. Asmis and J. Warneke, *Chem. Phys. Lett.*, 2015, **625**, 48-52.

201 X. M. Chen, N. N. Ma, Q. F. Zhang, J. Wang, X. G. Feng, C. G. Wei, L. S. Wang, J. Zhang and X. Chen, *J. Am. Chem. Soc.*, 2018, **140**, 6718-6726.

202 X. M. Chen, N. N. Ma, X. R. Liu, C. G. Wei, C. C. Cui, B. L. Cao, Y. H. Guo, L. S. Wang, Q. F. Gu and X. Chen, *Angew. Chem. Int. Ed.*, 2019, **58**, 2720-2724.

203 Q. Y. Zhai, R. D. Dewhurst, H. Braunschweig and X. Chen, *Angew. Chem. Int. Ed.*, 2019, **58**, 3268-3278.

204 S. Ghosh, M. Shang and T. P. Fehlner, *J. Am. Chem. Soc.*, 1999, **121**, 7451-7452.

205 S. Ghosh, M. Shang, Y. Li and T. P. Fehlner, *Angew. Chem. Int. Ed.*, 2001, **40**, 1125-1128.

206 S. Ghosh, A. M. Beatty and T. P. Fehlner, *J. Am. Chem. Soc.*, 2001, **123**, 9188-9189.

207 S. Ghosh, B. C. Noll and T. P. Fehlner, *Dalton. Trans.*, 2008, 371-378.

208 T. Heine and G. Meino, *Angew. Chem. Int. Ed.*, 2012, **51**, 4275-4276.

209 S. K. Ritter, *Chem & Eng News*, 2015, **93**, 27 (December 21 issue)

220 A. B. Rahane and V. Kumar, *Nanoscale*, 2015, **7**, 4055-4062.

221 L. Sai, X. Wu, N. Gao, J. Zhao and R. B. King, *Nanoscale*, 2017, **9**, 13905-13909.

222 H. T. Pham, J. T. Muya, F. Buendia, A. Ceulemans and M. T. Nguyen, *Phys. Chem. Chem. Phys.*, 2019, **21**, 7039-7044.

223 J. Lv, Y. Wang, L. Zhang, H. Lin, J. Zhao and Y. Ma, *Nanoscale*, 2015, **7**, 10482-10489.

224 N. M. Tam, L. V. Duong, H. T. Pham, M. T. Nguyen and M. P. Pham-Ho, *Phys. Chem. Chem. Phys.*, 2019, **21**, 8365-8375.

225 X. Dong, S. Jalife, A. Vasquez-Espinal, J. Barroso, M. Oroco, E. Ravell, J. L. Cabelllos, W. Y. Liang, Z. H. Cui and G. Merino, *Nanoscale*, 2019, **11**, 2143-2147.

226 Y. Tian, D. Wei, Y. Jin, J. Barroso, C. Lu and G. Merino, *Phys. Chem. Chem. Phys.*, 2019, **21**, 6935-6941.

227 M. R. Fagiani, X. W. Song, P. Petkov, S. Debnath, S. Gewinner, W. Schollkopf, T. Heine, A. Fielicke and K. R. Asmis, *Angew. Chem. Int. Ed.*, 2017, **56**, 501-504.

228 H. Park, Y. Zhang, J. P. Scheifers, P. R. Jothi, A. Encinas, and B. P. T. Fokwa, *J. Am. Chem. Soc.*, 2017, **139**, 12915-12918.

229 H. Park, A. Encinas, J. P. Scheifers, Y. Zhang and B. P. T. Fokwa, *Angew. Chem. Int. Ed.*, 2017, **56**, 5575-5578.
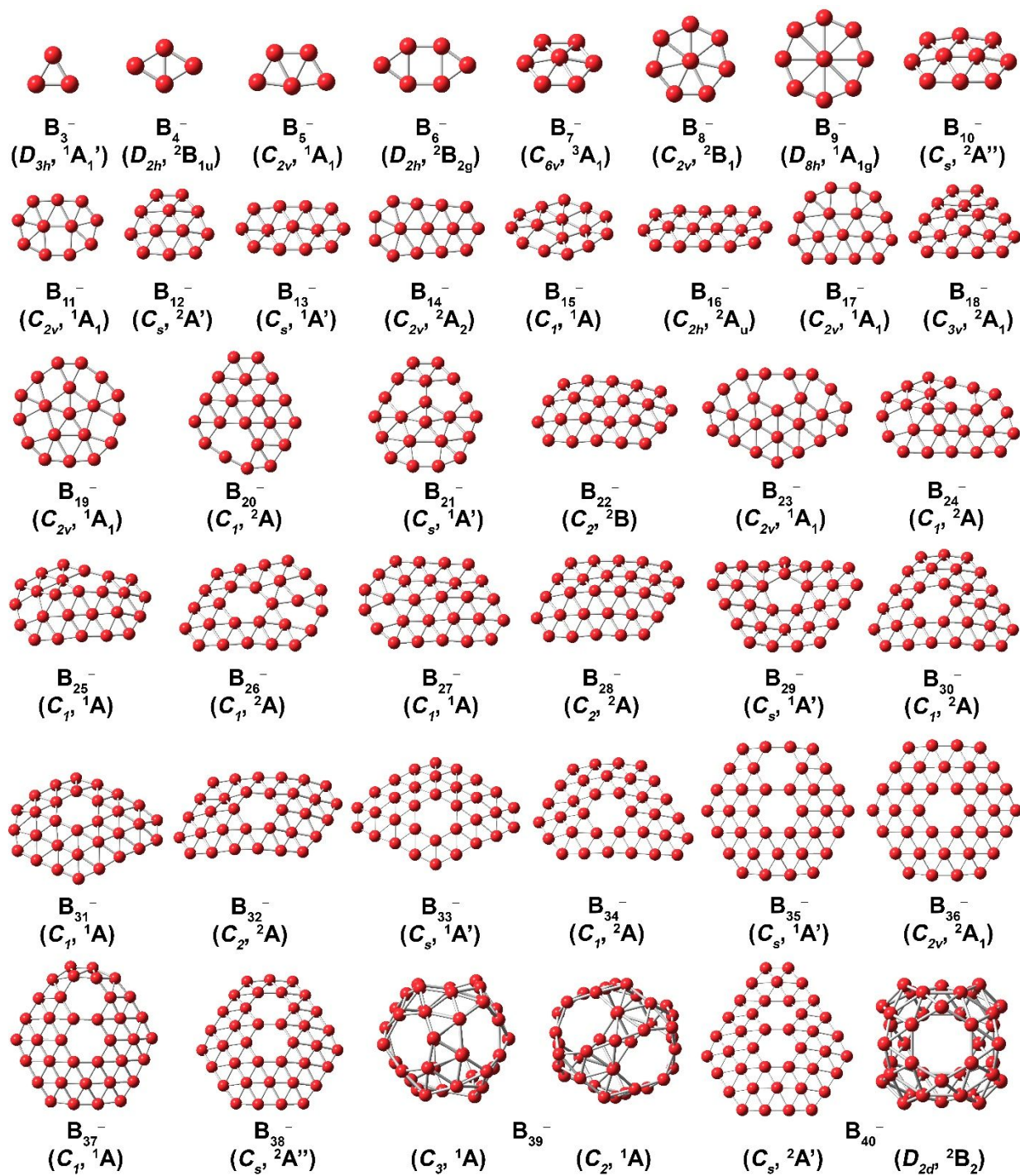
Fig. 1. A summary of the global minima of the B_n^- clusters (n = 3-40) confirmed from joint photoelectron spectroscopy and theoretical calculations. Note that a close-lying three-dimensional isomer is also shown for B_{39}^- and B_{40}^-.
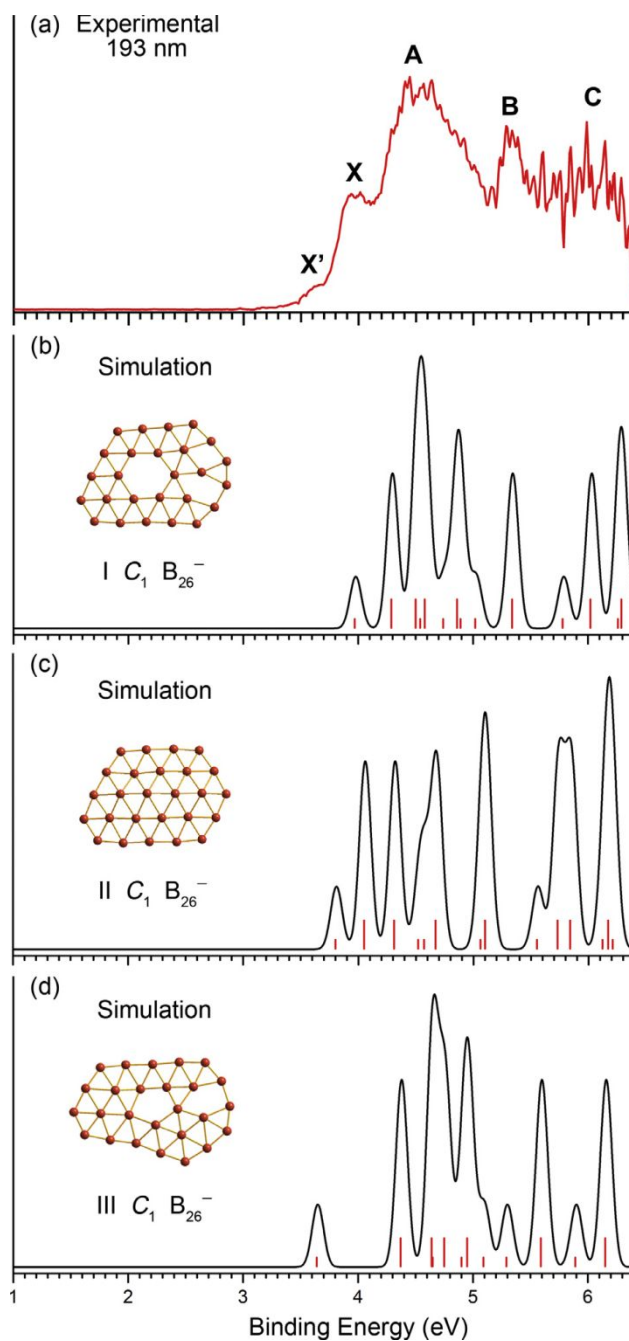
Fig. 2. Photoelectron spectrum of B_{26}^- at 193 nm (a) and comparison with the simulated spectra for three low-lying isomers. Reproduced from ref. 43 with permission from Elsevier, copyright 2016.

(a) B_{26}^-

	I (C_1 ^2A)	II (C_1 ^2A)	III (C_1 ^2A)	IV (C_{2h} ^2A_u)	V (C_s $^2A''$)
ΔE/PBE0	0.46	0.00	0.55	0.01	0.48
ΔE/CCSD(T)	(0.15)	(0.00)	(0.22)	(0.14)	(0.27)
ΔG/CCSD(T)	[0.00]	[0.01]	[0.11]	[0.13]	[0.25]

(b) B_{26}

	VI (C_{2h} ^3B_g)	VII (C_1 ^1A)	VIII (C_2 ^1A)	IX (C_1 ^1A)	X (C_1 ^1A)
ΔE/PBE0	0.00	0.31	0.52	0.57	0.57
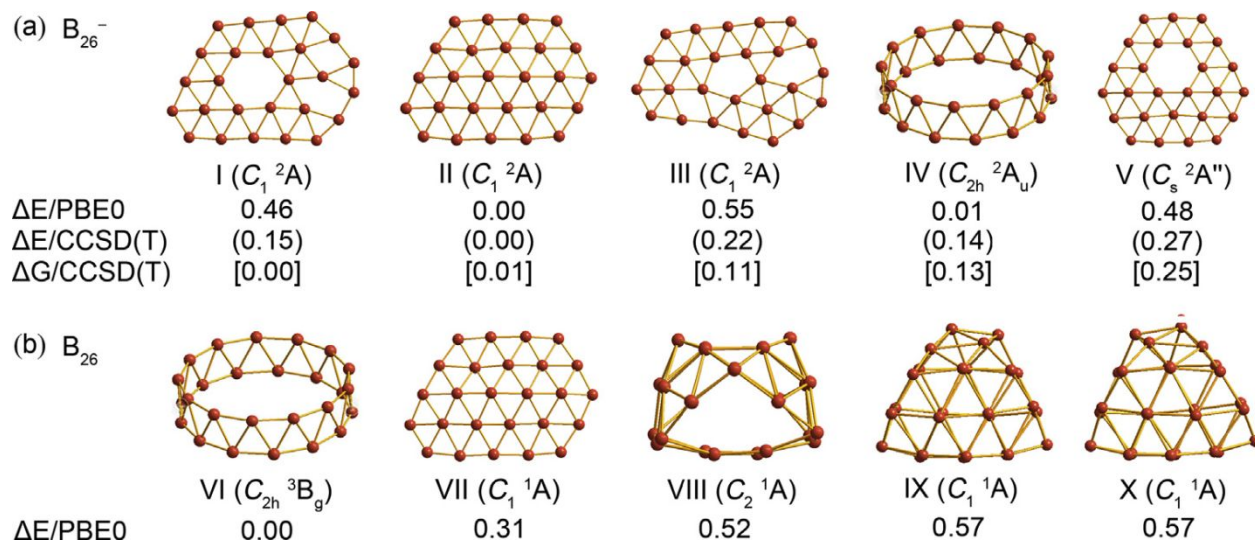
Fig. 3. The global minimum and low-lying isomers of B_{26}^- (a). Relative energies are shown in eV at PBE0/6-311+G*, CCSD(T)/6-311G*//PBE0/6-311+G* (in parenthesis), and CCSD(T)/6-311G*//PBE0/6-311+G* with corrections for Gibbs free energy at 460 K (in square brackets). Low-lying isomers for neutral B_{26} (b) at the PBE0 level are also shown. Reproduced from ref. 43 with permission from Elsevier, copyright 2016.
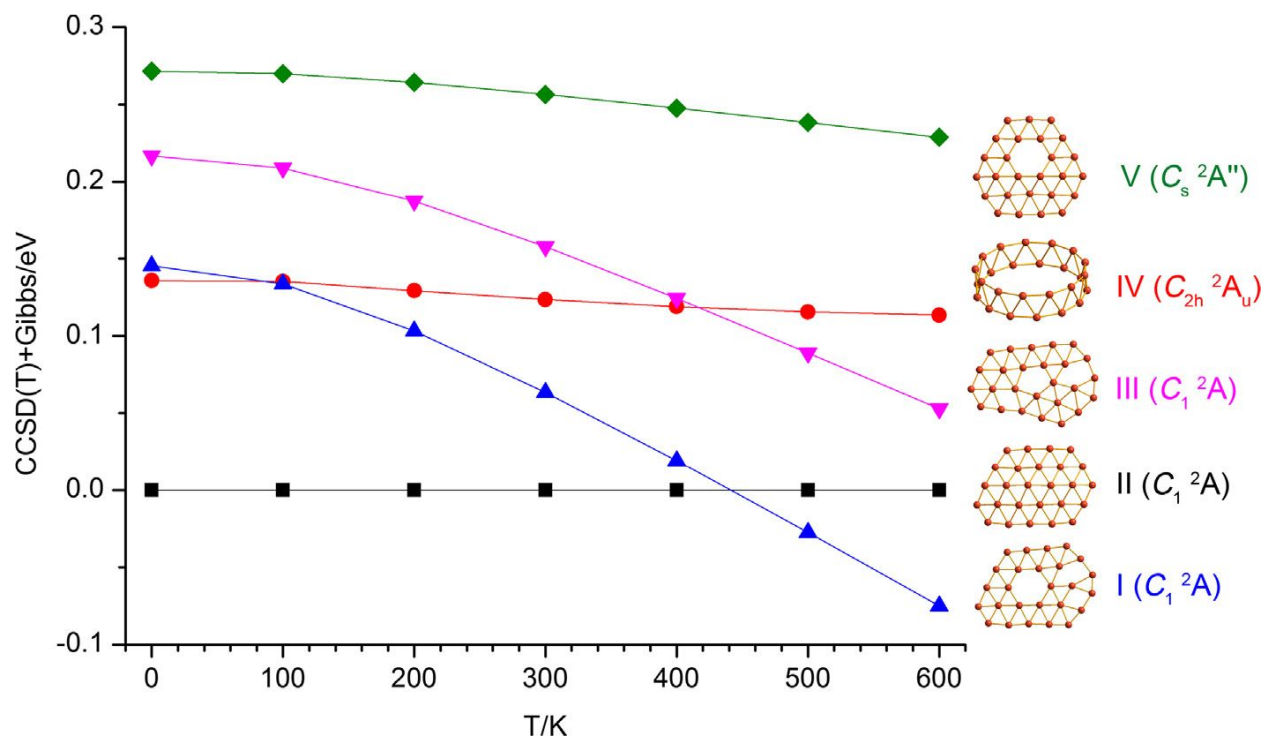
Fig. 4. Gibbs free energies of the top five low-lying isomers of B_{26}^- as a function of temperature. The energies are at the single-point CCSD(T) level with Gibbs free energy corrections at PBE0/6-311+G*, plotted relative to that of isomer II. Reproduced from ref. 43 with permission from Elsevier, copyright 2016.
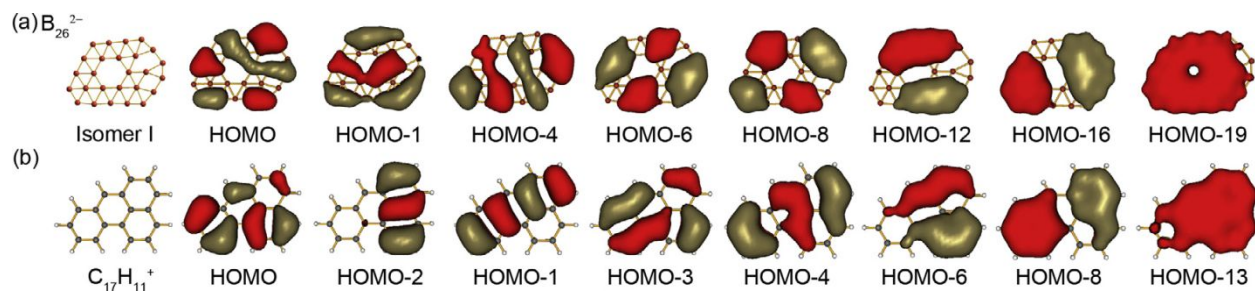
Fig. 5. Comparison of the canonical π molecular orbitals of the closed-shell B_{26}^{2-} (a) and the polycyclic aromatic hydrocarbon $C_{17}H_{11}^{+}$ (b). Reproduced from ref. 43 with permission from Elsevier, copyright 2016.

(a)

16×2c-2e σ bonds
ON=1.78-1.96 |e|

16×3c-2e σ bonds
ON=1.64-1.94 |e|

2×5c-2e π bonds
1×6c-2e π bond
ON=1.60-1.89 |e|

1×5c-2e π bond
ON=1.83 |e|

2×5c-2e π bonds
1×6c-2e π bond
1×4c-2e π bond
ON=1.66-1.93 |e|

(b)

16×2c-2e σ bonds
ON=1.97-1.99 |e|

15×2c-2e σ bonds
ON=1.96-1.98 |e|

2×3c-2e π bonds
1×4c-2e π bond
ON=1.69-1.77 |e|

1×3c-2e π bond
ON=1.72 |e|

3×4c-2e π bonds
1×3c-2e π bond
ON=1.66-1.89 |e|
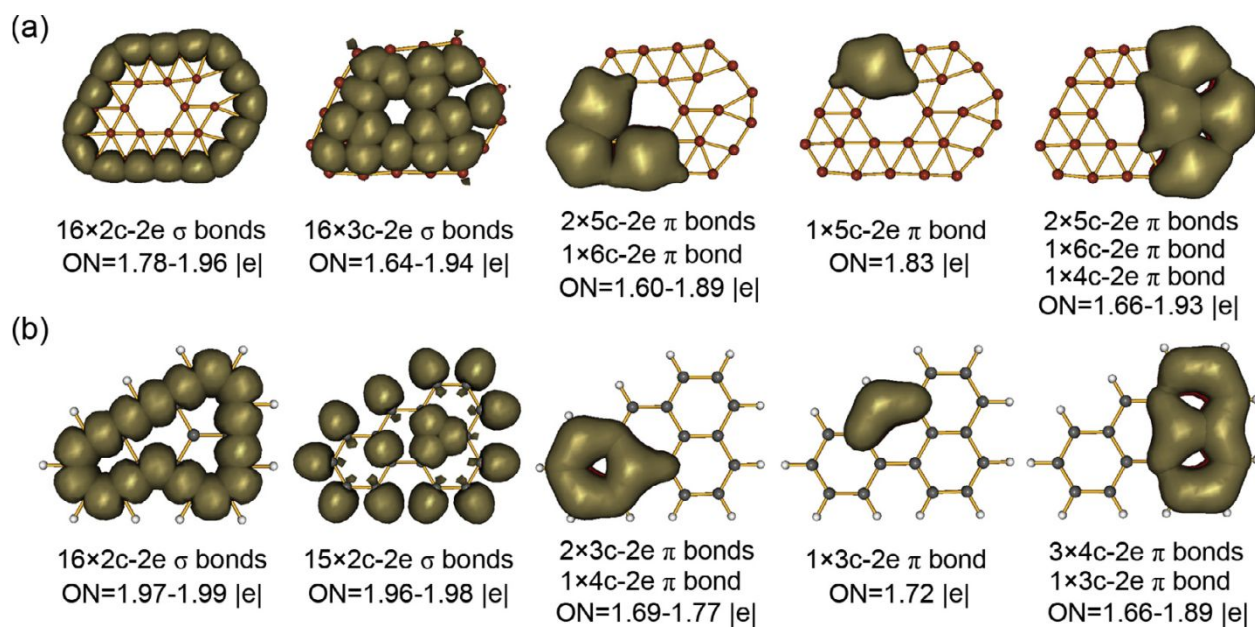
Fig. 6. Comparison of the AdNDP analyses for (a) B_{26}^{2-} corresponding to isomer I of B_{26}^{-} and (b) the polycyclic aromatic hydrocarbon $C_{17}H_{11}^{+}$. The occupation numbers (ONs) are shown. Reproduced from ref. 43 with permission from Elsevier, copyright 2016.
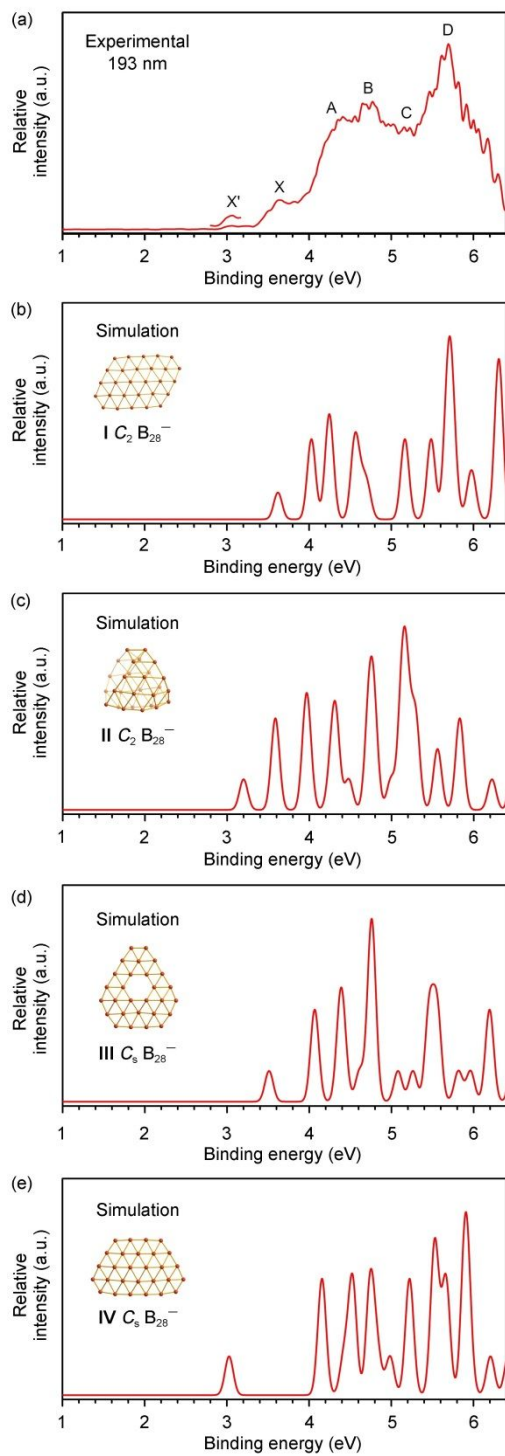
Fig. 7. Photoelectron spectrum of B_{28}^- at 193 nm (a) and comparison with the simulated spectra for four low-lying isomers (b-d). Reproduced from ref. 39 with permission from AIP Publishing, copyright 2016.
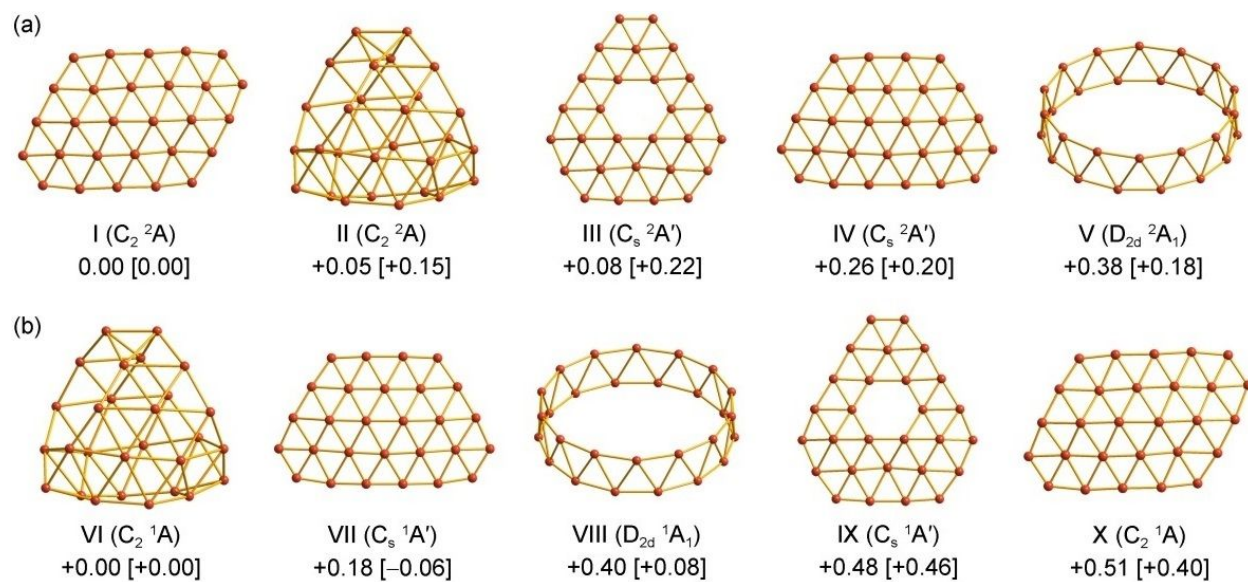
Fig. 8. The optimized structures for B_{28}^- and B_{28}. (a) The global minimum (I) and four low-lying isomers (II−V) of B_{28}^- at the PBE0/6-311+G* level. (b) The global minimum (VI) and four low-lying isomers (VII−X) of B_{28} at the PBE0/6-311+G* level. Relative energies are given in eV at CCSD(T)/6-311G*//PBE0/6-311+G* and PBE0/6-311+G* (in square brackets) levels. Reproduced from ref. 39 with permission from AIP Publishing, copyright 2016.
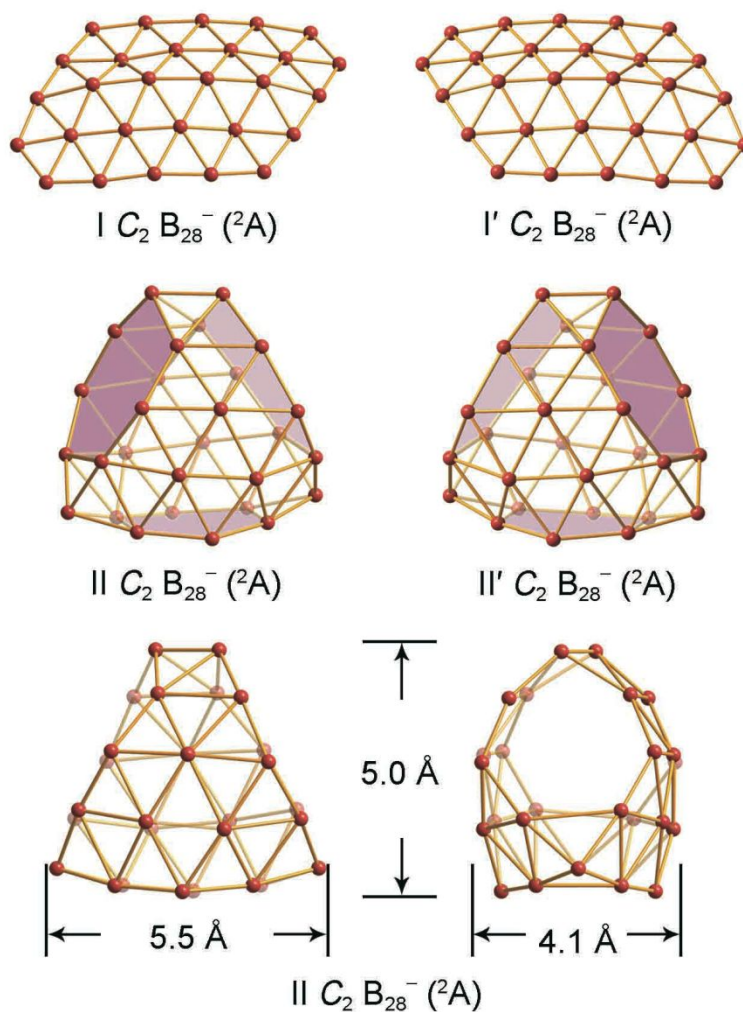
Fig. 9. The enantiomers of the chiral global minimum and the seashell isomer II of B_{28}^- and the dimensions of the seashell cage at the PBE0/6-311+G* level. The two B_7 rings on the waist and the B_6 ring at the bottom of the seashell isomer are shaded for easier viewing. Reproduced from ref. 39 with permission from AIP Publishing, copyright 2016.
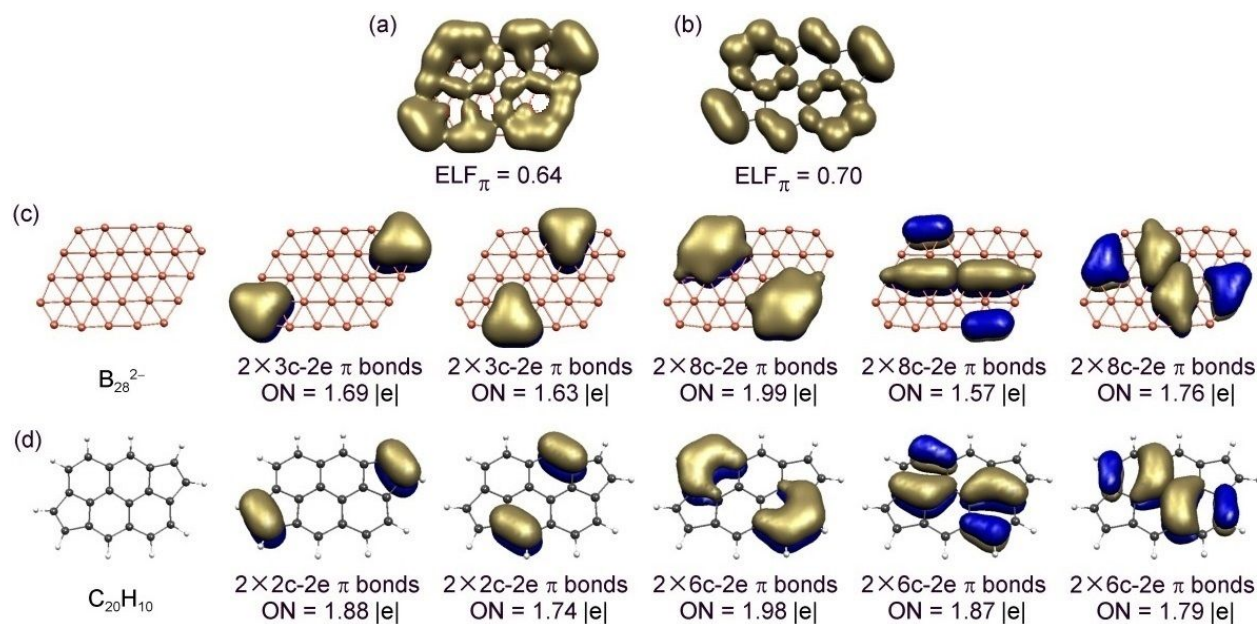
Fig. 10. Chemical bonding analyses for the quasi-planar global minimum of B_{28}^- using the planarized closed-shell C_{2h} B_{28}^{2-}. (a) The ELFπ for B_{28}^{2-}. (b) The ELFπ for $C_{20}H_{10}$. (c) The Clar type π bonds for B_{28}^{2-} at the PBE0/6-31G level using AdNDP. (d) The Clar type π bonds for $C_{20}H_{10}$ at the PBE0/6-31G* level using AdNDP. The occupation numbers (ONs) are shown. Reproduced from ref. 39 with permission from AIP Publishing, copyright 2016.
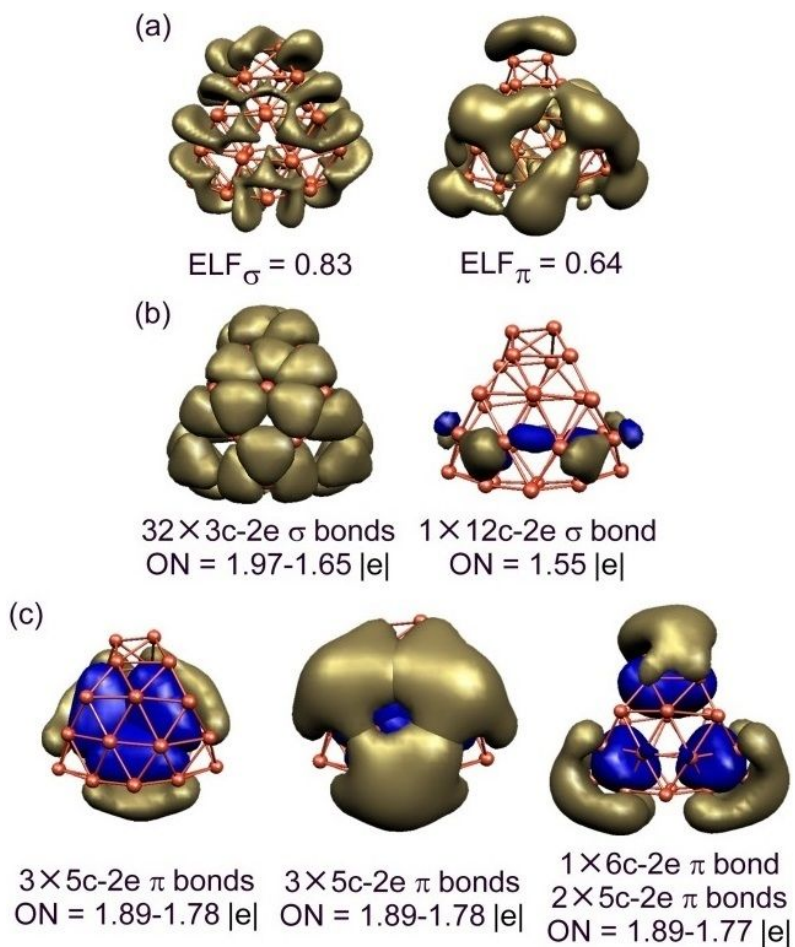
Fig. 11. Chemical bonding analyses for the seashell-like B_{28} borospherene. (a) The ELFσ and ELFπ. (b) The σ bonding using AdNDP. (c) The π bonding using AdNDP. The occupation numbers (ONs) are shown. Reproduced from ref. 39 with permission from AIP Publishing, copyright 2016.
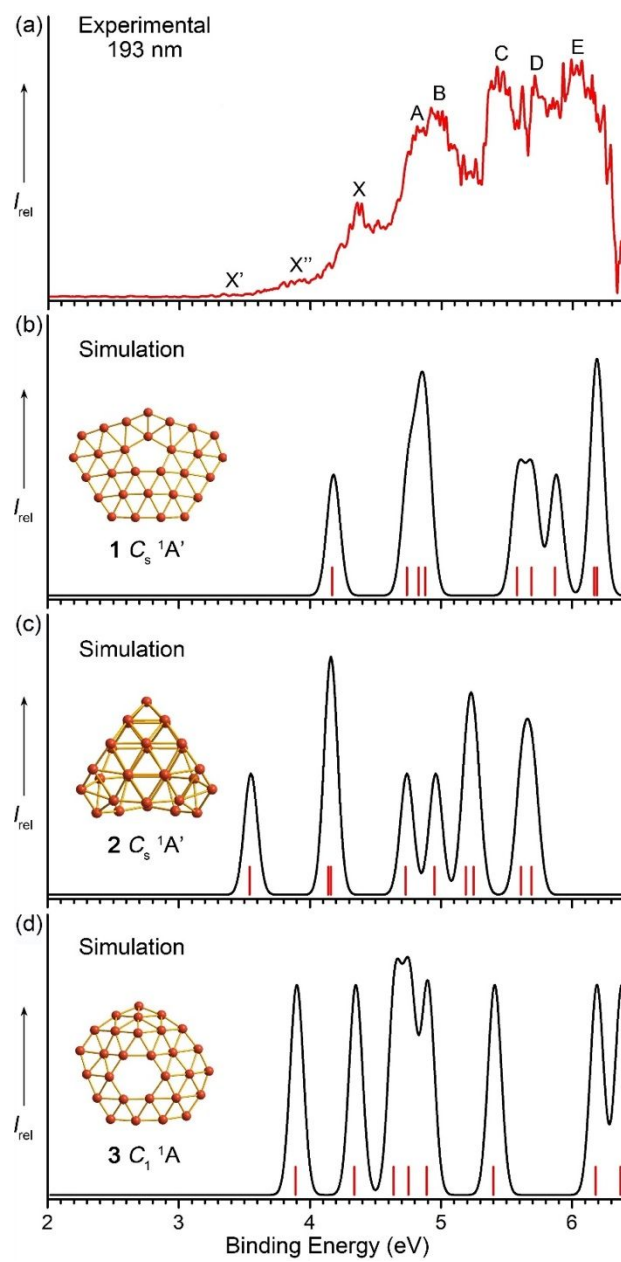
Fig. 12. Photoelectron spectrum of B_{29}^- at 193 nm (a) and comparison with simulated spectra of isomers **1** (b), **2** (c), and **3** (d) at the PBE0/6-311+G* level. Reproduced from ref. 40 with permission from the Royal Society of Chemistry, copyright 2016.
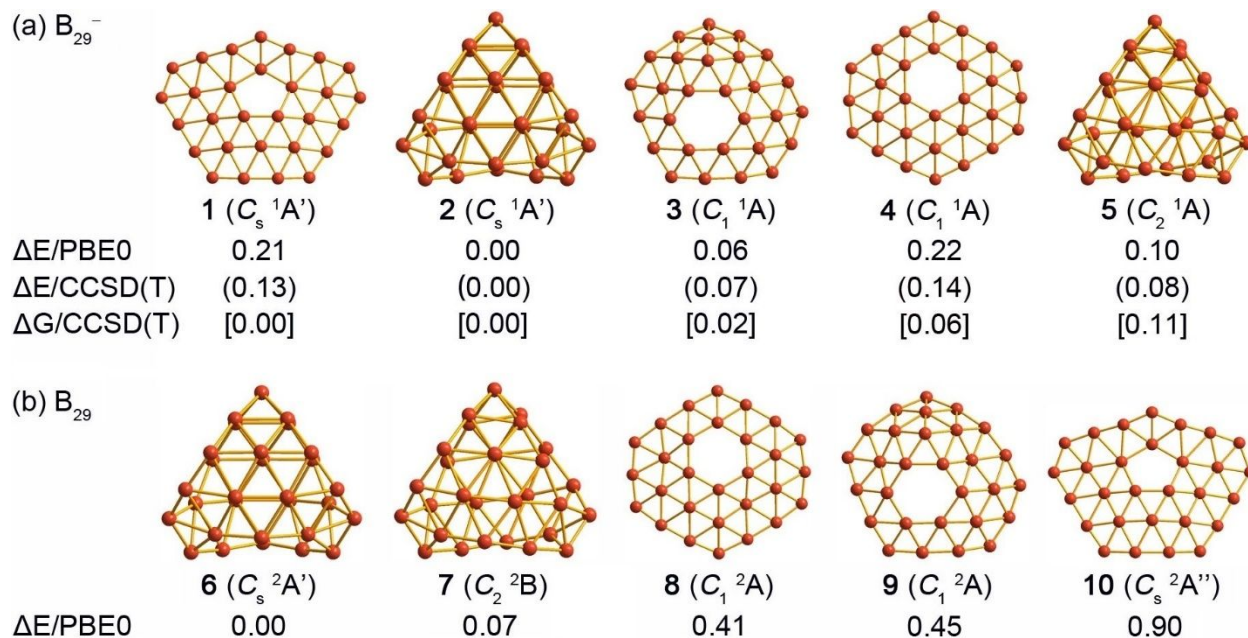
Fig. 13. The top five lowest-lying structures (**1–5**) for B_{29}^- at the PBE0/6-311+G* level, along with their relative energies (in eV) at three levels of theory: PBE0/6-311+G*, single-point CCSD(T) at the PBE0/6-311+G* geometries (in parentheses), and CCSD(T) with corrections for Gibbs free energies at 298 K (in square brackets). The PBE0 and CCSD(T) data were corrected for zero-point energies at PBE0. Gibbs free energies were calculated at the PBE0/6-311+G* level. The same set of low-lying isomers for neutral B_{29} (**6–10**) at the PBE0 level are also shown. Reproduced from ref. 40 with permission from the Royal Society of Chemistry, copyright 2016.
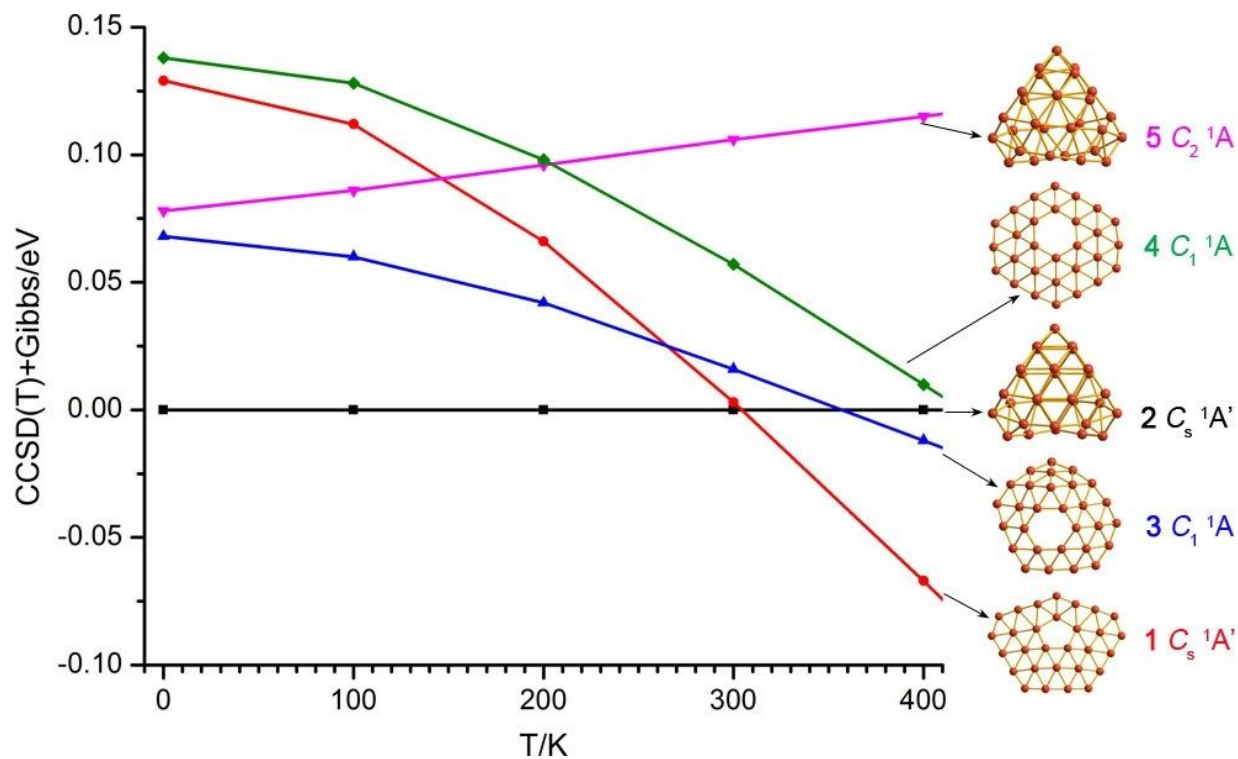
Fig. 14. Relative energies of the top five isomers (**1–5**) of B_{29}^- at the single-point CCSD(T) level, with Gibbs free energy corrections at PBE0/6-311+G* as a function of temperature from 0 to 400 K. The energies are plotted relative to that of the seashell-like C_s (**2**) structure. Reproduced from ref. 40 with permission from the Royal Society of Chemistry, copyright 2016.

(a)

| HOMO-1 (a_2) | HOMO-2 (a_2) | HOMO-3 (b_1) | HOMO-6 (b_1) | HOMO-10 (b_1) | HOMO-11 (a_2) | HOMO-17 (a_1) | HOMO-21 (b_2) | HOMO-24 (b_1) |

(b)

| HOMO (a_2) | HOMO-2 (a_2) | HOMO-1 (b_2) | HOMO-3 (b_2) | HOMO-5 (b_2) | HOMO-4 (a_2) | HOMO-10 (b_2) | HOMO-11 (a_2) | HOMO-17 (b_2) |
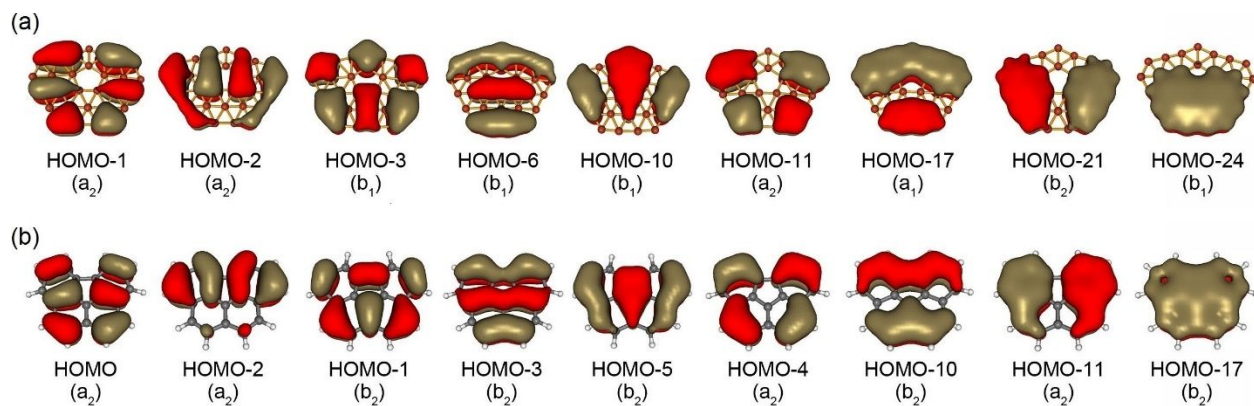
Fig. 15. Comparison of the π canonical molecular orbitals of (a) the flattened C_s (**1**) B_{29}^- cluster and (b) the benzo[*ghi*]fluoranthene ($C_{18}H_{10}$) PAH. Reproduced from ref. 40 with permission from the Royal Society of Chemistry, copyright 2016.

(a)

17 × 2c-2e σ bonds   5 × 3c-2e σ bonds   13 × 4c-2e σ bonds
ON = 1.76-1.93 |e| ON = 1.88-1.93 |e| ON = 1.87-1.95 |e|

4 × 4c-2e π bonds   2 × 5c-2e π bonds   1 × 5c-2e π bond   2 × 7c-2e π bonds
ON = 1.80-1.84 |e| ON = 1.75 |e| ON = 1.70 |e| ON = 1.67 |e|

(b)

10 × 2c-2e σ bonds   22 × 2c-2e σ bonds
ON = 1.98 |e| ON = 1.95-1.99 |e|

4 × 2c-2e π bonds   2 × 2c-2e π bonds   1 × 2c-2e π bond   2 × 2c-2e π bonds
ON = 1.74-1.80 |e| ON = 1.69 |e| ON = 1.60 |e| ON = 1.59 |e|
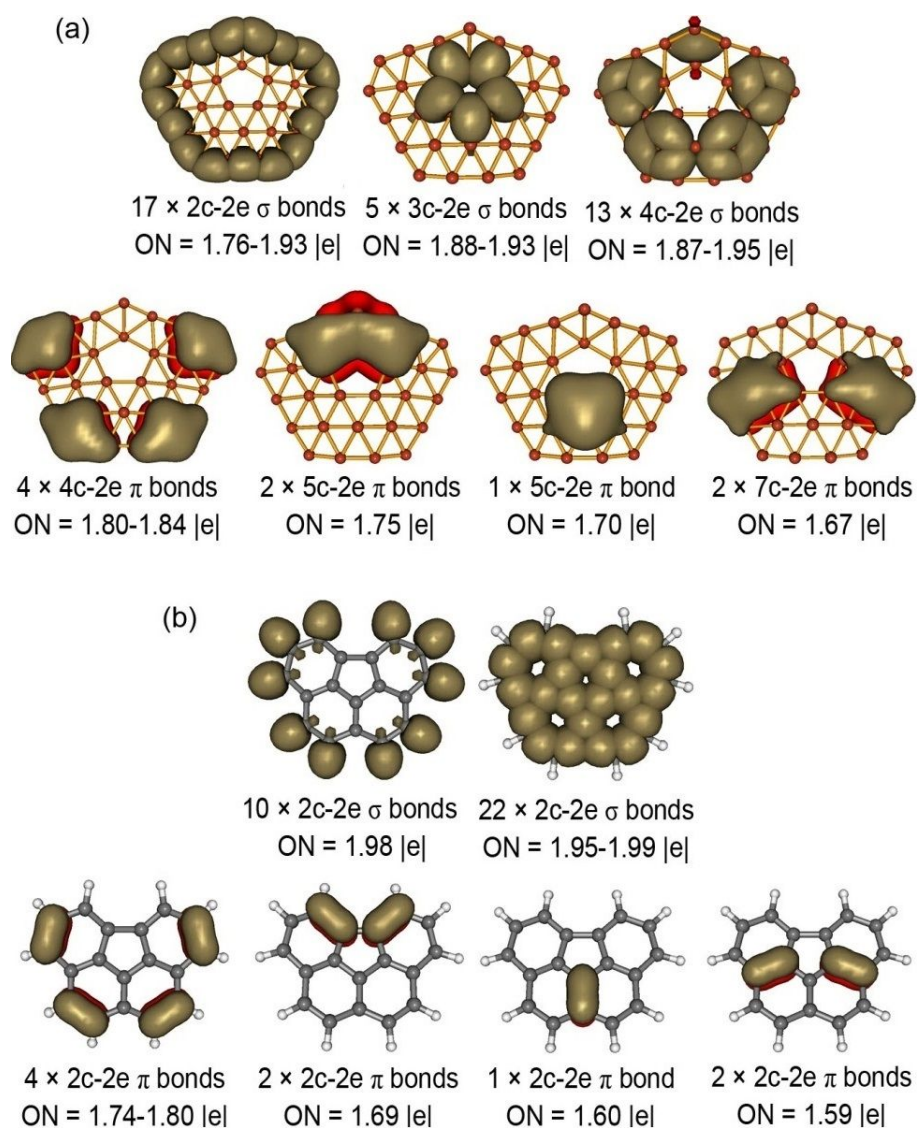
Fig. 16. AdNDP bonding analyses for (a) the C_s (**1**) isomer of B_{29}^- and (b) the $C_{18}H_{10}$ PAH at the PBE0/6-31G level. Occupation numbers (ONs) are shown. Reproduced from ref. 40 with permission from the Royal Society of Chemistry, copyright 2016.
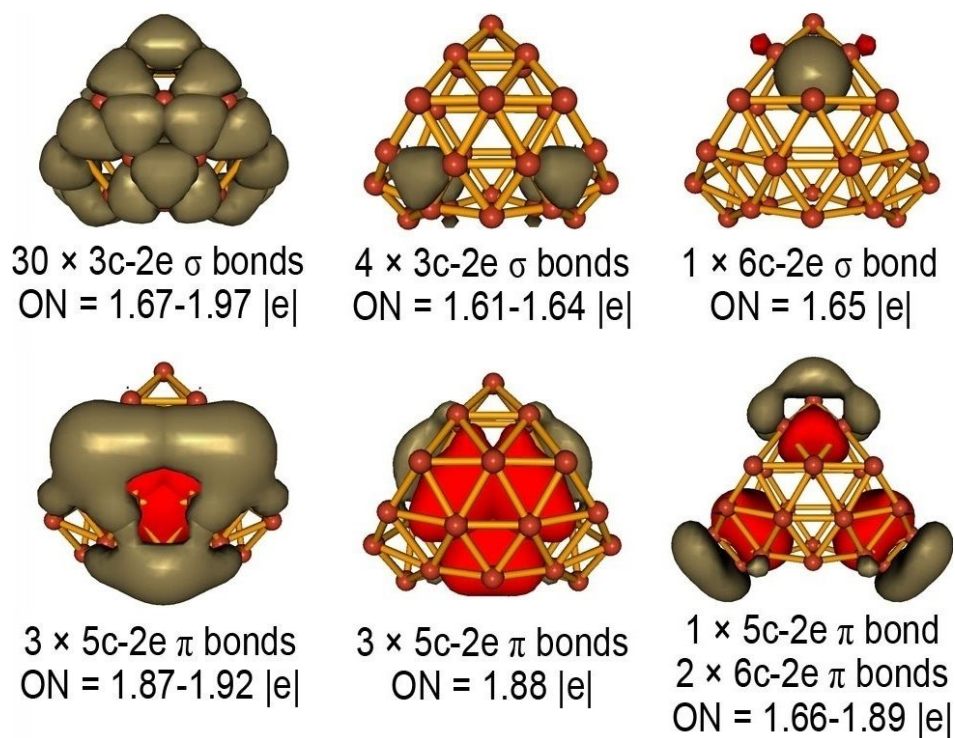
Fig. 17. AdNDP bonding analyses for the seashell-like C_s (**2**) isomer of B_{29}^-. Occupation numbers (ONs) are shown. Reproduced from ref. 40 with permission from the Royal Society of Chemistry, copyright 2016.
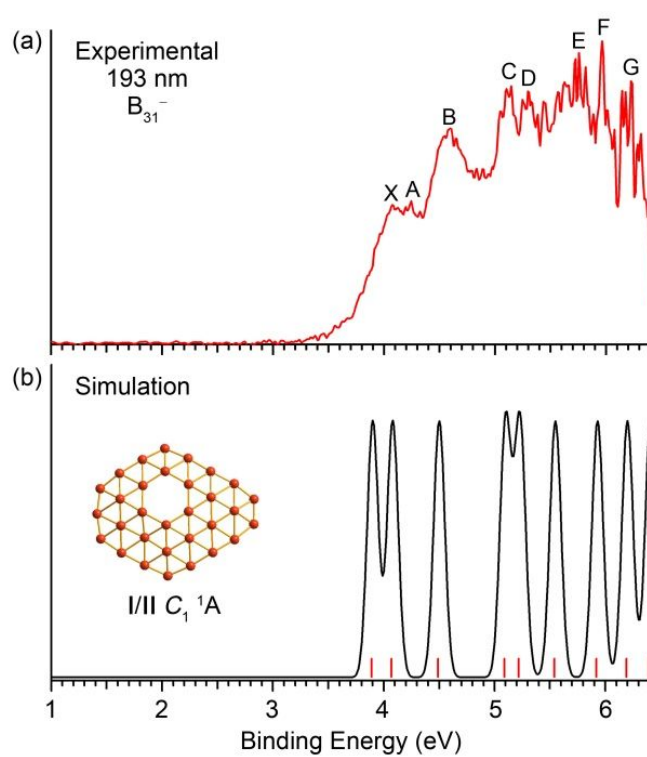
Fig. 18. Photoelectron spectrum of B_{31}^- at 193 nm (a) compared with simulated spectra of the lowest-lying chiral isomers of B_{31}^- (I and II) at the TD-PBE0/6-311+G(d) level. Reproduced from ref. 141 with permission from the Royal Society of Chemistry, copyright 2019.
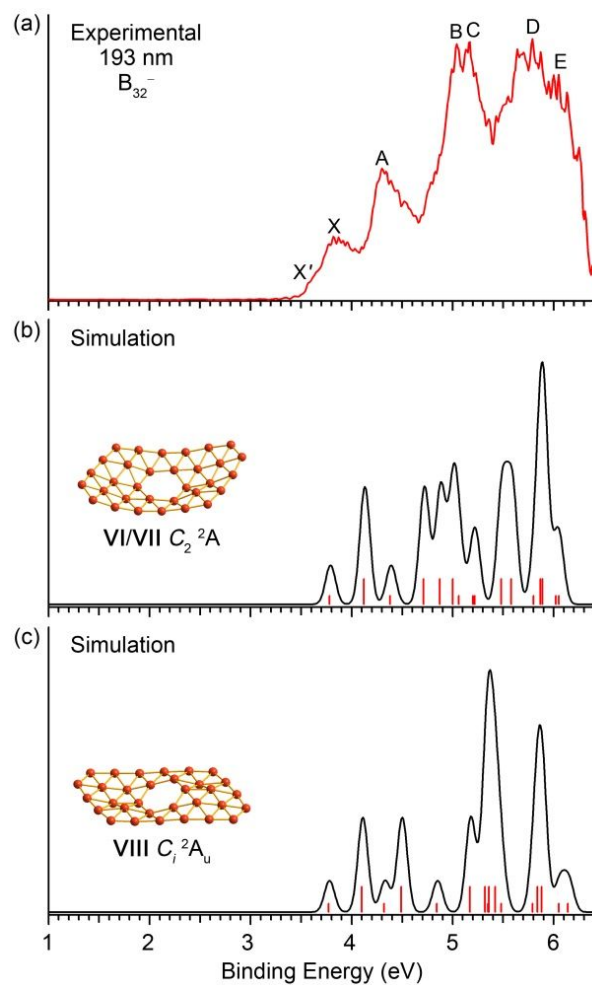
Fig. 19. Photoelectron spectrum of B_{32}^- at 193 nm (a) compared with the simulated spectra of the chiral global minima of B_{32}^- (VI and VII) and a low-lying isomer (C_i, VIII) at the TD-PBE0/6-311+G(d) level. Reproduced from ref. 141 with permission from the Royal Society of Chemistry, copyright 2019.
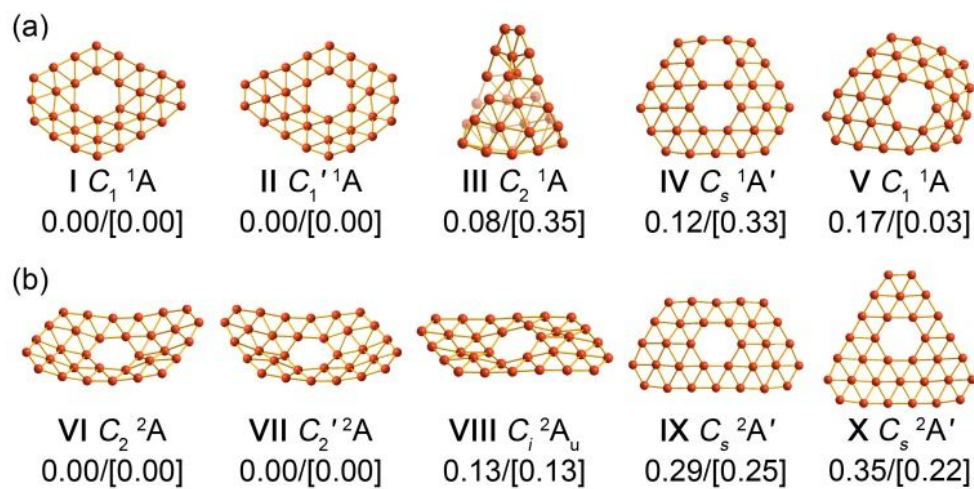
Fig. 20. The top five lowest-lying isomers of B_{31}^- (a) and B_{32}^- (b). The relative energies are given in eV at the CCSD(T)//PBE0 and PBE0/6-311+G(d) (in square brackets) levels of theory. Single-point calculations for the top five lowest-lying isomers of B_{31}^- and B_{32}^- were carried out using the CCSD(T)/6-311G(d) and UCCSD(T)/6-31G(d), respectively. Reproduced from ref. 141 with permission from the Royal Society of Chemistry, copyright 2019.
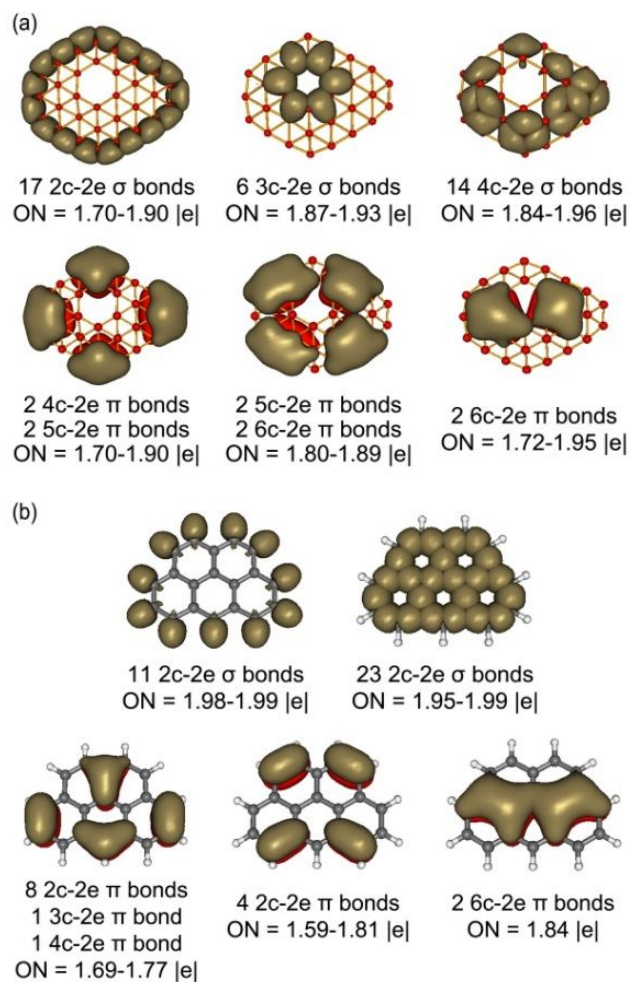
Fig. 21. Comparison of the AdNDP analyses for the global minimum of B_{31}^- (a) and the PAH $C_{19}H_{11}^-$ (b). ON = occupation number. Reproduced from ref. 141 with permission from the Royal Society of Chemistry, copyright 2019.
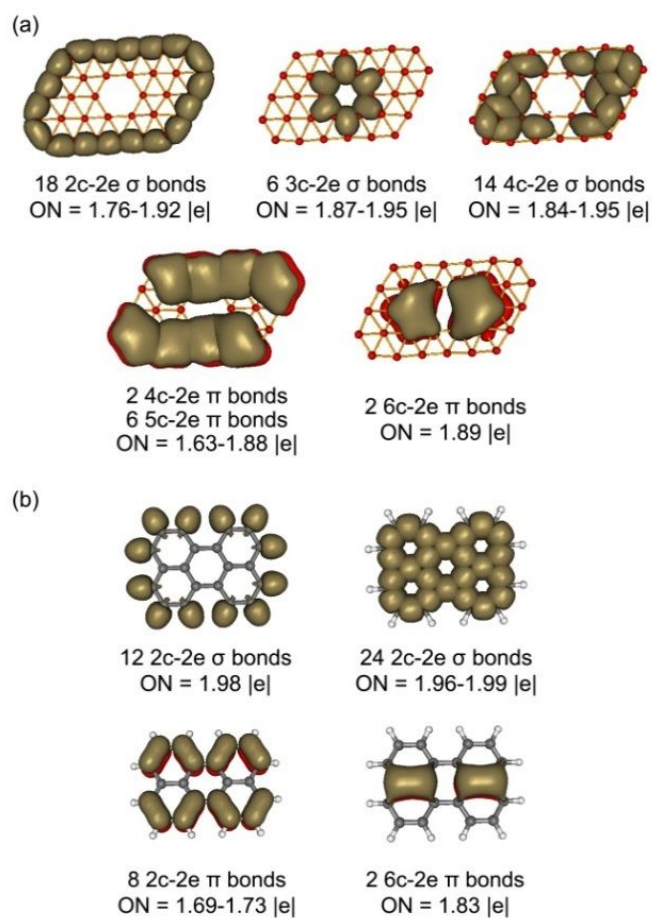
Fig. 22. Comparison of the AdNDP analyses for the closed-shell C_2 B_{32} (a) and the PAH $C_{20}H_{12}$ (b). ON = occupation number. Reproduced from ref. 141 with permission from the Royal Society of Chemistry, copyright 2019.
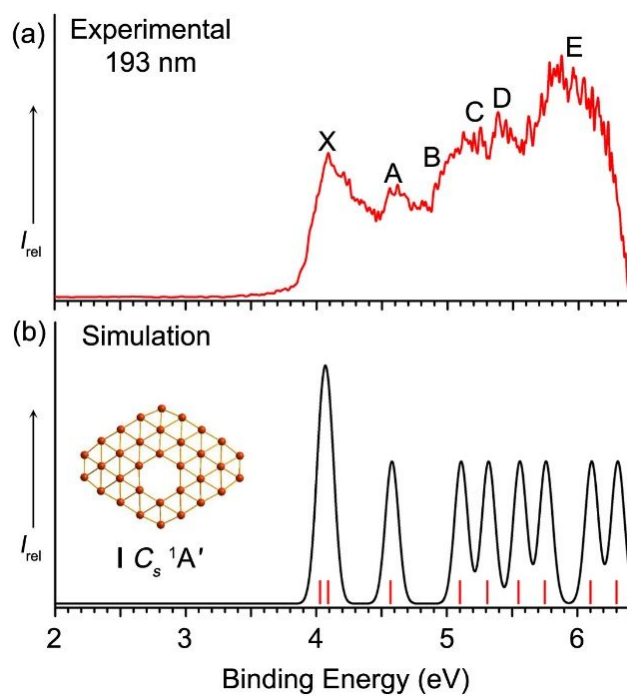
Fig. 23. Photoelectron spectrum of (a) B_{33}^- at 193 nm, compared to (b) the simulated spectrum of the global minimum of B_{33}^- (**I**, C_s) at the TD-PBE0/6-311+G(d) level. Reproduced from ref. 44 with permission from Wiley-VCH, copyright 2017.
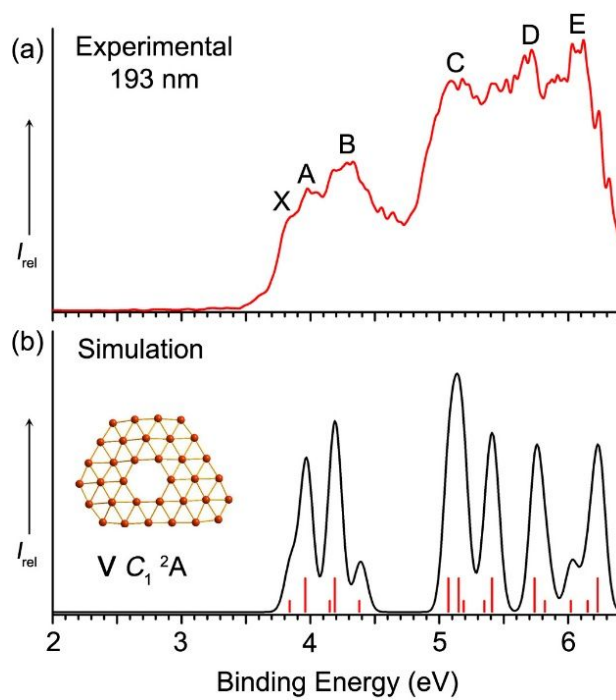
Fig. 24. Photoelectron spectrum of (a) B_{34}^- at 193 nm, compared to (b) the simulated spectrum of the global minimum of B_{34}^- at the TD-PBE0/6-311+G(d) level. Reproduced from ref. 44 with permission from Wiley-VCH, copyright 2017.
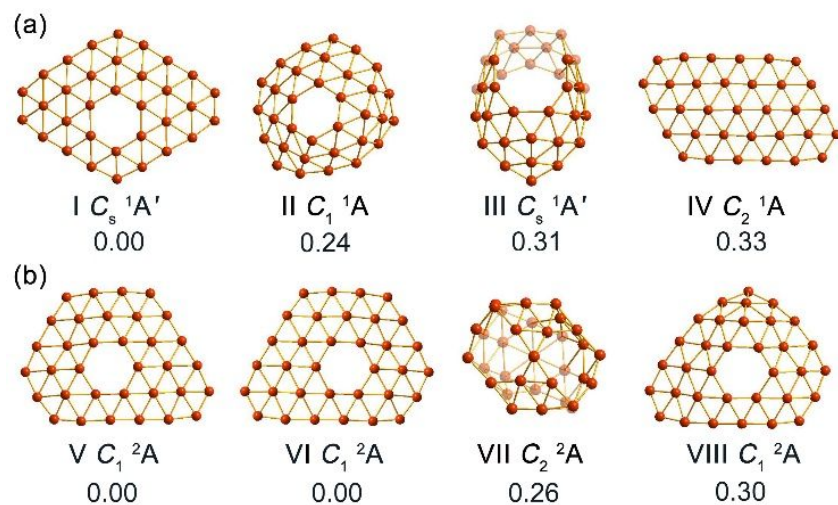
Fig. 25. The global minimum and low-lying isomers of (a) B_{33}^- and (b) B_{34}^-. Relative energies at the PBE0/6-311+G(d) level (including ZPE corrections) are shown in eV. Note the global minimum of B_{34}^- (**V** and **VI**) are enantiomers. Reproduced from ref. 44 with permission from Wiley-VCH, copyright 2017.
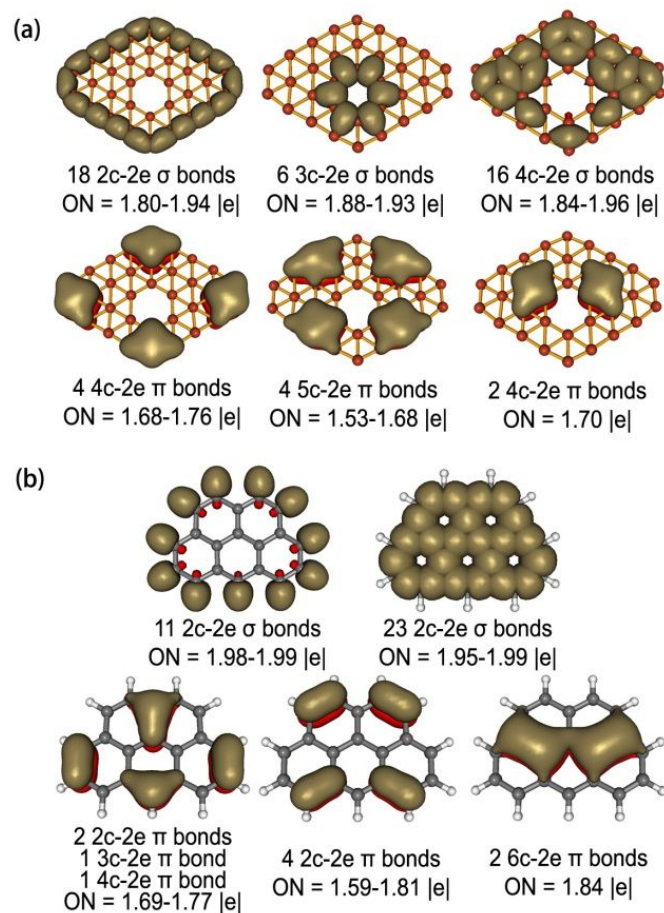
Fig. 26. AdNDP analyses for (a) the global minimum of B_{33}^- and (b) C_{2v} $C_{19}H_{11}^-$. Reproduced from ref. 44 with permission from Wiley-VCH, copyright 2017.

18 2c-2e σ bonds
ON = 1.61-1.94 |e|

6 3c-2e σ bonds
ON = 1.91-1.95 |e|

16 4c-2e σ bonds
ON = 1.89-1.96 |e|

9 5c-2e π bonds
ON = 1.80-1.93 |e|

3 5c-2e π bonds
ON = 1.83-1.88 |e|
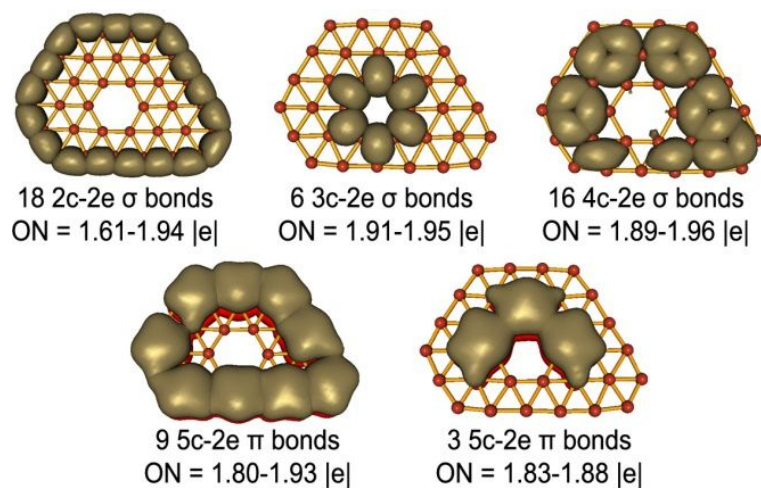
Fig. 27. AdNDP analyses for the closed-shell B_{34}^{2-} corresponding to the global minimum of B_{34}^{-}. Reproduced from ref. 44 with permission from Wiley-VCH, copyright 2017.
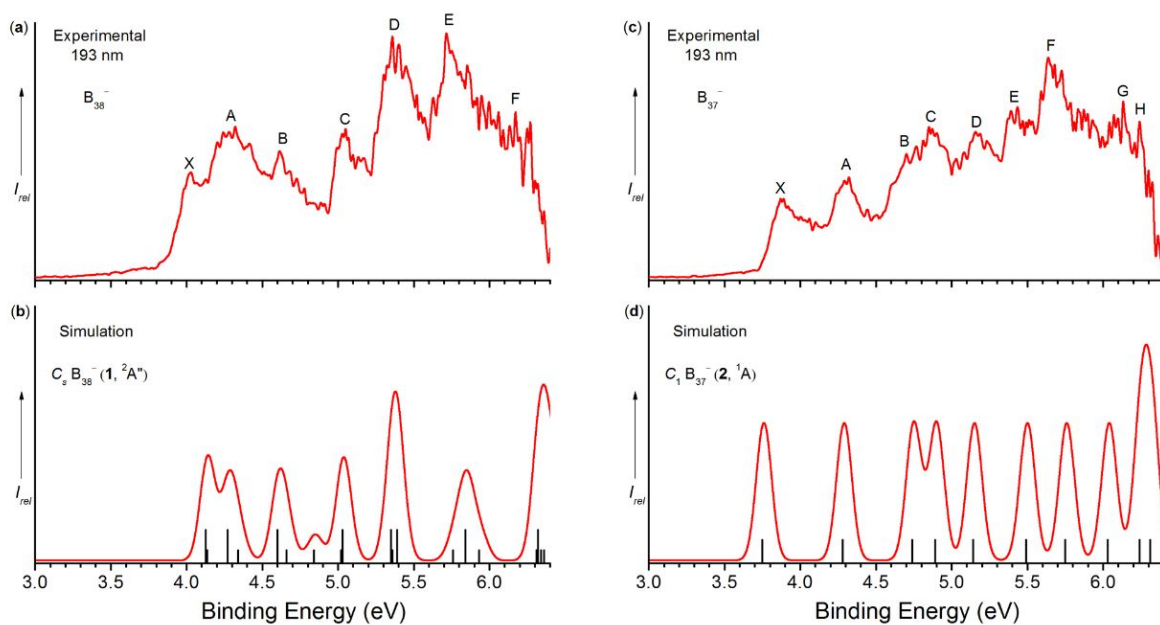
Fig. 28. Photoelectron spectra of (a) B_{38}^- and (c) B_{37}^- at 193 nm, compared with the simulated spectra of (b) C_s B_{38}^- (**1**, $^2A''$) and (d) C_1 B_{37}^- (**2**, ^1A) at the TD-PBE0/6-311+G* level. Reproduced from ref. 41 with permission from the Royal Society of Chemistry, copyright 2017.
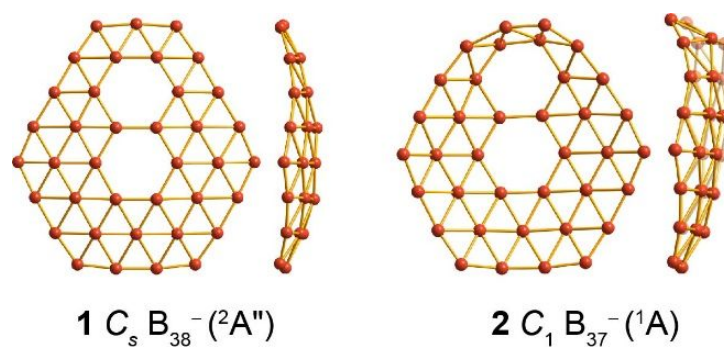
Fig. 29. Top and side views of the global-minimum structures of B_{38}^- and B_{37}^- at the PBE0/6-311+G* level. Reproduced from ref. 41 with permission from the Royal Society of Chemistry, copyright 2017.

Fig. 30. Configurational energy spectra of (a) B_{38}^- and (b) B_{37}^- at the PBE0/6-311+G* level. Black, red, violet, and blue horizontal bars represent quasi-planar, cage-like, double-, and triple-ring tubular structures, respectively. Relative energies are given in eV. Reproduced from ref. 41 with permission from the Royal Society of Chemistry, copyright 2017.
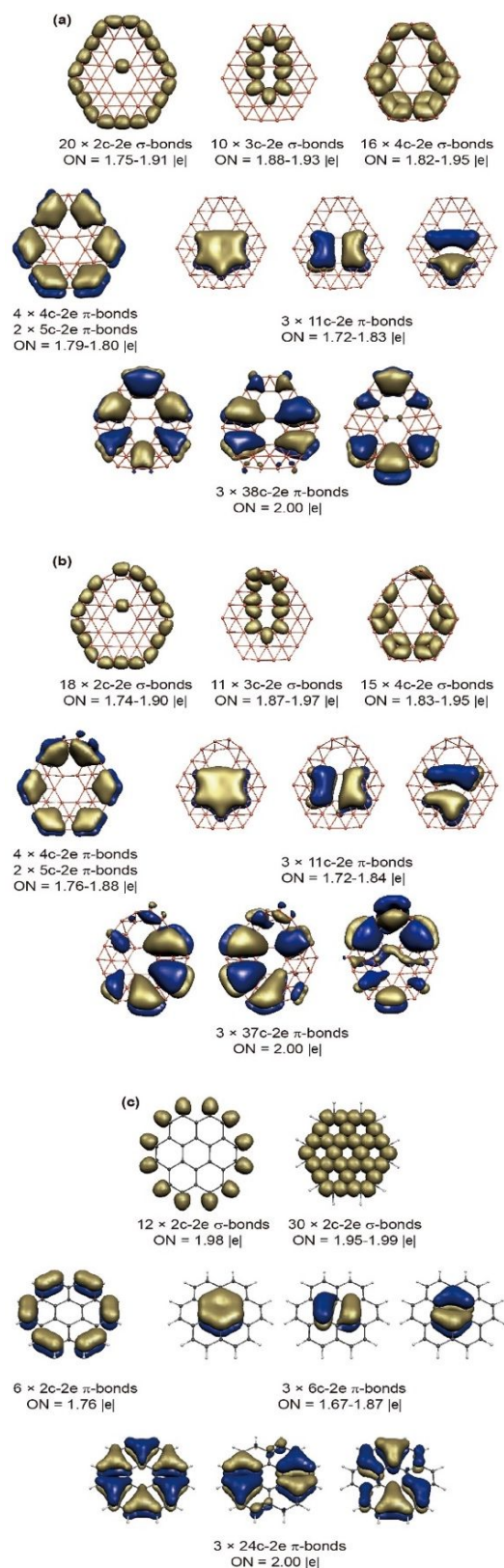
Fig. 31. AdNDP analyses of (a) C_s B_{38}^{2-}, (b) C_1 B_{37}^{-}, and (c) coronene. Occupation numbers (ONs) are indicated. Reproduced from ref. 41 with permission from the Royal Society of Chemistry, copyright 2017.
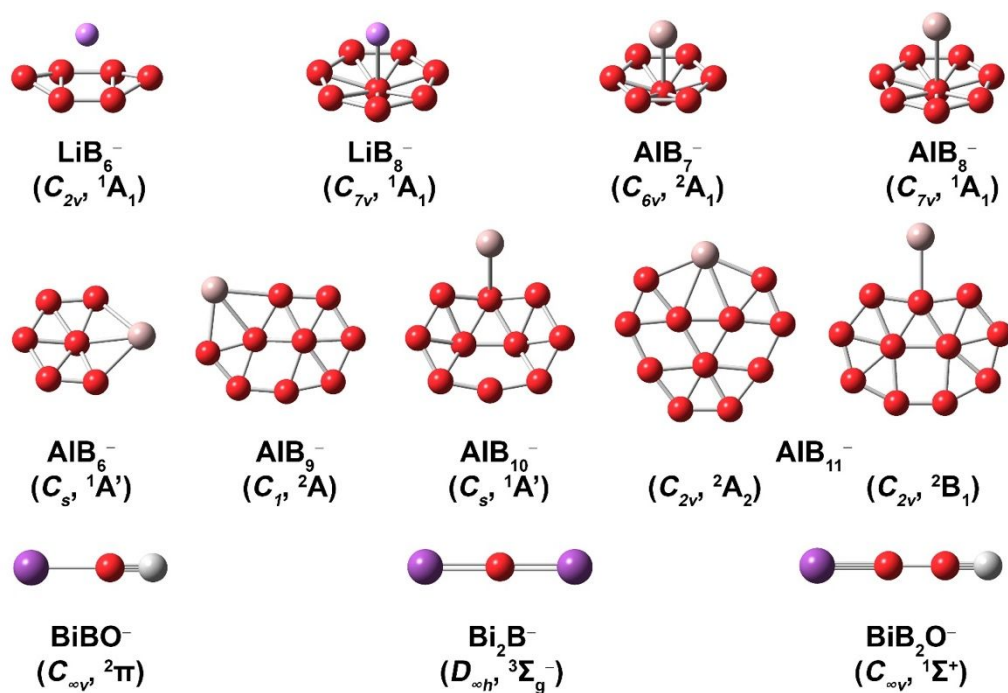
Fig. 32. A summary of the global minima of mono-main-group metal doped boron clusters confirmed from joint photoelectron spectroscopy and theoretical calculations.
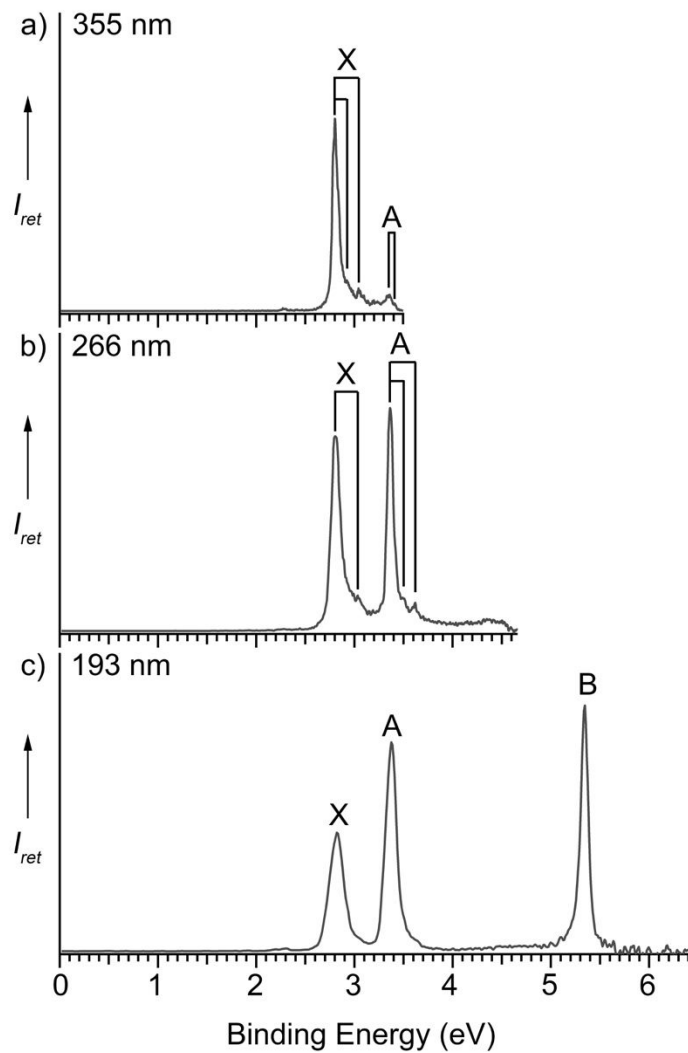
Fig. 33. Photoelectron spectra of BiB$_2$O$^-$ at (a) 355 nm, (b) 266 nm, and (c) 193 nm. The resolved vibrational structures are labeled for bands X and A in (a) and (b). Reproduced from ref. 73 with permission from Wiley-VCH, copyright 2017.
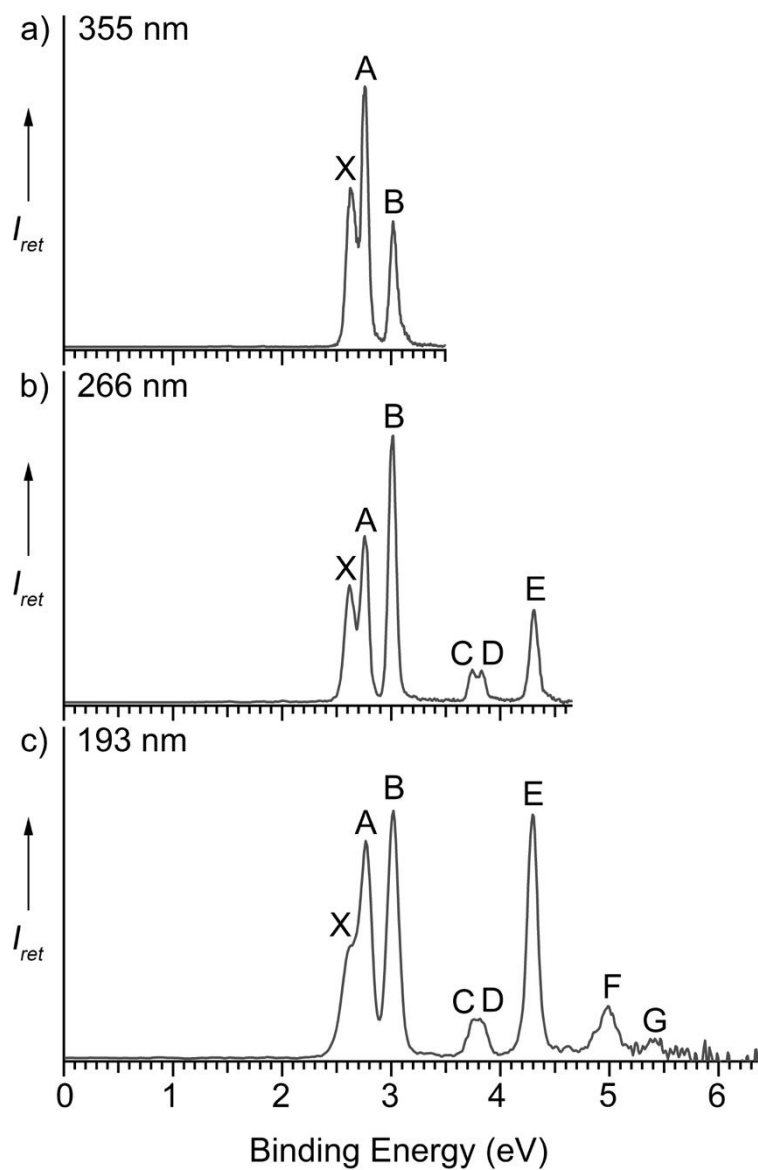
Fig. 34. Photoelectron spectra of Bi_2B^- at (a) 355 nm, (b) 266 nm, and (c) 193 nm. Reproduced from ref. 73 with permission from Wiley-VCH, copyright 2017.
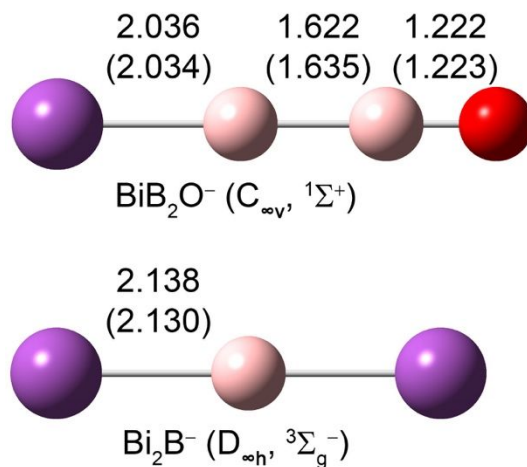
Fig. 35. The optimized structures of BiB$_2$O$^-$ and Bi$_2$B$^-$ at the PBE0/AVTZ and CCSD/AVTZ levels of theory. Bond lengths are given in Å and the values in parentheses are from the CCSD/AVTZ level. Redrawn from ref. 73 with permission from Wiley-VCH, copyright 2017.
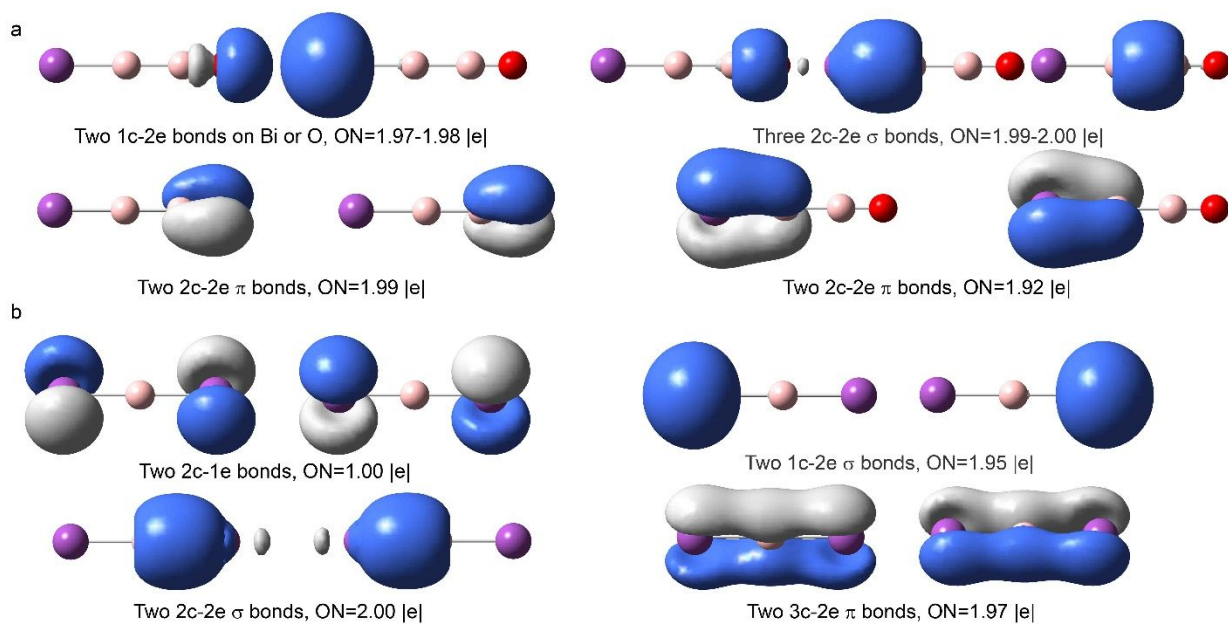
Fig. 36. Chemical bonding analyses using AdNDP for (a) BiB_2O^- and (b) Bi_2B^- at the PBE0/AVTZ level. Redrawn from ref. 73 with permission from Wiley-VCH, copyright 2017.
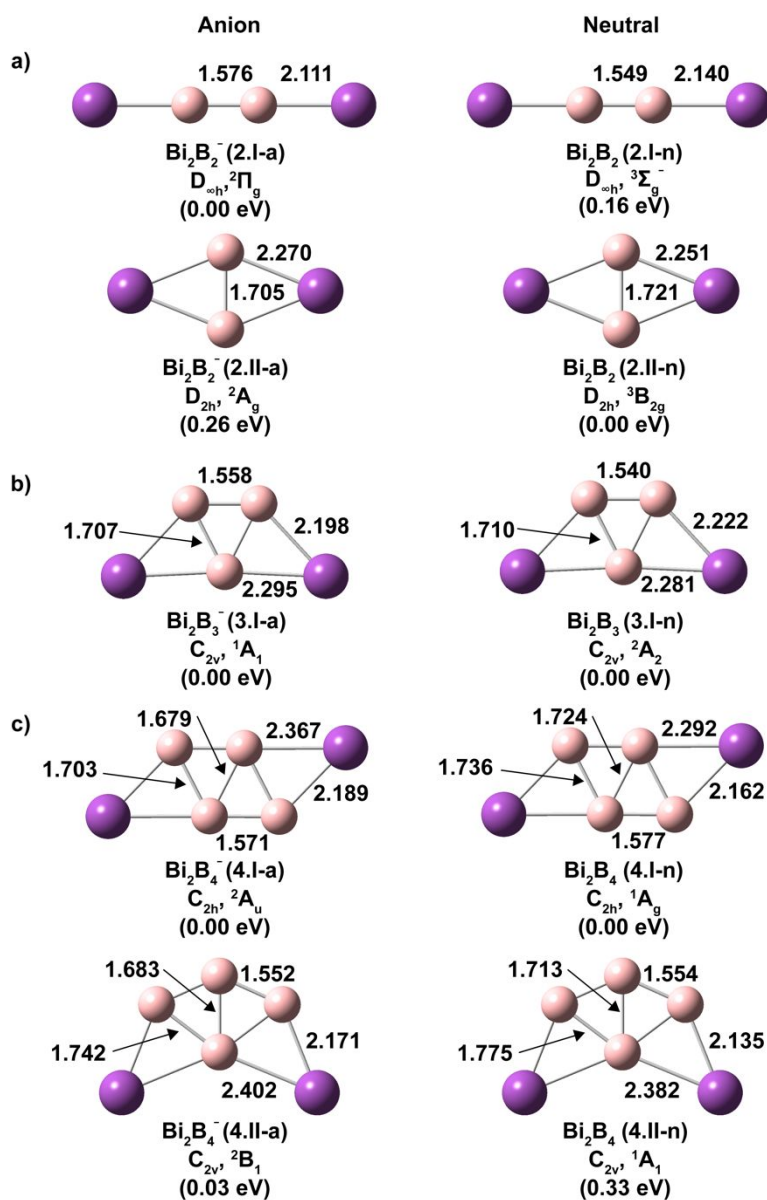
Fig. 37. The global minima and low-lying structures of (a) $Bi_2B_2^-$, (b) $Bi_2B_3^-$, (c) $Bi_2B_4^-$, and their corresponding neutrals optimized at the TPSSh/Bi/aug-cc-pVTZ-pp/B/aug-cc-pVTZ level of theory. Bond lengths are given in Å. Reproduced from ref. 153 with permission from AIP Publishing, copyright 2019.
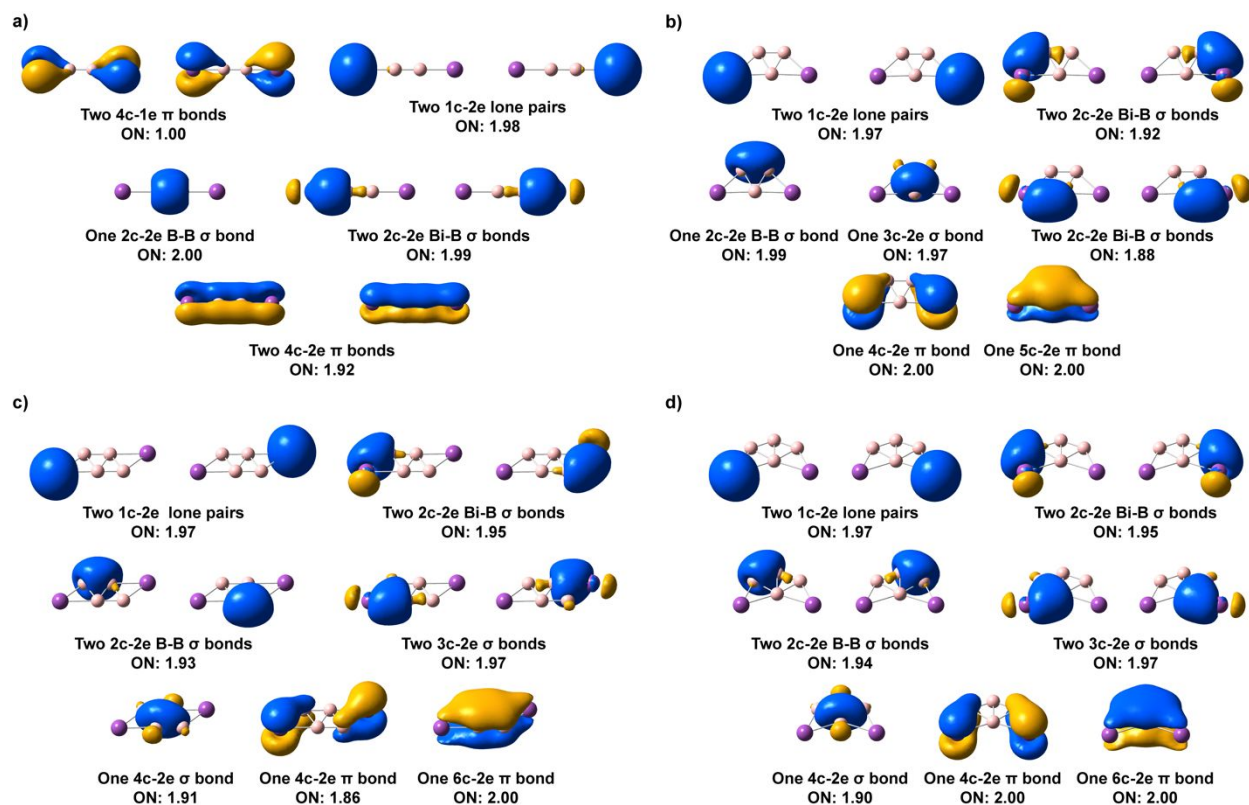
Fig. 38. AdNDP analyses of (a) Bi_2B_2 (2.I-n), (b) $Bi_2B_3^-$ (3.I-a), (c) Bi_2B_4 (4.I-n), and (d) Bi_2B_4 (4.II-n) (Fig. 37). Reproduced from ref. 153 with permission from AIP Publishing, copyright 2019.
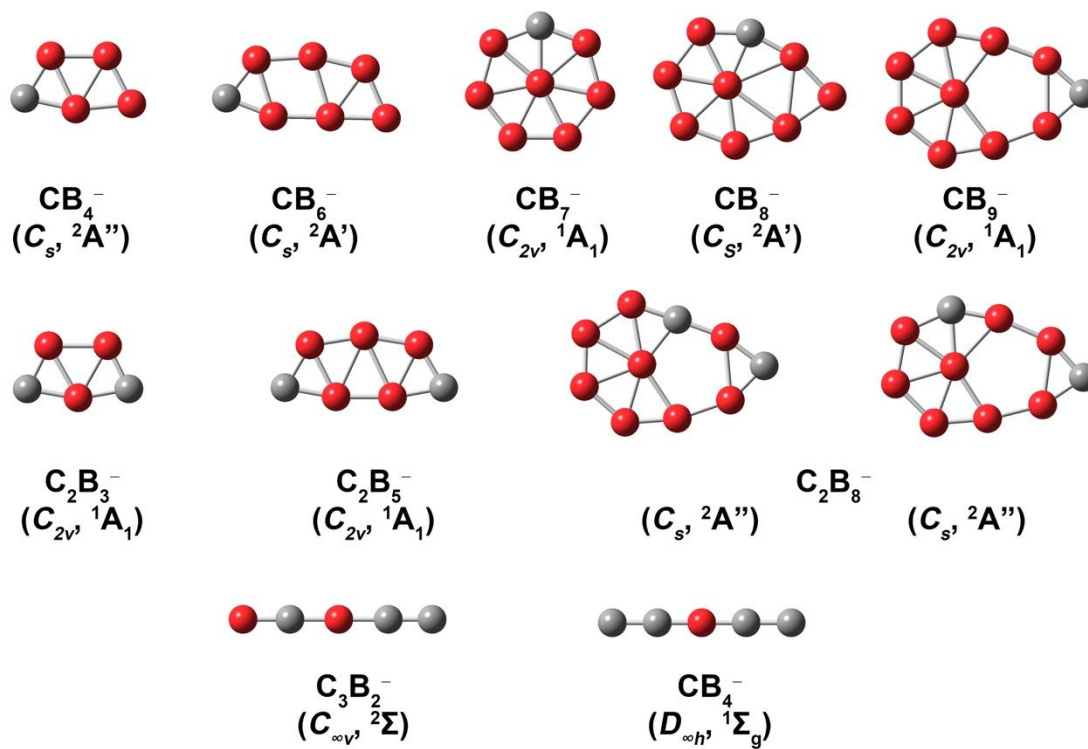
Fig. 39. A summary of the global minima of carbon doped boron clusters confirmed from joint photoelectron spectroscopy and theoretical calculations.
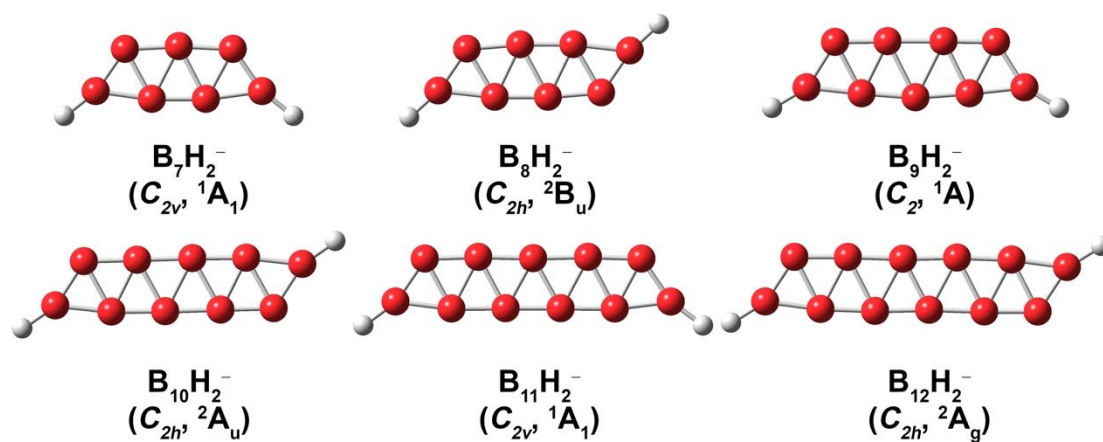
Fig. 40. A summary of the global minima of dihydrogenated boron clusters confirmed from joint photoelectron spectroscopy and theoretical calculations. Reproduced from ref. 121a with permission from the American Chemical Society, copyright 2012.
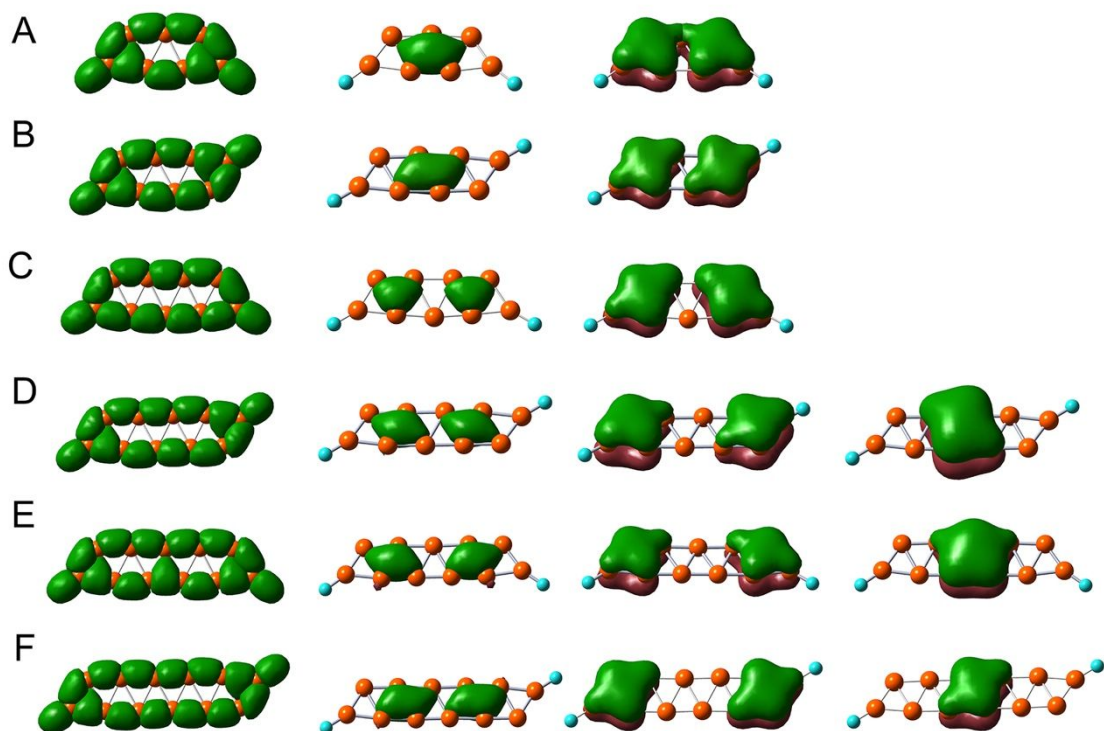
Fig. 41. AdNDP analyses for (A) $H_2B_7^-$, (B) H_2B_8, (C) $H_2B_9^-$, (D) $H_2B_{10}^{2-}$, (E) $H_2B_{11}^-$, (F) H_2B_{12}. Reproduced from ref. 121a with permission from the American Chemical Society, copyright 2012.
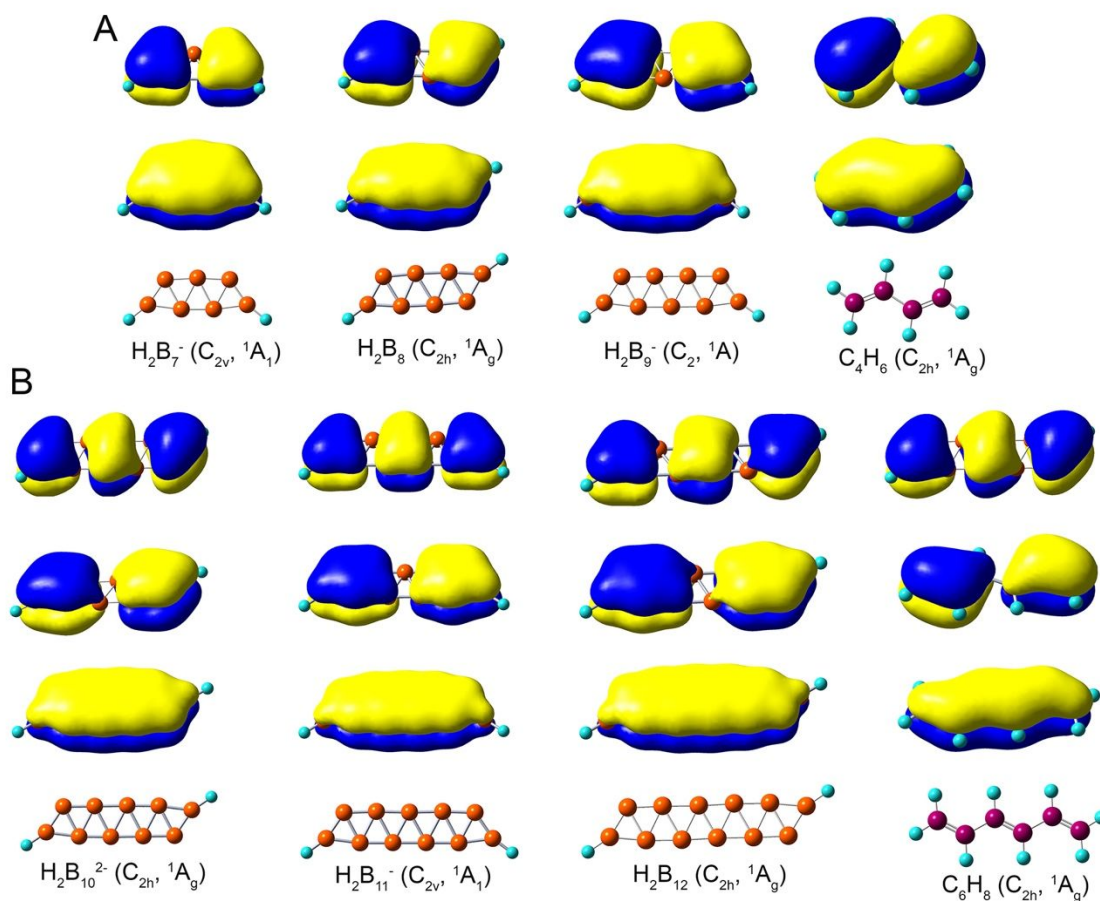
Fig. 42. Comparison of the π MOs of the boron cluster dihydrides with those of conjugated alkenes. (A) The π orbitals of $H_2B_7^-$, H_2B_8, $H2B_9^-$, and butadiene (C_4H_6). (B) The π orbitals of $H_2B_{10}^{2-}$, $H_2B_{11}^-$, H_2B_{12}, and 1,3,5-hexatriene (C_6H_8). Reproduced from ref. 121a with permission from the American Chemical Society, copyright 2012.
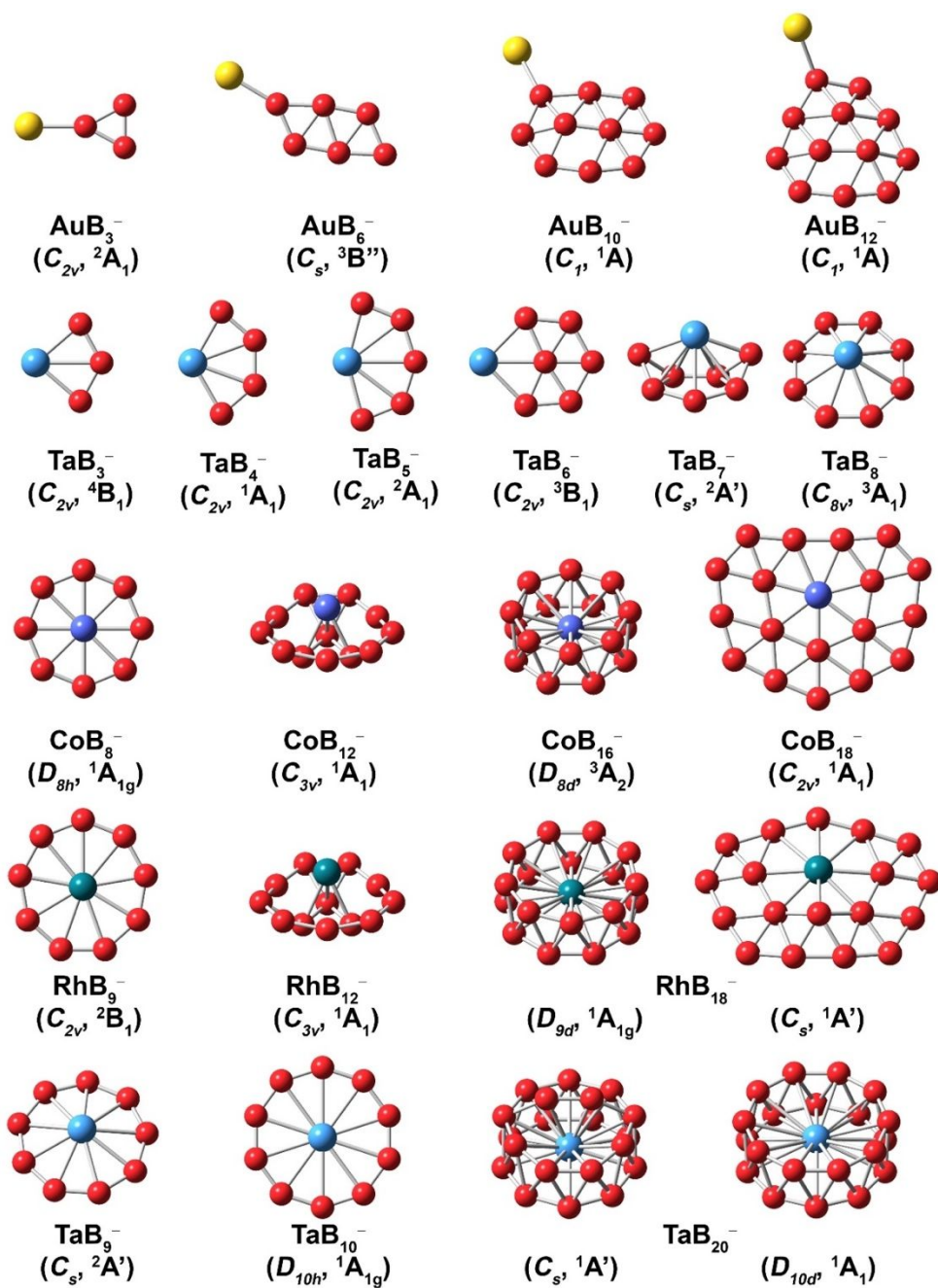
Fig. 43. A summary of the global minima of mono transition metal doped boron clusters confirmed from joint photoelectron spectroscopy and theoretical calculations. Note that Au has a filled 5d shell, while Co, Rh, and Ta are chosen as a representative for 3d, 4d, and 5d transition metals, respectively.
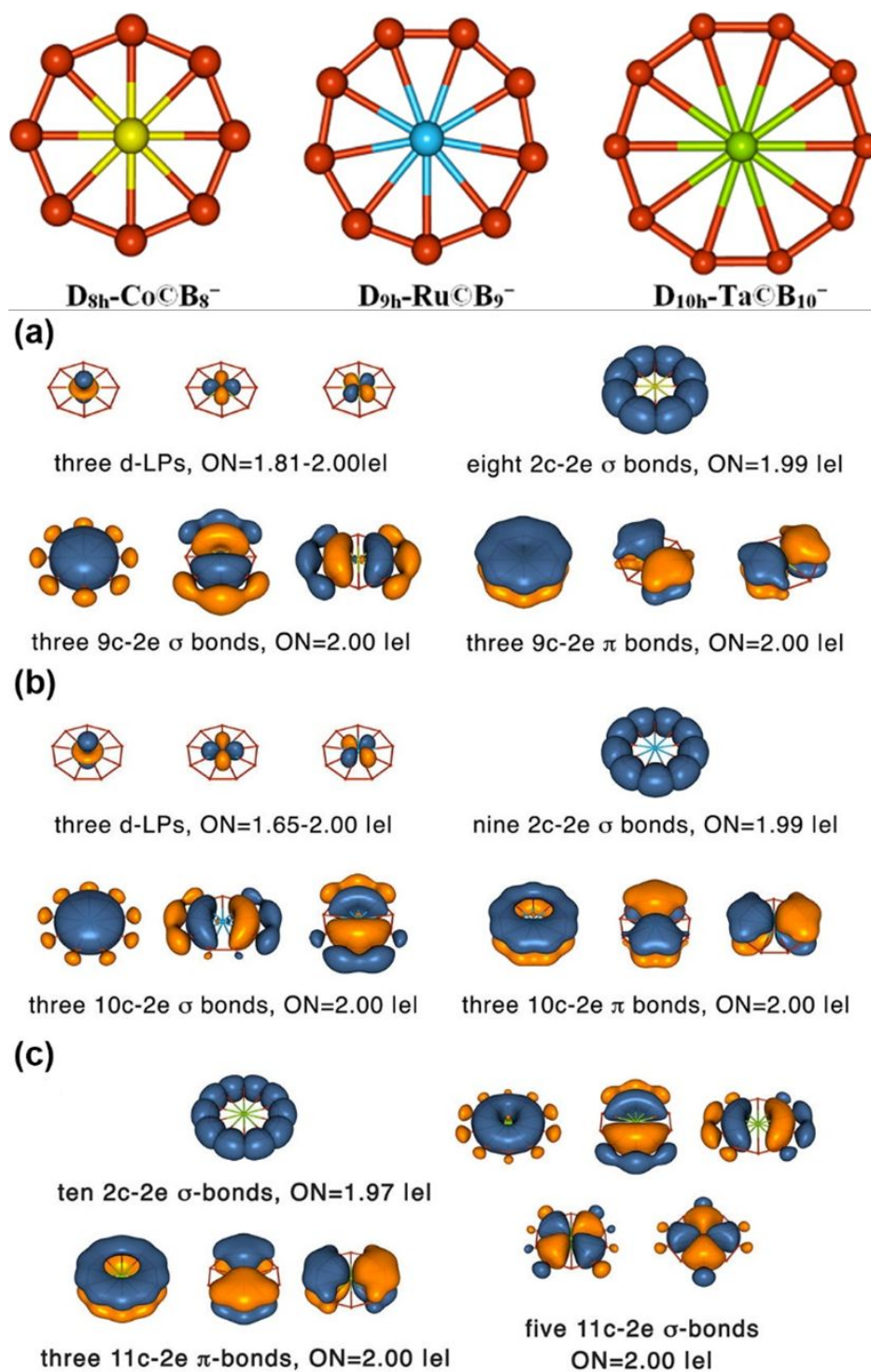
Fig. 44. AdNDP analyses for (a) CoB_8^-, (b) RuB_9^-, and (c) TaB_{10}^-. Redrawn from ref. 83 with permission from the American Chemical Society, copyright 2012.
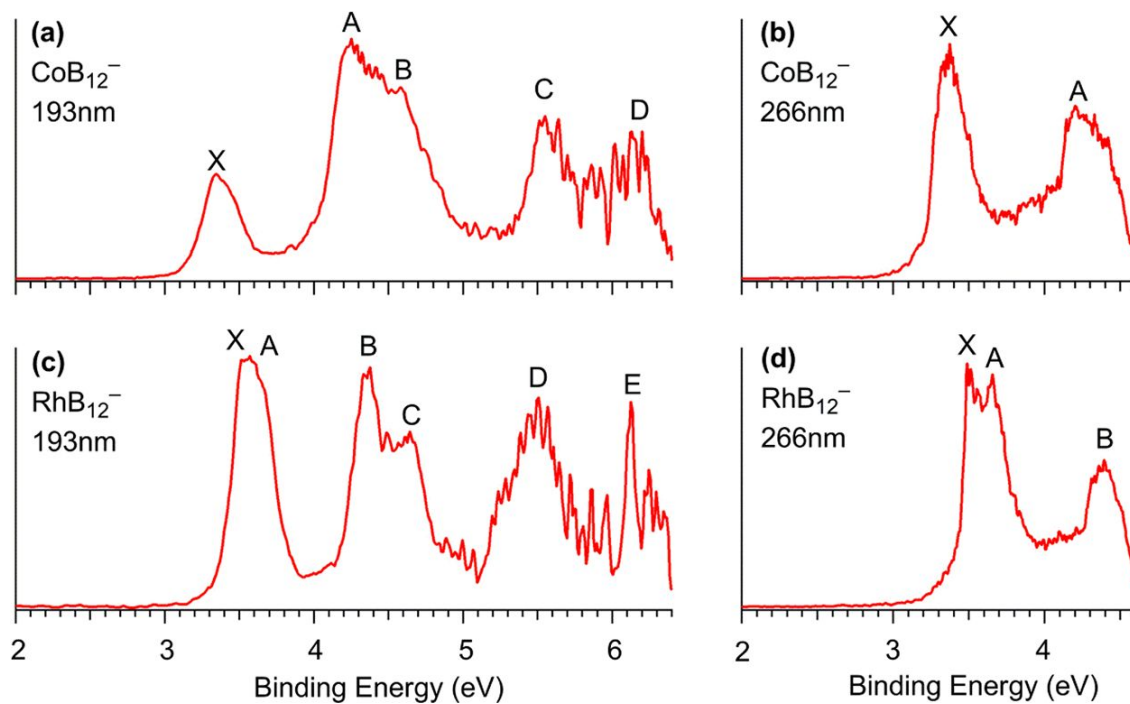
Fig. 45. Photoelectron spectra of CoB_{12}^- (a,b) and RhB_{12}^- (c,d) at 193 nm and 266 nm. Reproduced from ref. 88 with permission from the American Chemical Society, copyright 2014.
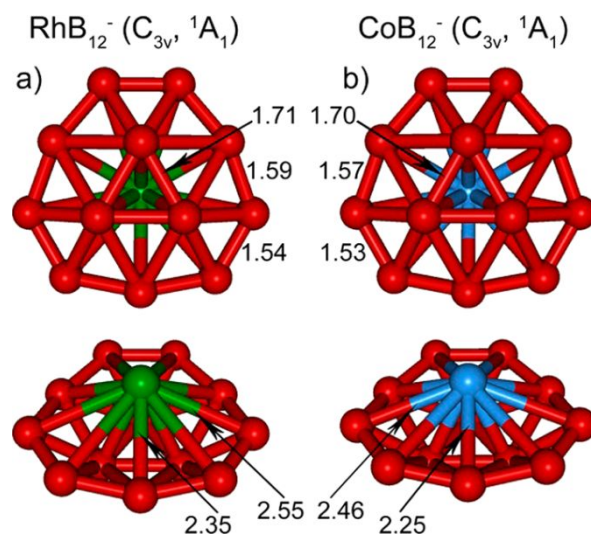
Fig. 46. Two views of the global minimum structures of (a) RhB_{12}^- and (b) CoB_{12}^-. Bond lengths are given in Å. Reproduced from ref. 88 with permission from the American Chemical Society, copyright 2014.
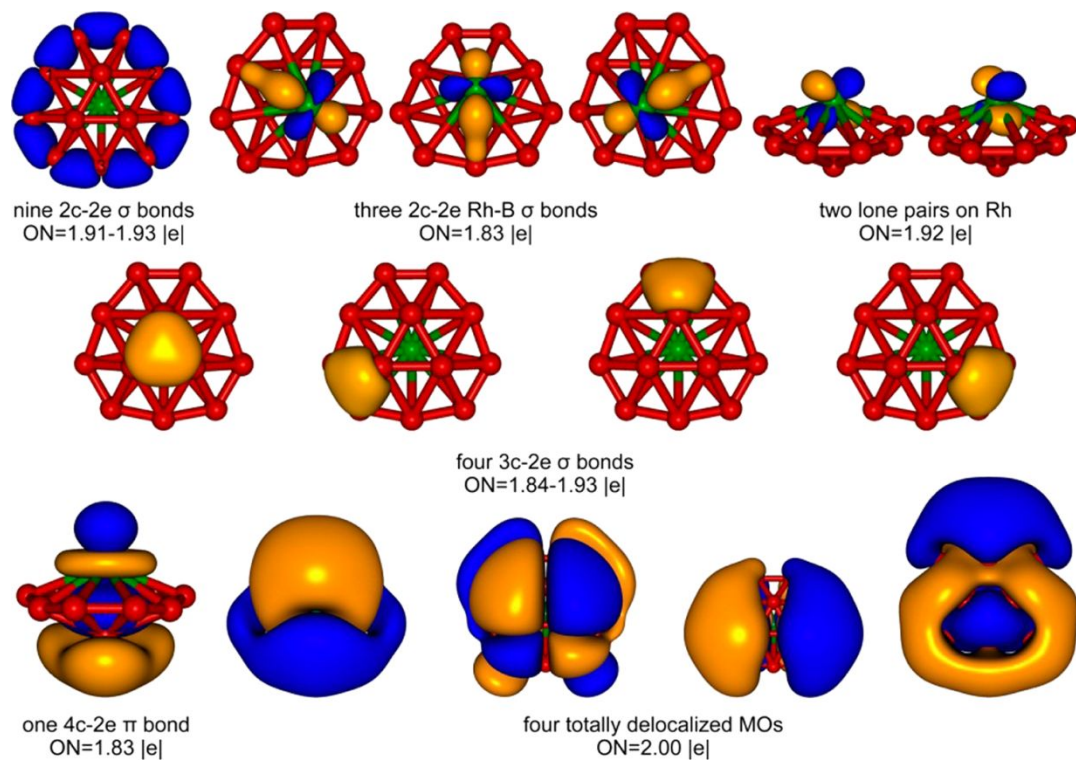
Fig. 47. AdNDP analyses for RhB_{12}^{-}. Reproduced from ref. 88 with permission from the American Chemical Society, copyright 2014.
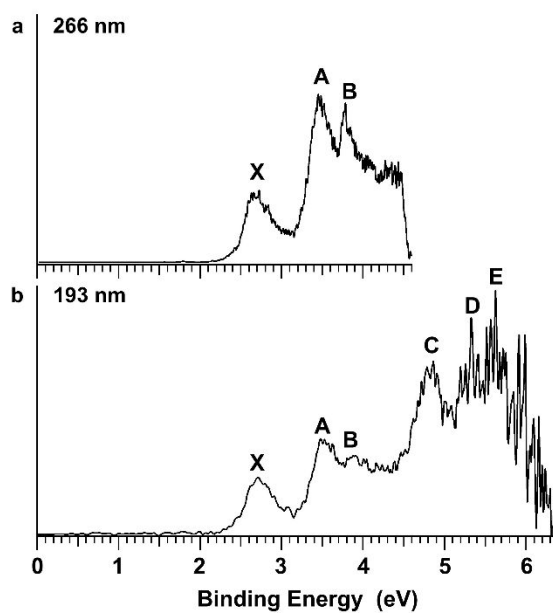
Fig. 48. Photoelectron spectra of CoB_{16}^- (a) at 266 nm and (b) at 193 nm. Reproduced from ref. 91 with permission from Macmillan Publishers Limited, copyright 2015.
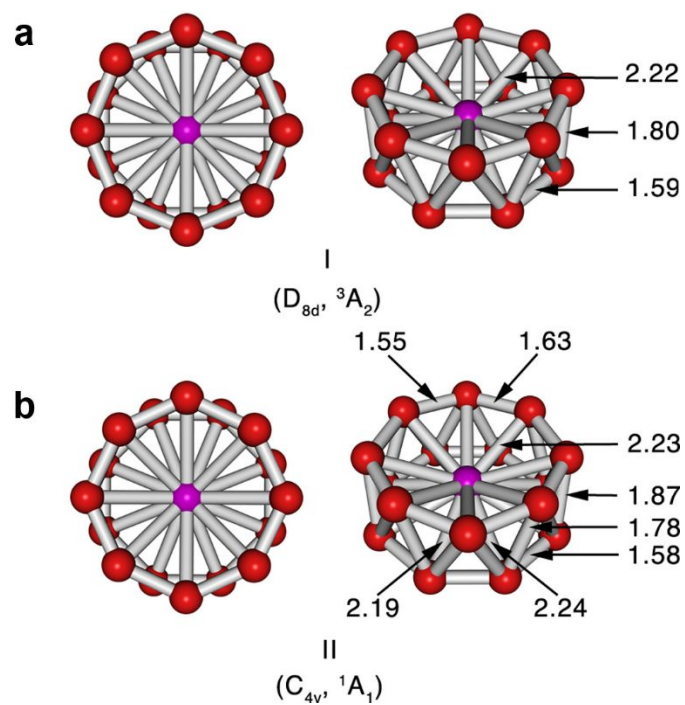
Fig. 49. Two views of isomer I (a) and isomer II (b) of the CoB_{16}^- cluster. All distances are in Å. Reproduced from ref. 91 with permission from Macmillan Publishers Limited, copyright 2015.

a

Sixteen 2c-2e B-B σ bonds
ON=1.84 |e|

b

3d$_{zz}$ lone pair on Co
ON=1.98 |e|

c **d** **e** **f** **g**

Three 16c-2e σ+σ bonds
ON=1.82-1.86 |e|

Two 17c-2e σ+σ bonds
ON=2.00 |e|

h **i** **j**

One 16c-2e σ-σ bond
ON=1.86 |e|

Two 17c-2e σ-σ bonds
ON=2.00 |e|

k **l** **m** **n** **o**

Three 16c-2e π-π bonds
ON=1.98-2.00 |e|

Two 16c-1e π-π bonds
ON=1.00 |e|
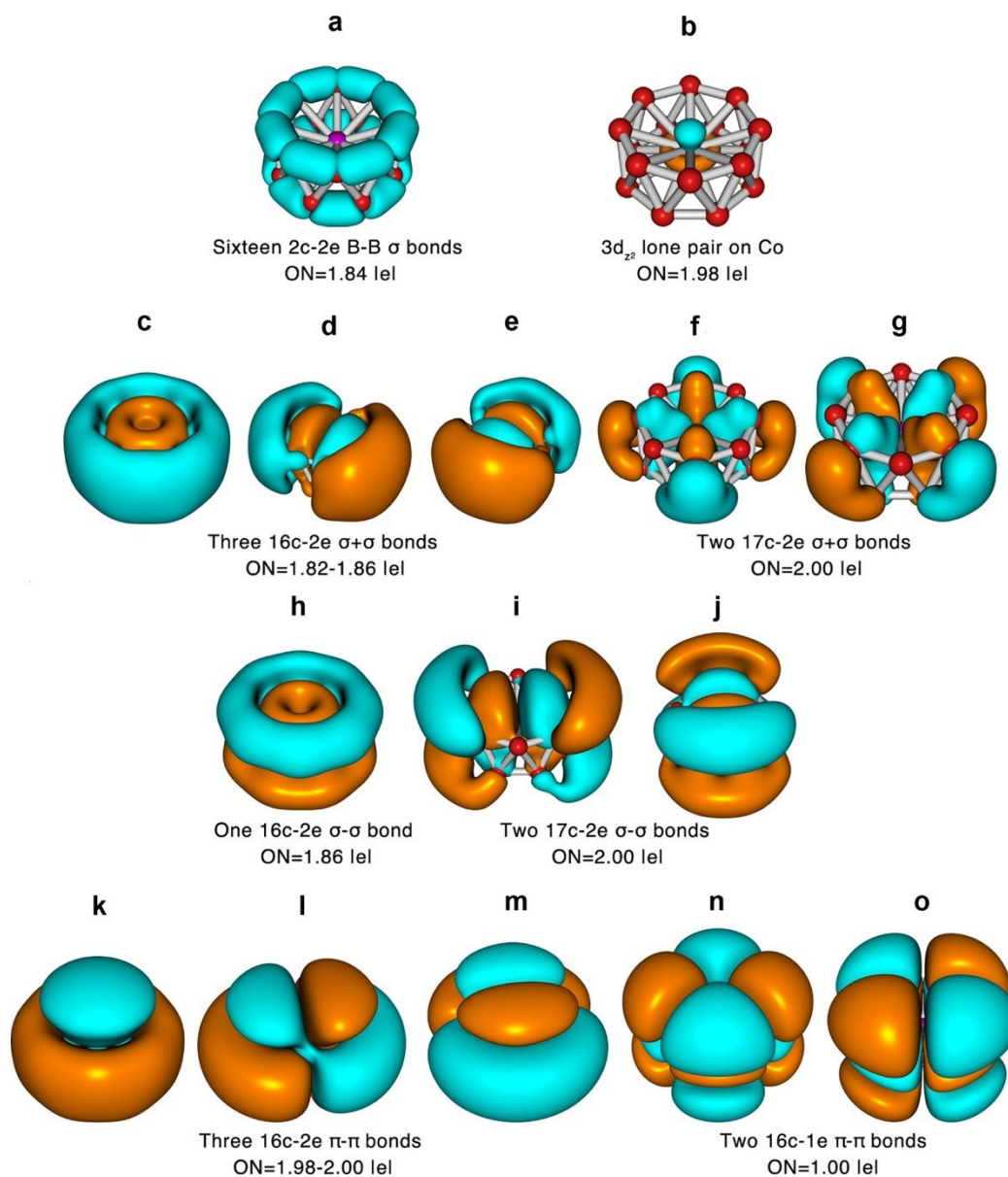
Fig. 50. AdNDP analyses for isomer I of the CoB$_{16}^{-}$. Reproduced from ref. 91 with permission from Macmillan Publishers Limited, copyright 2015.
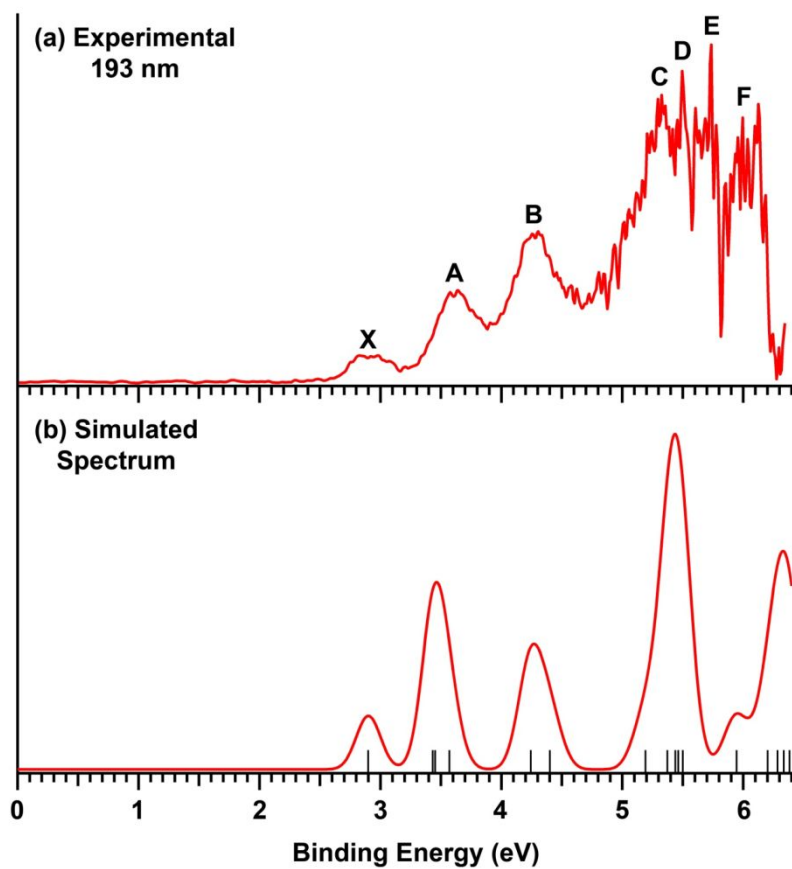
Fig. 51. Photoelectron spectrum of MnB_{16}^- at 193 nm (a), compared with the simulated spectrum (b) at the TD-SAOP/TZP level. Reproduced from ref. 92 with permission from AIP Publishing, copyright 2016.

MnB_{16}^{-} (C_{4v}, $^3B_2$)

MnB_{16} (C_{2v}, $^2A_1$)
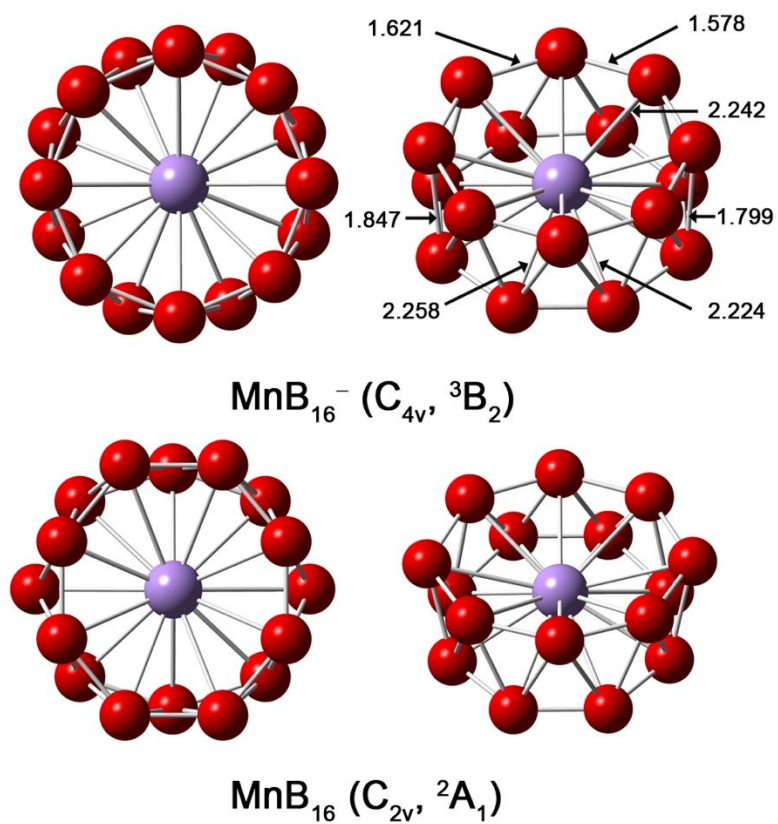
Fig. 52. Optimized structures of MnB_{16}^{-} and MnB_{16} at the PBE0/TZP level. All distances are in Å. Reproduced from ref. 92 with permission from AIP Publishing, copyright 2016.

Fig. 53. Valence molecular orbitals of MnB_{16}^{-} at the PBE0/TZP level. All the orbitals plotted were generated from the interactions between the $3d$ orbitals of Mn and the $2s/2p$ orbitals of B. The gray block corresponds to the energy levels mainly from the B $2s/2p$ orbitals (isovalue = 0.03 a.u.). Herein, r, t, and v represent radial, tangential, and vertical p-orbitals of each B atom in a local coordinate system (LCS), respectively, where the z-axis is across the two centers of the double ring and x-axis points to the center. Reproduced from ref. 92 with permission from AIP Publishing, copyright 2016.

Fig. 54. The chemical bonding picture of MnB_{16}^{-} obtained from UAdNDP analyses at the PBE0/TZVP level. ON stands for occupation number. Reproduced from ref. 92 with permission from AIP Publishing, copyright 2016.
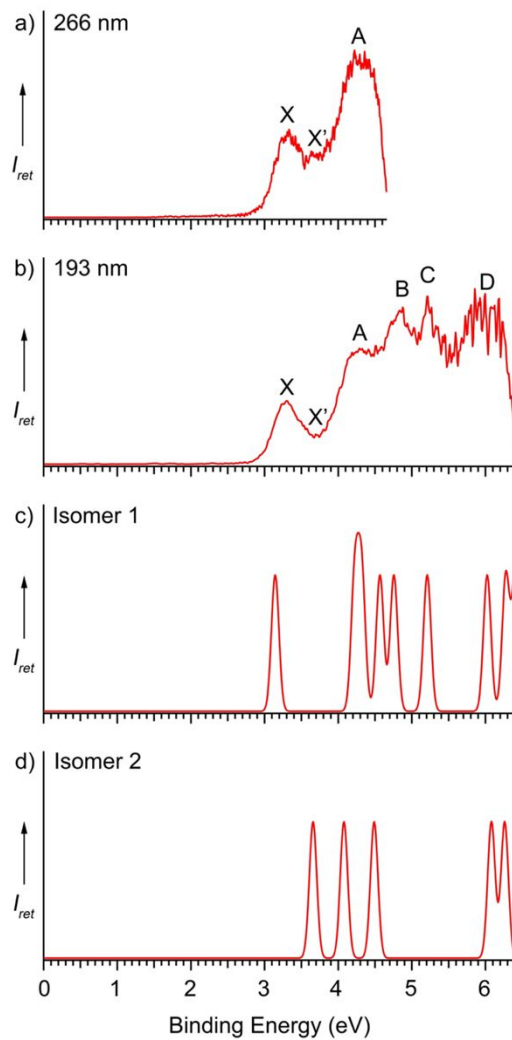
Fig. 55. Photoelectron spectra of TaB_{20}^- and comparison with simulated spectra. a) and b) experimental PE spectra at 266 nm and 193 nm. c) and d) the simulated spectra of isomers 1 and 2 at the SAOP/TZP level. Reproduced from ref. 94 with permission from the Royal Society of Chemistry, copyright 2017.
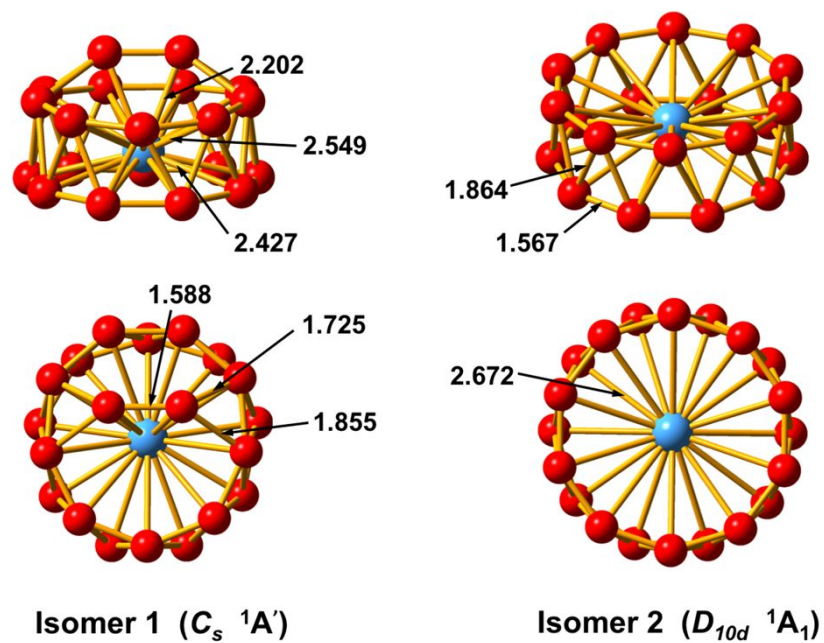
Fig. 56. Front and top views of isomers 1 and 2 of TaB$_{20}^-$ at the PBE0/TZP level. Reproduced from ref. 94 with permission from the Royal Society of Chemistry, copyright 2017.
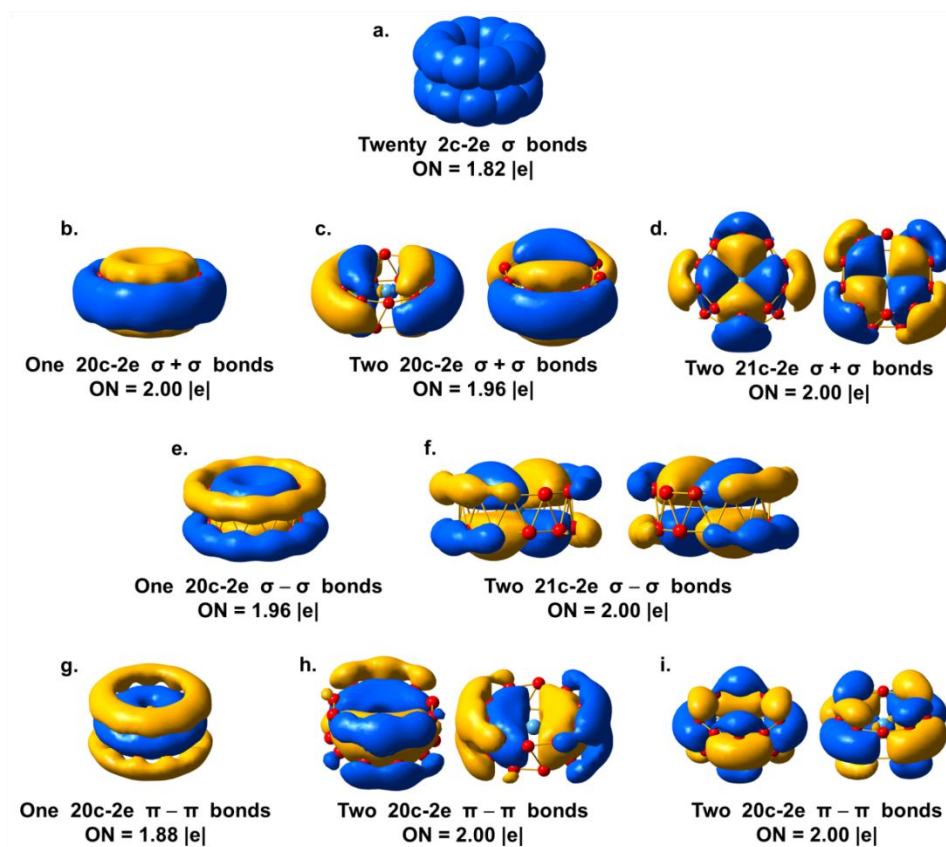
Fig. 57. AdNDP bonding pattern of D_{10d} Ta@B_{20}^-. Reproduced from ref. 94 with permission from the Royal Society of Chemistry, copyright 2017.

(a) $Ta_2B_2^-$ (C_{2v} $^2A_1$)   (b) $Ta_2B_3^-$ (C_{2v} $^3B_2$)   (c) $Ta_2B_4^-$ (C_{2v} $^2A_1$)   (d) $Ta_2B_5^-$ (C_{2v} $^1A_1$)
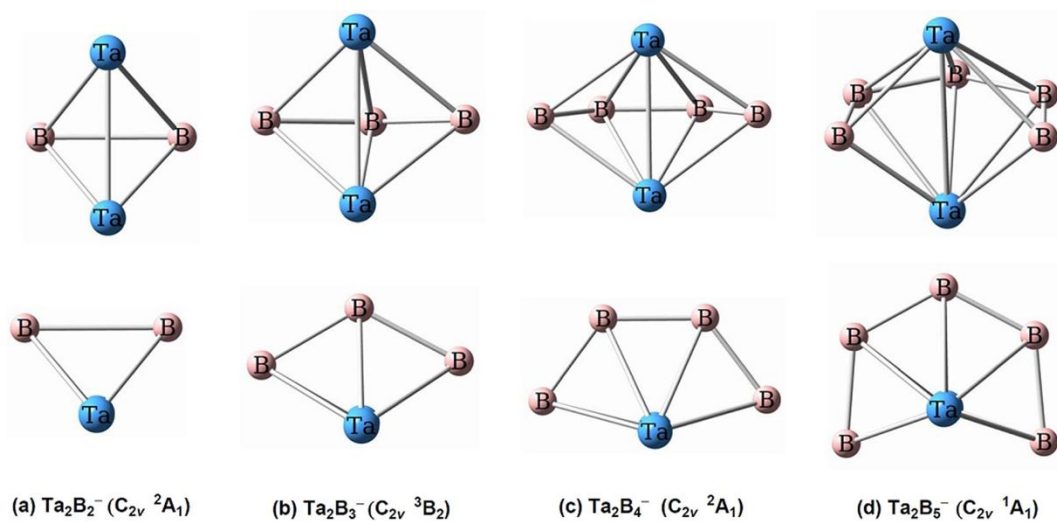
Fig. 58. Structure evolution of $Ta_2B_n^-$ (n = 2−5). Geometries in the second row are projections viewing along the Ta−Ta axis. Reproduced from ref. 101 with permission from the American Institute of Physics, copyright 2013.
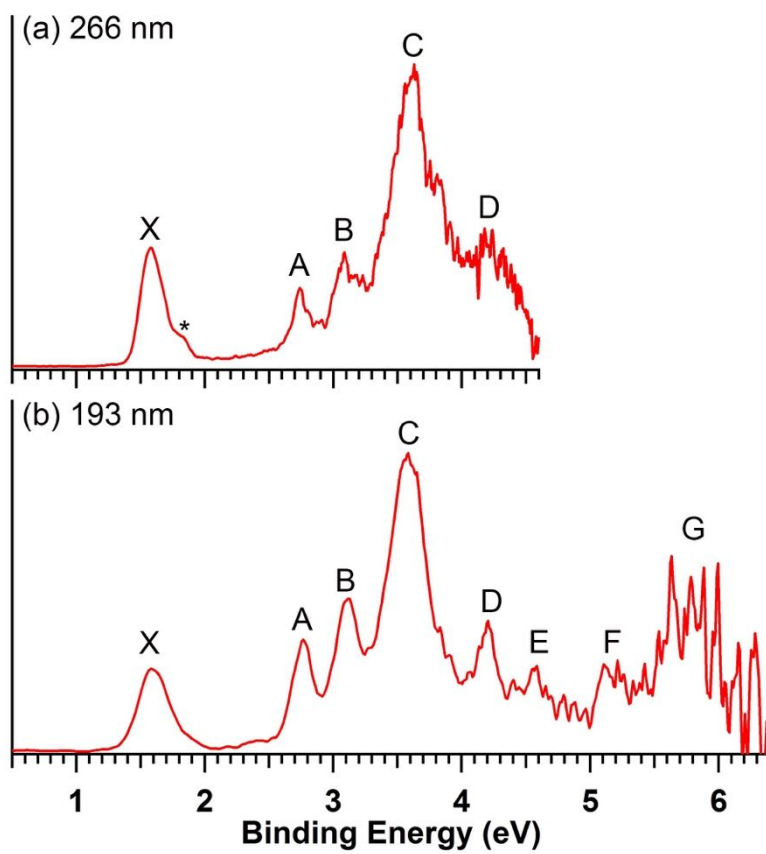
Fig. 59. Photoelectron spectra of $Ta_2B_6^-$ at 266 and 193 nm. Reproduced from ref. 102 with permission from Wiley-VCH, copyright 2014.
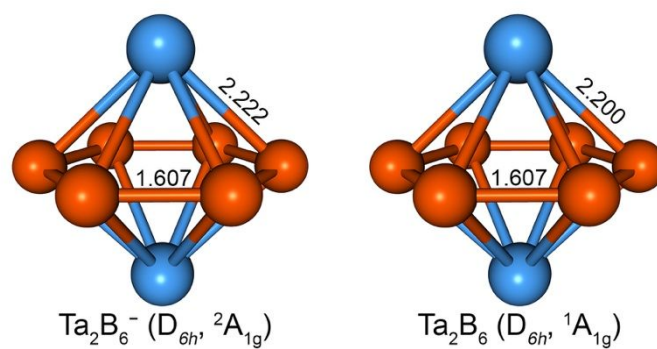
Fig. 60. Optimized structures of $Ta_2B_6^-$ and Ta_2B_6 at the BP86/Ta/ Stuttgart+2f1g/B/aug-cc-pVTZ level of theory. The bond lengths are in Å. Reproduced from ref. 102 with permission from Wiley-VCH, copyright 2014.
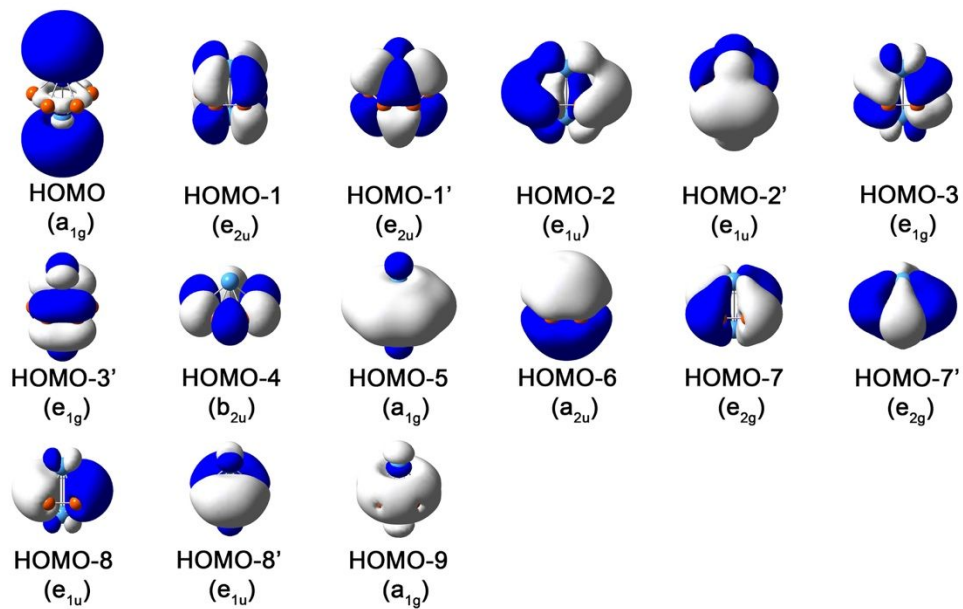
Fig. 61. Valence molecular orbitals of $Ta_2B_6^-$ at the BP86/Ta/Stuttgart+2f1g /B/aug-cc-pVTZ level of theory. Reproduced from ref. 102 with permission from Wiley-VCH, copyright 2014.
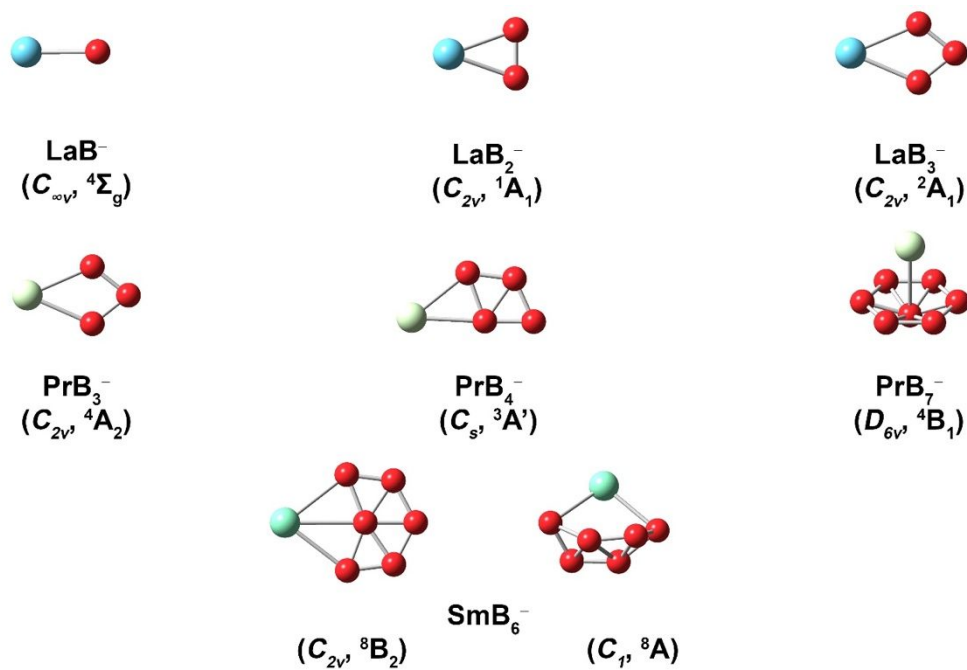
Fig. 62. A summary of the global minima of mono-lanthanide doped boron clusters confirmed from experiments.
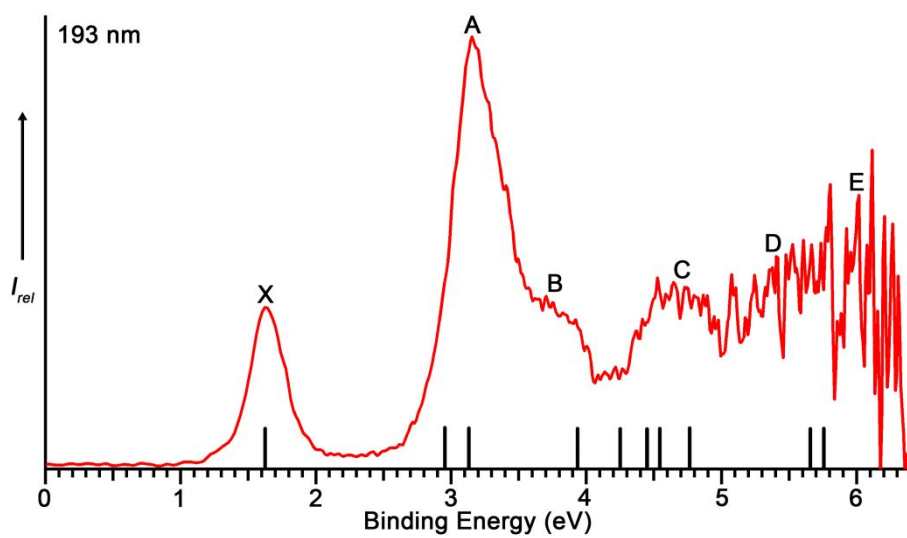
Fig. 63. Photoelectron spectrum of PrB$_7^-$ at 193 nm. The vertical bars represent the calculated vertical detachment energies. Reproduced from ref. 99 with permission from Wiley-VCH, copyright 2017.
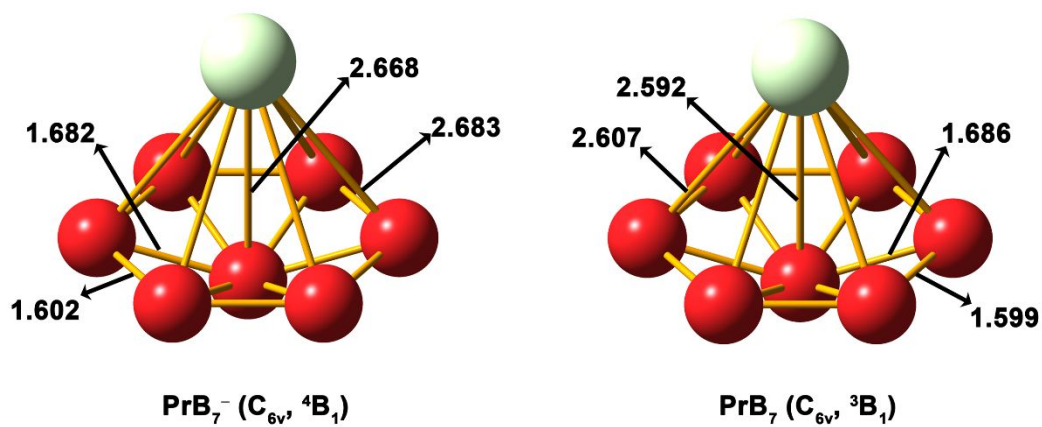
Fig. 64. The optimized global minimum structures of PrB_7^- and neutral PrB_7. The bond lengths are given in Å. Reproduced from ref. 99 with permission from Wiley-VCH, copyright 2017.
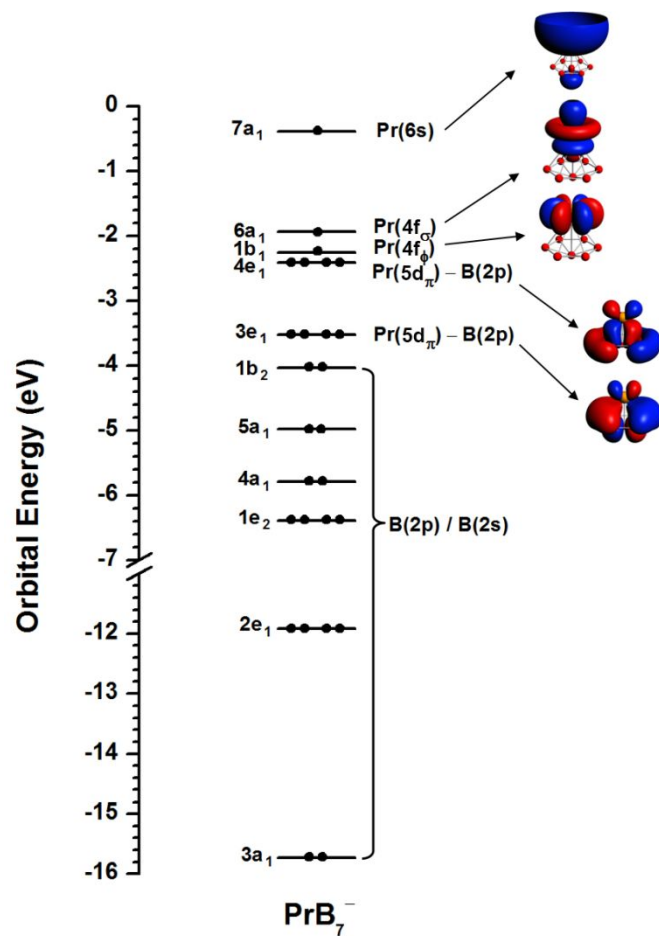
Fig. 65. The molecular orbital energy levels of PrB_7^- at the PBE0/TZP level. Reproduced from ref. 99 with permission from Wiley-VCH, copyright 2017.

Six 2c–2e σ bonds
ON = 1.90 |e|

Three 7c–2e σ bonds
ON = 1.99 |e|

Three 8c–2e π bonds
ON = 1.98-2.00 |e|
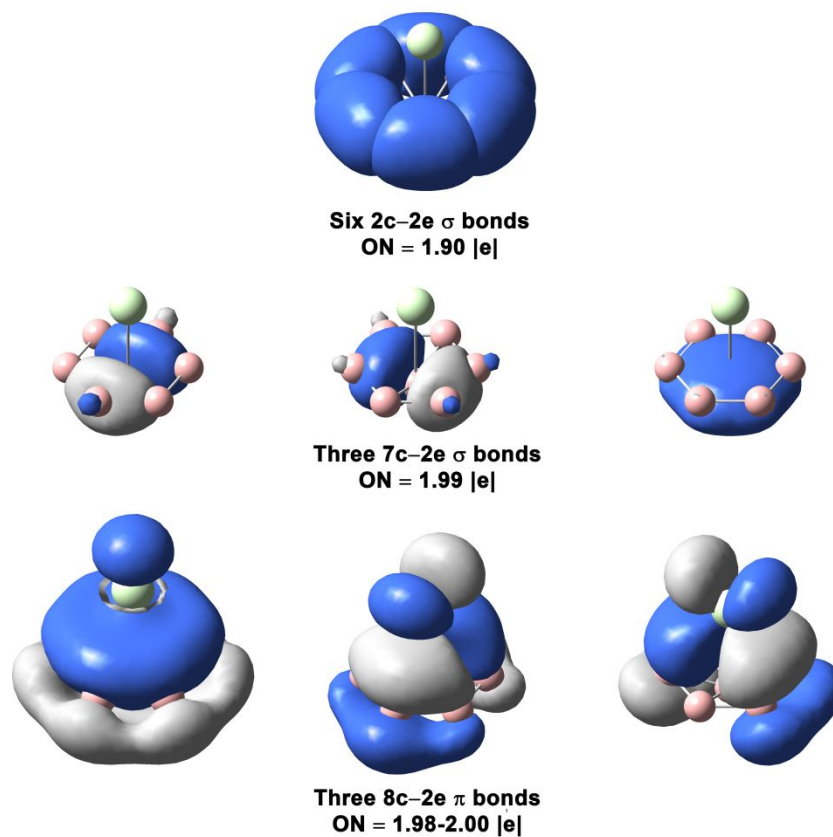
Fig. 66. AdNDP analyses for the B_7^{3-} moiety in PrB_7 $\{Pr(III)[\eta^7\text{-}B_7^{3-}]\}$ at the PBE0/TZP level. The two unpaired and localized 4f electrons on Pr(III) are not shown. Reproduced from ref. 99 with permission from Wiley-VCH, copyright 2017.
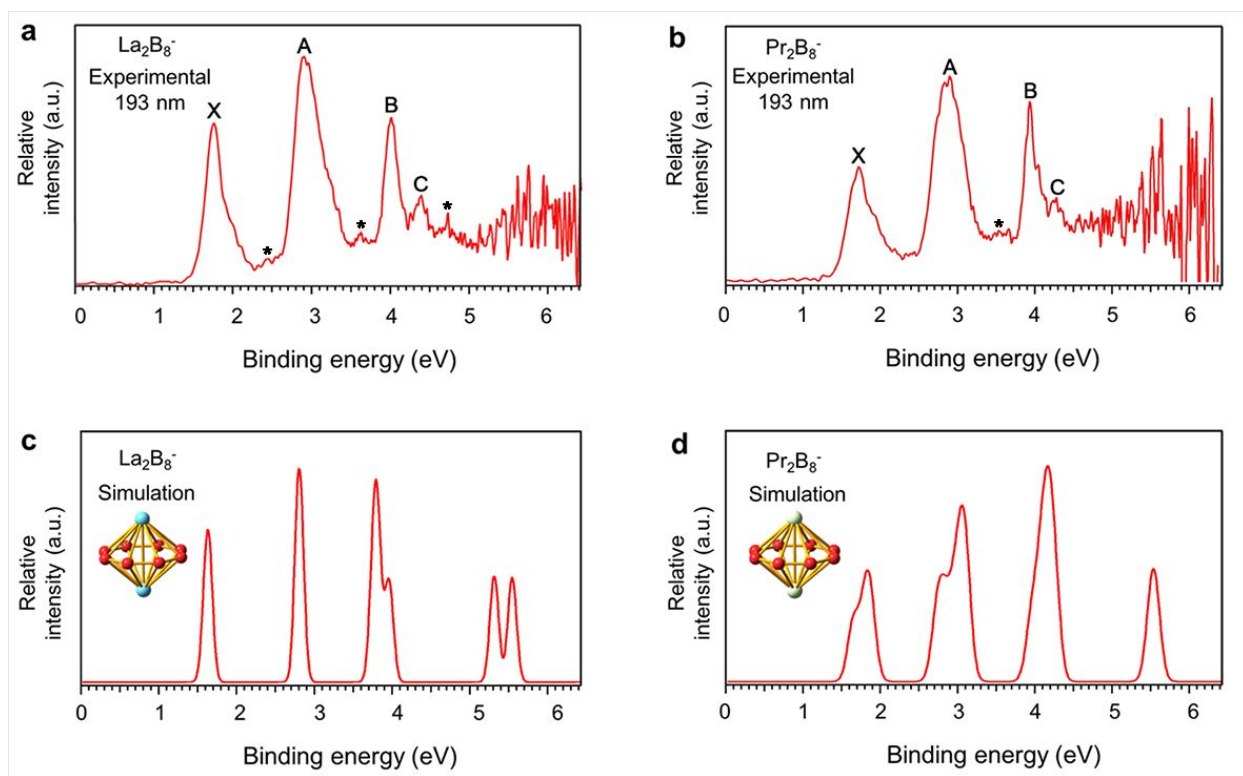
Fig. 67. Photoelectron spectra of (a) $La_2B_8^-$ and (b) $Pr_2B_8^-$ at 193 nm and comparison with the simulated spectra for the (c) D_{4h} $La_2B_8^-$ and (d) D_{4h} $Pr_2B_8^-$. Reproduced from ref. 103 with permission from PNAS (USA), copyright 2018.
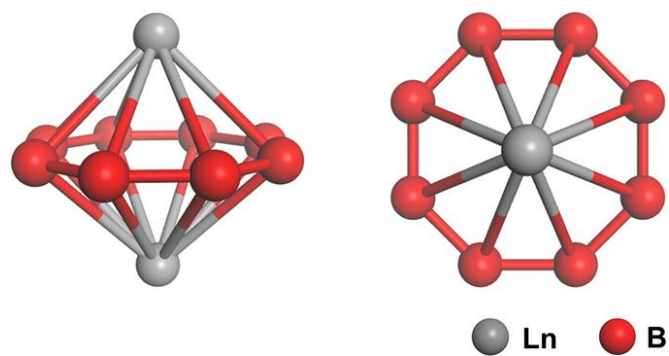
Fig. 68. Two views of the global minima of the neutral D_{8h} Ln_2B_8. Bond lengths: Ln. . .Ln = 3.720 Å (La), 3.558 Å (Pr); Ln−B = 2.759 Å (La), 2.701 Å (Pr); B−B = 1.560 Å (La), 1.555 Å (Pr) at the PBE0/TZP level. Reproduced from ref. 103 with permission from PNAS (USA), copyright 2018.
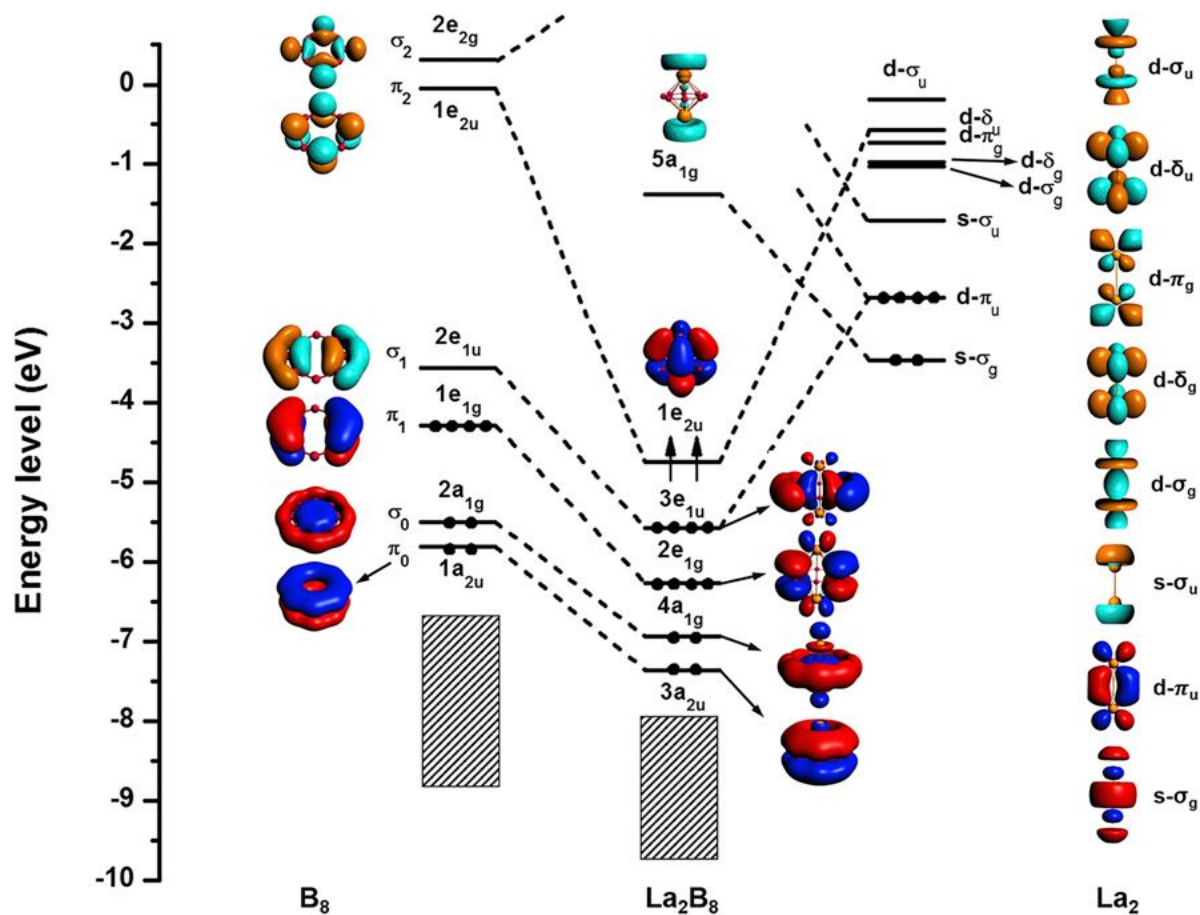
Fig. 69. The MO bonding scheme of D_{8h} La_2B_8 at the level of PBE0/TZP, illustrating the bonding interactions between the La. . .La and B_8 fragments. Reproduced from ref. 103 with permission from PNAS (USA), copyright 2018.
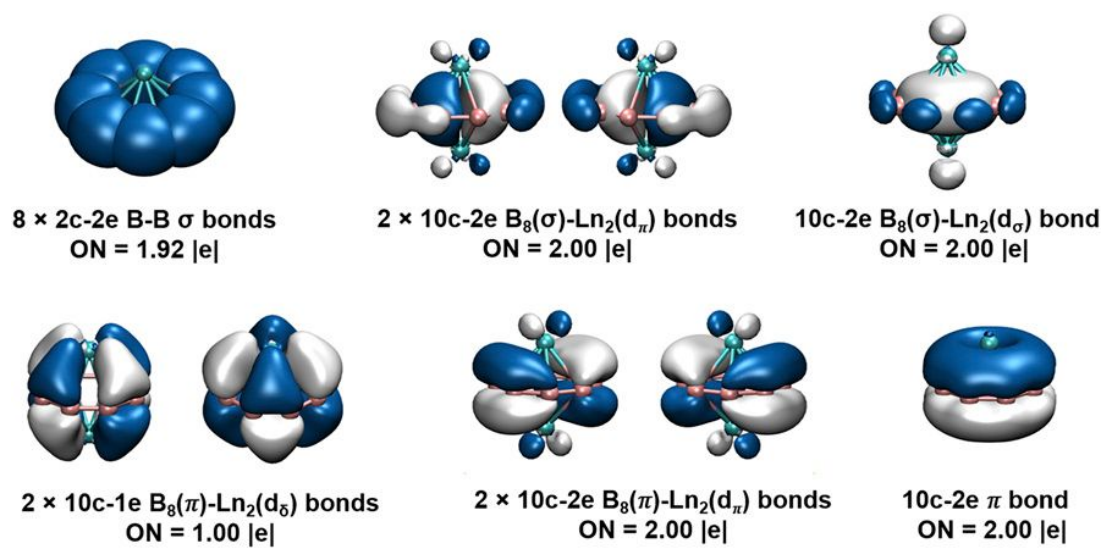
Fig. 70. AdNDP bonding analyses for La_2B_8 at the PBE0/cc-pVTZ level. Occupation numbers (ON) are shown. Reproduced from ref. 103 with permission from PNAS (USA), copyright 2018.
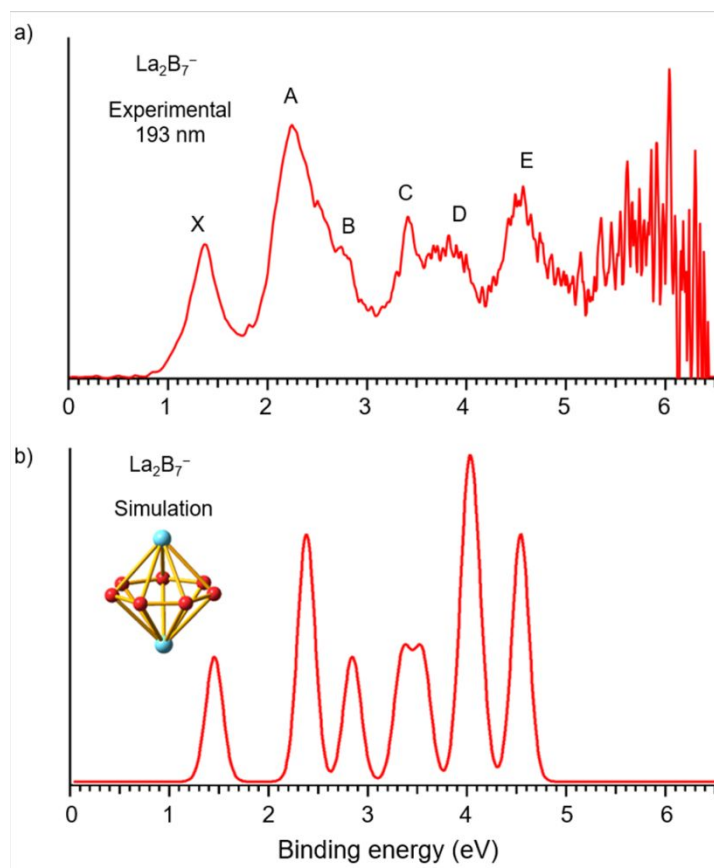
Fig. 71. Photoelectron spectrum of $La_2B_7^-$ at 193 nm (a) and the simulated spectrum (b) for the D_{7h} global minimum of $La_2B_7^-$. Reproduced from ref. 104 with permission from the Royal Society of Chemistry, copyright 2019.
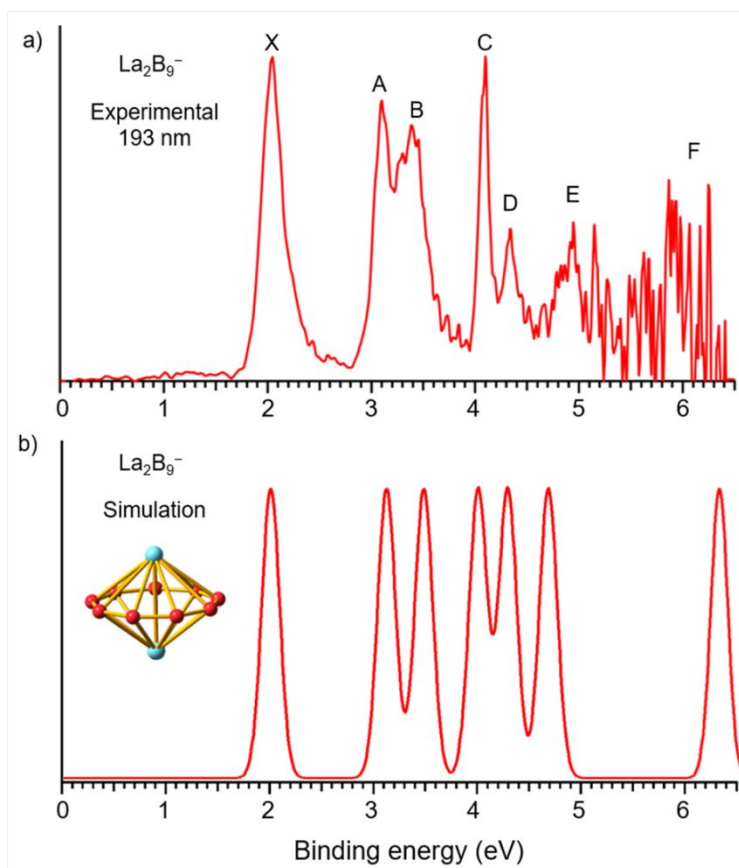
Fig. 72. Photoelectron spectrum of La$_2$B$_9^-$ at 193 nm (a) and the simulated spectrum (b) for the D$_{9h}$ global minimum of La$_2$B$_9^-$. Reproduced from ref. 104 with permission from the Royal Society of Chemistry, copyright 2019.
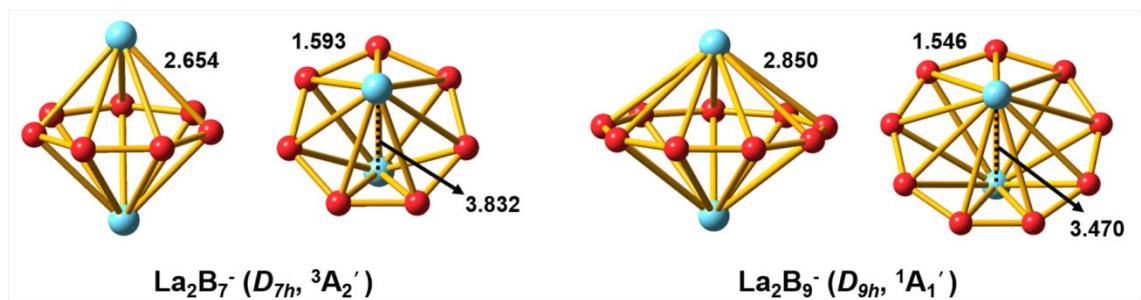
Fig. 73. The optimized global-minimum inverse-sandwich structures of $La_2B_7^-$ and $La_2B_9^-$ at the PBE0/TZP level. Reproduced from ref. 104 with permission from the Royal Society of Chemistry, copyright 2019.
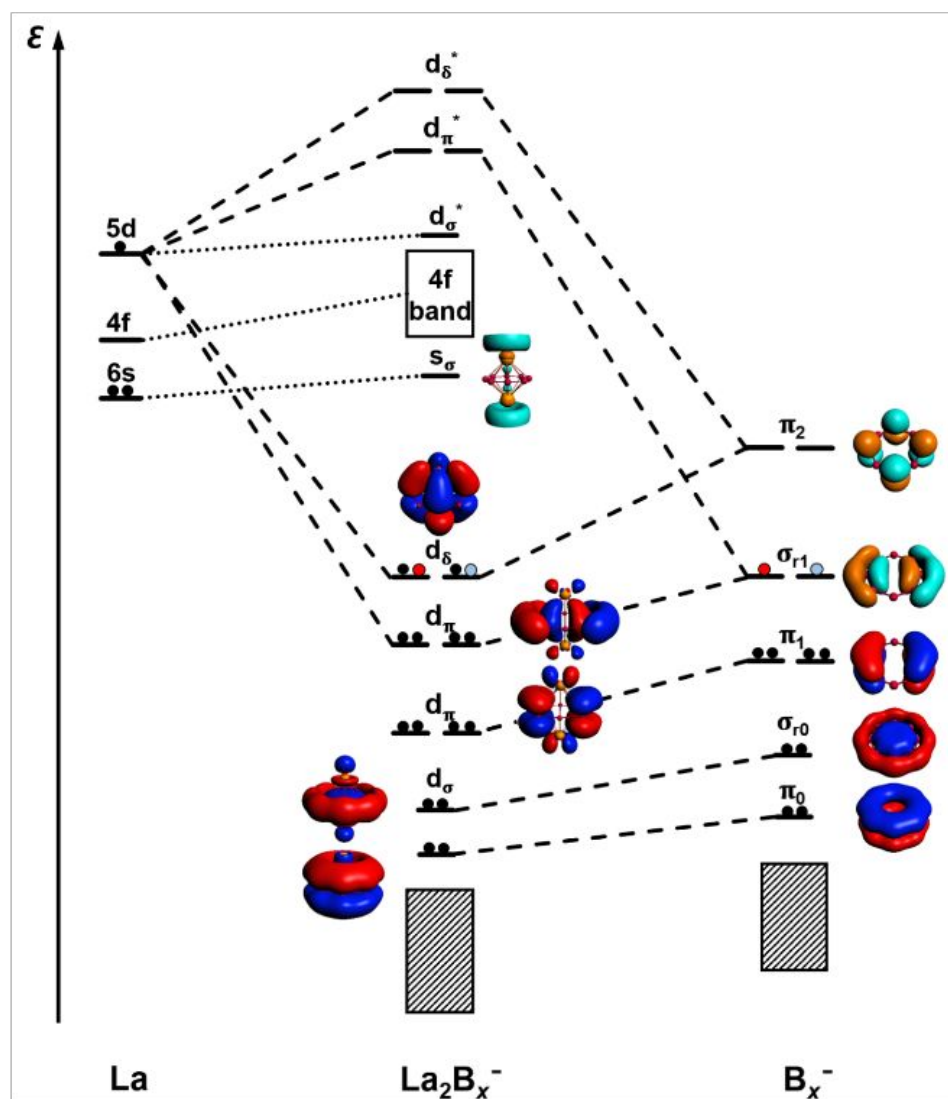
Fig. 74. A schematic MO diagram for the $La_2B_x^-$ ($x = 7-9$) inverse sandwiches, showing the major bonding interactions between the La 5d orbitals and the local orbitals of the B_x^- ring. Red and blue dots indicate the successive additional electrons for $La_2B_8^-$ and $La_2B_9^-$, respectively. Reproduced from ref. 104 with permission from the Royal Society of Chemistry, copyright 2019.

La$_2$B$_7^-$

7 × 2c-2e B-B σ bonds
ON = 1.88 |e|

2 × 9c-2e B$_7$(σ)-La$_2$(d$_\pi$) bonds
ON = 2.00 |e|

9c-2e B$_7$(σ)-La$_2$(d$_\sigma$) bonds
ON = 2.00 |e|

2 × 9c-1e B$_7$(π)-La$_2$(d$_\delta$) bonds
ON = 1.00 |e|

2 × 9c-2e B$_7$(π)-La$_2$(d$_\pi$) bonds
ON = 2.00 |e|

9c-2e π bonds
ON = 2.00 |e|

La$_2$B$_9^-$

9 × 2c-2e B-B σ bonds
ON = 1.93 |e|

2 × 11c-2e B$_9$(σ)-La$_2$(d$_\pi$) bonds
ON = 2.00 |e|

11c-2e B$_9$(σ)-La$_2$(d$_\sigma$) bonds
ON = 2.00 |e|

2 × 11c-2e B$_9$(π)-La$_2$(d$_\delta$) bonds
ON = 2.00 |e|

2 × 11c-2e B$_9$(π)-La$_2$(d$_\pi$) bonds
ON = 2.00 |e|

11c-2e π bonds
ON = 2.00 |e|
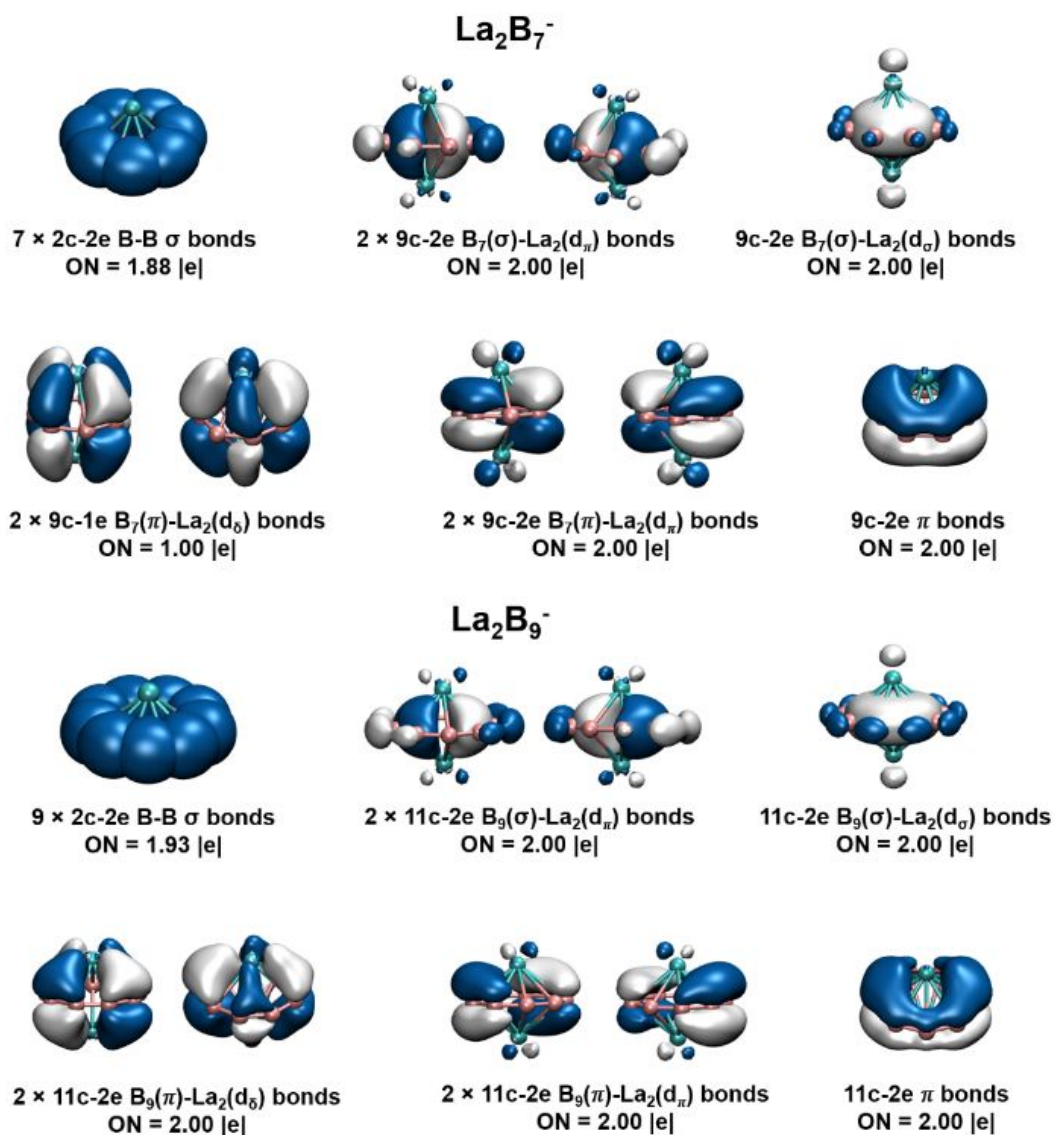
Fig. 75. AdNDP analyses for the La$_2$B$_n^-$ (n = 7, 9) inverse sandwiches at the PBE0/VTZ level. Occupation numbers (ON) are also given. Reproduced from ref. 104 with permission from the Royal Society of Chemistry, copyright 2019.
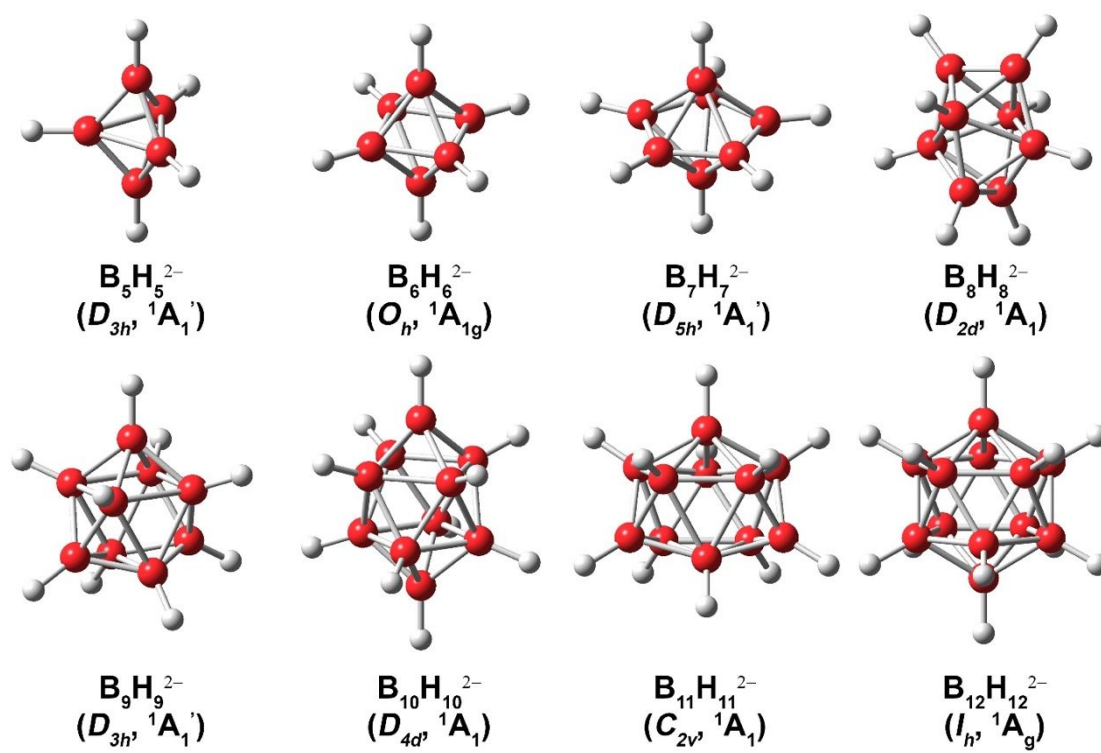
Fig. 76. A summary of the borane clusters $B_nH_n^{2-}$ (n = 5-12).
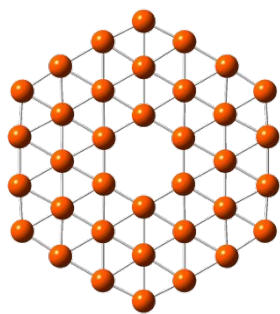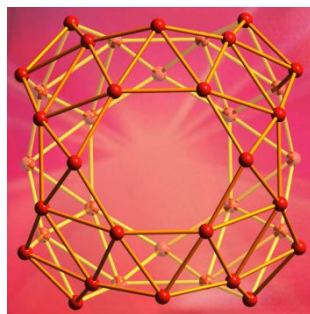
B$_{36}$: borophene   B$_{40}$: borospherene

Photoelectron spectroscopy in conjunction with theoretical calculations has been used to investigate size-selected boron clusters, uncovering interesting structures and bonding